博 士 学 位 論 文
Doctoral Thesis

論文題目

Thesis Title

Research on Time-Modulated Reflectarray

時間変調リフレクトアレーの研究

東 北 大 学 大 学 院 工 学 研 究 科

Graduate School of Engineering,

TOHOKU UNIVERSITY

専攻/Department: Communications Engineering

学籍番号/ ID No: B9TD9202

氏 名 /Name: 曹　　先　　博 (Cao Xianbo)

Research on Time-Modulated Reflectarray

(時間変調リフレクトアレーの研究)

by

Cao Xianbo（曹 先博）

A Dissertation
for Doctor of Philosophy (Engineering)

Submitted to
Department of Communications Engineering
Graduate School of Engineering
Tohoku University

July, 2023

Supervised by Prof. Chen, Qiang （陳　強）

Abstract

Reconfigurable Reflectarray (RRA) has attracted significant interest in wireless communication applications, particularly in the context of Reconfigurable Intelligent Surfaces (RIS), due to its appealing features such as flexible beam control capability and low cost. Existing RRAs designed based on frequency-domain methods, such as phase-controllable RRAs and amplitude-controllable RRAs, can control either the reflection phase or the reflection amplitude. However, a common limitation of these methods is their inability to achieve real-time simultaneous control of both reflection amplitude and phase, which restricts their beam control capability. To overcome this limitation, a more flexible approach is to design the equivalent reflection coefficients (amplitude and phase) of RRA using the time-varying characteristics of control signals. This architecture is referred to as Time-Modulated Reflectarray (TMRA). Moreover, unlike previously reported TMRA designs, this dissertation focuses on TMRA operating at the carrier frequency to enhance its scattering efficiency and practicality.

In this paper, addressing the lack of effective evaluation methods for TMRA efficiency, an analysis method and a quantification definition expression for TMRA efficiency are proposed for the first time, adding a new dimension to the comprehensive evaluation of TMRA performance. Inspired by the 1-bit RRA, a 1-bit TMRA, capable of realizing controllable reflection amplitude and phase by utilizing two phase-antipodal reflection states of 1-bit RRA, is designed. The prototype of a 10×10 1-bit TMRA, a 1-bit functional control board, and a time modulation functional control board are fabricated. In the validation experiment of the 1-bit functionality (controlling reflection phase), a high-gain and wideband printed Fermi antenna is used as the feeding source, operating at a frequency of 11.1 GHz. Theoretical and experimental results demonstrate good consistency, achieving a realized gain of 15.6 dBi at 11.1 GHz, corresponding to 21.1 % aperture efficiency. Fur-

thermore, the scattering beam can be steered within the range of 10° to 50°, indicating the real-time reflection phase control capability of the proposed 1-bit TMRA. On the other hand, in the validation experiment of time modulation functionality (controlling reflection amplitude), a 20 dB Chebyshev pattern is successfully achieved by shaping the scattering beam using the proposed 1-bit TMRA prototype, with a TMRA efficiency of 64.6 %. This demonstrates the real-time reflection amplitude control capability of the proposed 1-bit TMRA. The scattering characteristics of TMRA, such as gain bandwidth, SLL bandwidth, and time modulation signal bandwidth, are also analyzed in detail to provide design guidelines for TMRA applications. Additionally, by measuring the scattering patterns at different time modulation frequencies, it is shown that the scattering characteristics of TMRA remain unchanged with TM frequency, which is important for a deeper analysis of TMRA scattering characteristics and its applicable range.

To address the aforementioned limitation of TMRA's inability to simultaneously control amplitude and phase, a method is proposed to enable TMRA with independent control over both parameters, facilitating enhanced efficiency beam shaping at the carrier frequency. A phase-reversal switching method is introduced to control the switching mode between different phase states of a Q-bit RRA, enabling control of the reflection amplitude. Furthermore, a theoretical analysis of TMRA implemented using Q-bit RRA is conducted, and the results demonstrate that selecting an appropriate number of phase quantization bits Q can achieve good beam shaping performance. Additionally, the proposed method outperforms traditional TMRA operating at the harmonic frequency in terms of directional coefficient and efficiency, showcasing its efficiency-enhancing characteristics.

A series of experimental validations are performed using TMRA based on a 1-bit RRA. Theoretical calculations and measurement results exhibit good consistency, confirming that the proposed method can achieve beam shaping as expected, validating its ability to simultaneously control the reflection amplitude and phase. Moreover, loss and efficiency analysis is conducted to objectively assess the radiation performance of the 1-bit TMRA used in the experimental validation. In conclusion, the proposed TMRA operating at the carrier frequency in this paper will make significant contributions to enhancing the performance and expanding the functionalities of TMRA in RIS applications.

List of Figures

List of Tables

Chapter 1

Introduction

1.1 Background

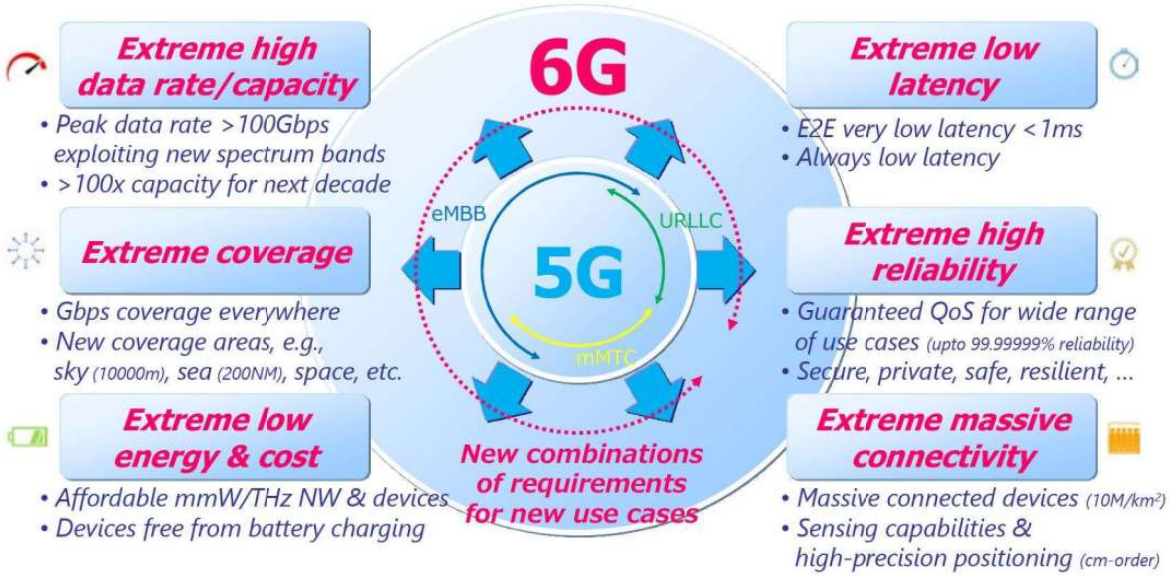

Figure 1.1: Requirements for 6G wireless technology [1]

The gradual emergence of societal and production improvements brought forth by the implementation of 5G is expected. However, the evolving user needs, enhanced ser-

vice experiences, and the expansion of vertical industry services will drive the continuous advancement of mobile communication networks [1]. In the era beyond 5G and 6G, emerging business requirements such as digital twins, holographic interaction, and sensory interconnection will impose greater demands on mobile network coverage depth, ubiquitous access capability, air interface transmission rate, end-to-end delay, device connection capacity, and endogenous intelligence level. Consequently, higher operating frequency bands, larger antenna sizes, lower equipment energy consumption, and heightened levels of intelligence have become pivotal trends in the development of future mobile communication networks.

Despite the opportunities that lie ahead, the development of mobile communication networks faces various challenges [2]:

1) Inadequate high-frequency channel environment: High-frequency signals exhibit higher propagation loss and penetration loss compared to low-frequency signals. Consequently, network coverage areas may experience blind spots or weak coverage areas due to the susceptibility of high-frequency signals to obstacles. This limitation hampers the realization of wireless network ubiquity and deep coverage.

2) Constraints on massive multi-input multi-output (MIMO) development: The expansion of antenna size in massive MIMO systems increases the complexity and cost of antenna manufacturing, channel measurement and modeling, signal processing calculations, and reference information utilization. Consequently, there is a growing demand for effective integration of antenna systems that are characterized by low cost, low power consumption, high reliability, and easy deployment.

3) Escalating energy consumption burden: The energy consumption of current 5G base stations surpasses that of 4G base stations by several times. Furthermore, as society undergoes accelerated digital transformation, the computing power requirements of mobile communication networks will increase further. Addressing equipment energy consumption effectively becomes a critical factor influencing the selection of technology for next-generation wireless networks.

4) Passive adaptation to the wireless environment: Since its inception, mobile communication systems have primarily relied on passive adaptation to the wireless environment's path loss and multipath fading. The air interface often poses a significant barrier to network performance. Network requirements such as endogenous intelligence and dynamic

reconfiguration have gradually shifted from the core network side to the wireless access side. Therefore, establishing a new paradigm for next-generation mobile communication networks will revolve around on-demand intelligent dynamic reconfiguration of the wireless domain.

In recent years, Reconfigurable Intelligent Surface (RIS) has attracted extensive attention from academia and industry due to its ability to flexibly manipulate the electromagnetic properties of the channel environment [3–8]. The introduction of RIS has changed the wireless propagation environment from passive adaptation to active control, thus building an intelligent wireless environment. In addition, as a two-dimensional implementation of metamaterials, RIS is naturally low-cost, low-complexity, and easy-to-deploy, and could be used to address the needs and challenges facing the development of future mobile communication networks.

1.2 Previous Study of RIS Implementation

The core of the physical implementation of RIS is the design of RIS elements with controllable electromagnetic wave reflection characteristics. Specifically, RIS elements need to achieve flexible control over the reflection coefficients (amplitude and phase) of the reflected waves. Since RIS is a novel concept that has emerged in recent years, there is currently no consensus on the physical implementation of RIS from the perspective of scattering control techniques [12]. So far, research on the physical implementation of RIS has primarily been based on existing controllable scattering structures, with the most extensively studied structure being the reconfigurable reflectarray (RRA).

The RRA evolves from the reflectarray by introducing electronically controlled electronic components, control structures, or ingeniously designed variable physical structures within the reflectarray element. This enables real-time control of the reflection characteristics of the reflectarray, providing flexible beam-forming capabilities, which makes it suitable as a physical implementation method for RIS. Depending on the different implementation methods of reconfigurability, RRA can be mainly classified into electronically controlled RRA and mechanically controlled RRA.

Electronically controlled RRA refers to the use of control structures (such as electronic components and control materials) within the RRA element to modify the electrical

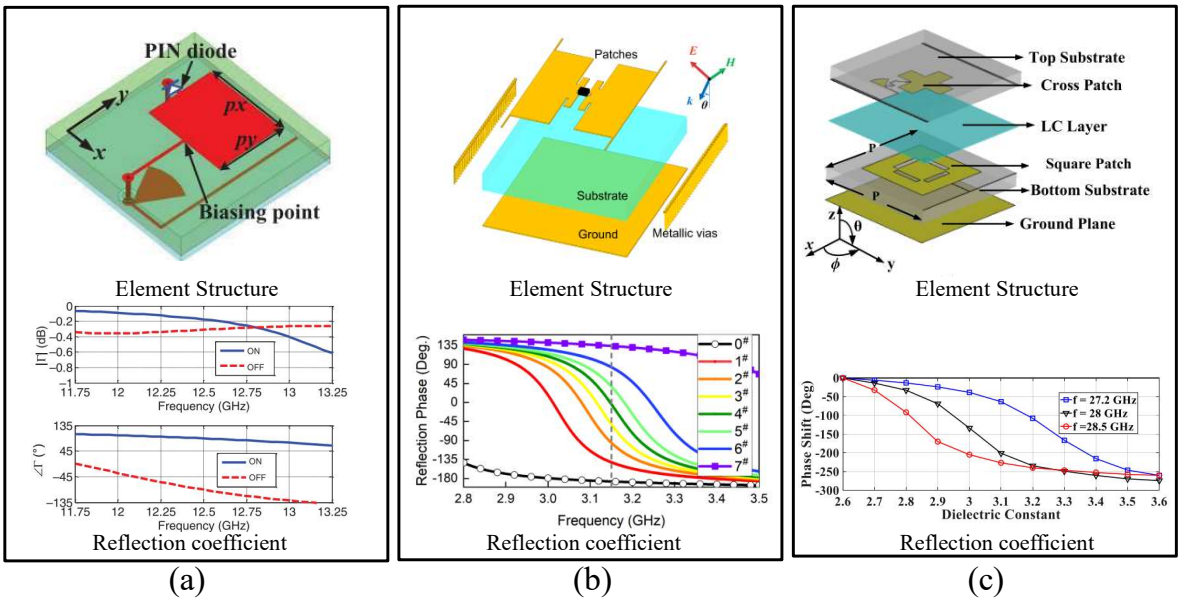

Figure 1.2: Typical electronically controlled RRA. (a) PIN diode-based 1-bit RRA in [9]. (b) Varactor diode-based 3-bit RRA in [10]. (c) Liquid crystal-based RRA in [11]

characteristics of the control structures. As shown in Fig. 1.2(a), [9] proposed an RRA element based on PIN diodes, where different reflection characteristics of the RRA are achieved by controlling the bias voltage of the diodes. Specifically, the diode is connected between the patch on the top layer and the grounding via. When a forward voltage is applied to the diodes, the diodes conduct, short-circuiting the patch to the ground. Conversely, when a reverse voltage is applied to the diode, the diode is cut-off, open-circuiting the patch to the ground. Due to the 180 ° phase difference between the short-circuit and open-circuit reflection coefficients, this RRA structure is also referred to as a 1-bit RRA [13–18]. The number of bits (n) refers to the number of phases that the reconfigurable reflection coefficients possess (2^n).

By implementing two different reflection phase states (1-bit), beam steering can be achieved by 1-bit phase quantization of the required phase distribution for forming beams in different directions. In general, 1-bit RRA is prone to large side-lobe level (SLL) and beam squint when realizing larger angular beam steering, which is due to the huge 1-bit

phase quantization error. In order to reduce phase quantization errors and achieve better beam steering performance, recent research has also proposed a 2-bit RRA based on PIN diodes [19–22]. However, the complex design of reconfigurable scattering structures and bias circuitry pose significant challenges for designing higher-bit RRAs based on PIN diodes.

Therefore, RRAs based on other electronic components have also received extensive research attention, such as varactor [23–27]. A 3-bit RRA based on varactor diode was proposed in [10]. Varactor diodes exhibit the characteristic of varying capacitance with bias voltage. As shown in Fig. 1.2(b), the varactor diode is placed between two patches on the top layer of the RRA element, and different capacitance values are generated by applying different bias voltages. This, in turn, changes the input impedance of the RRA element, ultimately achieving controllable reflection phase. It is worth pointing out that although continuous control of the reflected phase is theoretically possible (the capacitance value varies continuously with the bias voltage), it is limited by the number and accuracy of the achievable bias voltage values, and only 3-bit phase control has been achieved in the published studies so far. In addition to varactor diodes, another method to achieve continuous phase control is by using liquid crystal as the dielectric substrate of the RRA element [28–32]. As shown in Fig. 1.2(c), In [11] proposed an RRA structure based on a liquid crystal substrate, where the liquid crystal is placed between the top-layer patch and the intermediate-layer patch. Due to the change in molecular polarity of the liquid crystal with the variation of the nearby electric field, it macroscopically exhibits a change in the dielectric constant, as shown in the figure. Therefore, by applying different bias voltages, the dielectric constant of the RRA medium can be altered, thus controlling the RRA element to achieve different reflection phases. As can be easily found, the advantage of electronically controlled RRA is the simplicity of the control structure as well as the ease of real time control. However, the aperture efficiency is usually low due to the use of active devices, which results in the loss of RF power.

Another major classification of RRAs is mechanically controlled RRAs, which refers to the use of mechanical methods (e.g., movement, rotation) to change the physical structure of the RRA cell to achieve control of the reflected phase [36–40]. As shown in Fig. 1.3(a), in [33], a RRA based on a movable structure is proposed to achieve 2-bit reflection phase

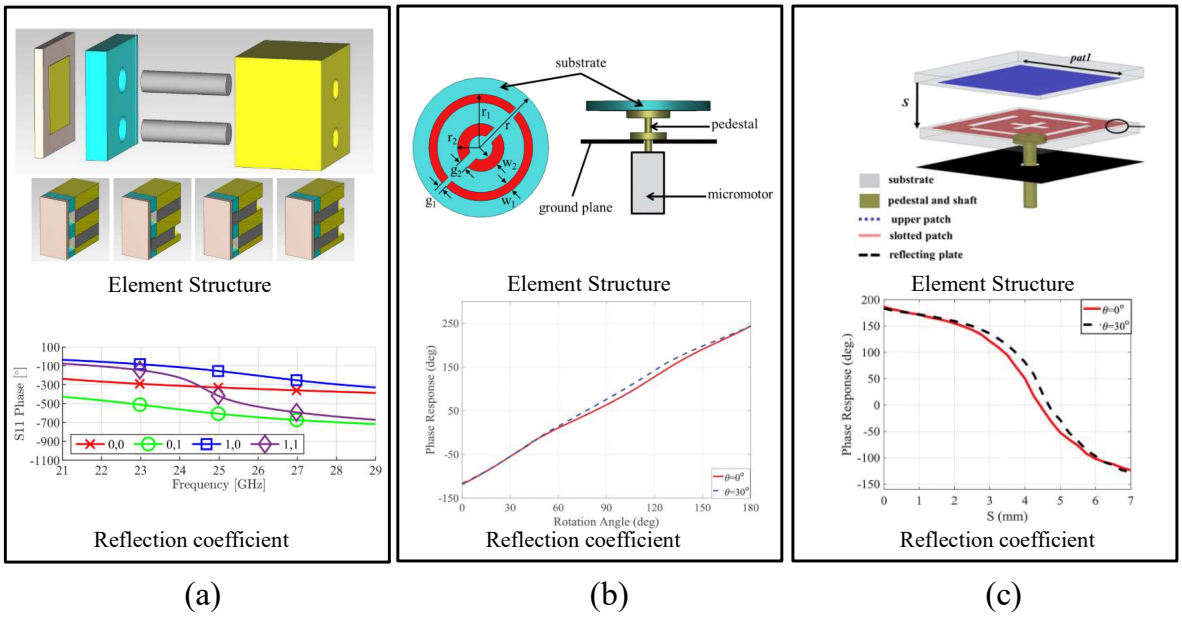

Figure 1.3: Typical mechanically controlled RRA. (a) Movable structure-based RRA in [33]. (b) Rotatable structure-based RRA in [34]. (c) Height-adjustable structure-based RRA in [35]

control by changing the relative position relationship of two metal columns. As shown in 1.3(c), in [35] , an RRA based on height-adjustable structure was proposed to achieve the control of reflection phase by changing the thickness of the air layer sandwiched between the top patch and the middle patch. In addition to this, an RRA based on a rotating structure has also been proposed, as shown in Fig. 1.3(b). In [34], a concentric dual split rings-shape patch element was proposed. By rotating the element structure, the reflection phase control in 360° is achieved. It is evident that, benefiting from the principle of controlling phase by altering the physical structure, mechanically controlled RRA exhibits low losses, structural stability, and excellent efficiency and robustness. However, compared to electronically controlled RRA, the real-time control module based on mechanical methods is characterized by complex principles and bulky structures, which represents a significant challenge for mechanically controlled RRA. On the other hand, the switching speed of mechanically controlled RRA (to achieve different control

states) is relatively slow, thereby limiting its application in RIS scenarios.

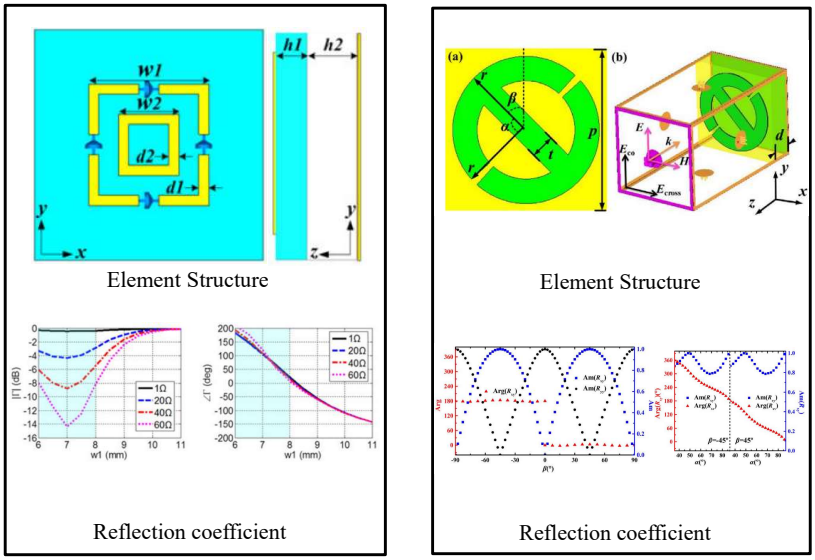

Figure 1.4: Typical amplitude controllable RRA. (a) Resistor-based RRA in [41]. (b) Rotatable structure-based RRA in [42].

A limitation of the existing RRAs, which can only control the phase of the reflection coefficient, can be easily found from the above introduction. Therefore, RRA can only realize the control of the direction of the reflected beam, i.e. beam-steering. In order to fully utilize the powerful control capability of RIS on the reflected beam, it is essential to realize the beam-forming function. This requires the RIS elements to add the extra control of reflection amplitude to the control of reflection phase. As shown in Fig. 1.4(a), a resistor-based RRA was proposed in [41]. Resistors are placed in the patch structure where the induced current is maximum, and a portion of the power is consumed through the resistors to achieve control of the reflection amplitude. As shown in Fig. 1.4(b), a rotating structure-based RRA is proposed in [42], which can produce a reflected wave polarization component (cross-polarization) orthogonal to the incident wave polarization (co-polarization), and the magnitude of the cross-polarization component varies with the rotation angle. Therefore, the reflection amplitude control of the cross-polarization component can be achieved by rotating the RRA structure. There

are relatively few studies on amplitude controllable RRAs because of the limited control effect of reflection amplitude, the difficulty of real time controllability and the difficulty of independent controllability of amplitude and phase, which are the main challenges in designing amplitude controllable RRAs.

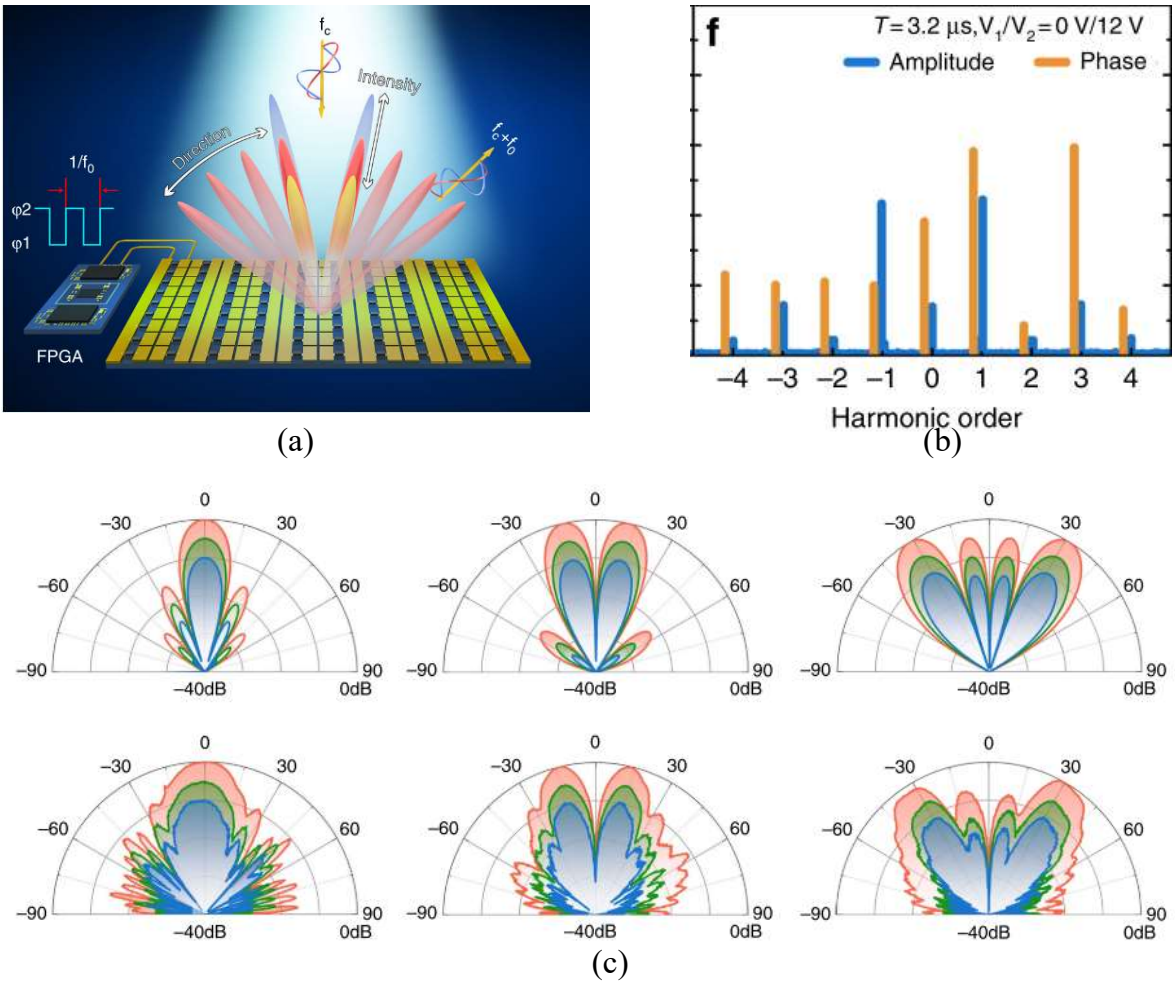

Figure 1.5: TMRA in [43]. (a) Schematic diagram. (b) Time sequence. (c) Generated scattering pattern.

Except frequency domain method, a type of reflection array called time-modulated reflectarray (TMRA) has been increasingly investigated in recent time. TMRA works

by achieving the desired reflection coefficients in the frequency domain (time-average of time-varying reflection coefficients) by means of instantaneously controlling reflection coefficients of TMRA elements in the time domain. As shown in Fig. 1.5, a TMRA with independent control of harmonic amplitude and phase is proposed in [43], and beam scanning using multiple harmonics is achieved separately by applying different time series to the reflection coefficients. In [44], the pattern of a spatial domain multibeam was experimentally verified using multiple harmonic components simultaneously by imposing a pre-designed time sequence, where the main beams of each harmonic component point in a specific direction and do not overlap each other. These works demonstrate the flexible beam control capability of TMRA. In addition, TMRA has the advantages of simple control, real-time control, and high control accuracy. Despite its harmonic components and low efficiency, TMRA has been rapidly and extensively studied in recent years due to its flexible and powerful beam control capability [45–49]. However, it is worth stating that most of the current research on TMRA is mainly focused on beam forming using harmonic components, which is difficult to be directly applied to existing communication systems. On the other hand, it is known from the Fourier transform that the equivalent amplitude of harmonics decreases with increasing harmonics' number, so the efficiency of harmonic-based beam forming is low. In addition, since TMRA is relatively new research, the related theory also needs to be developed and improved. These are the challenges and opportunities for TMRA-related research, and are the issues that this thesis will embark on.

1.3 Research Objectives of Dissertation

The research objectives of dissertation are summarized as follows:

1. Design of TMRA with Real-Time Amplitude Control Ability.

To address the problem that the current RRA can only control the reflection phase, this thesis will design a TMRA with real-time controllable reflection amplitude by introducing a time modulation technique. specifically, this TMRA should have switchable phase or amplitude control capability. In addition, the TMRA should operate at the carrier frequency (center frequency) and be controllable in real time.

2. Analysis Method of TMRA's Efficiency.

A comprehensive and accurate analysis of TMRA's scattering efficiency is essential for evaluating TMRA's performance, but there are no detailed related studies, so it is necessary to propose an analysis method for TMRA's efficiency. In this dissertation, the TMRA efficiency is completely analyzed and defined for the first time. The specialized efficiency definition provides a quantitative method to accurately evaluate TMRA scattering performance and is important for TMRA research.

3. Method to Realizing Beam-Forming with Enhanced Efficiency.

In response to the existing TMRA operating at harmonic frequencies and the problem of low efficiency, this paper will propose a method to achieve enhanced efficiency beam-forming using TMRA at the center frequency. Specifically, the method can achieve simultaneous and independent controllability of amplitude and phase, and operate at the carrier frequency. In addition, the method can achieve higher efficiency compared to the conventional TMRA working with harmonics. In summary, this dissertation focuses on a method to achieve enhanced-efficiency beam-forming using TMRA at the carrier frequency.

1.4 Dissertation Framework

As shown in Fig. 1.6, this dissertation is divided into five chapters which is proceed as follows.

In Chapter 2, the fundamental theory of time-modulated antenna arrays (TMAA) is introduced and extended to TMRA, and the similarities and differences between TMAA and TMRA are discussed. Next, two typical applications of time-modulated arrays are introduced, which are beam-forming and environment sensing. Then the definition of the efficiency of TMRA is analyzed and derived. In addition, The rectangular waveguide (RWG) method for fast and low-cost evaluation of reflection coefficients of RA is introduced and experimentally verified. Finally, performances of the PIN diode used in this dissertation in terms of insertion loss, isolation, and switching speed are experimentally evaluated. Furthermore, simulation models of the PIN diode are compared and discussed to increase the consistency with measured results.

In Chapter 3, a RIS based on a 1-bit TMRA is proposed. The correspondence between the reflection states of 1-bit RRA and two sates of time sequence is firstly found

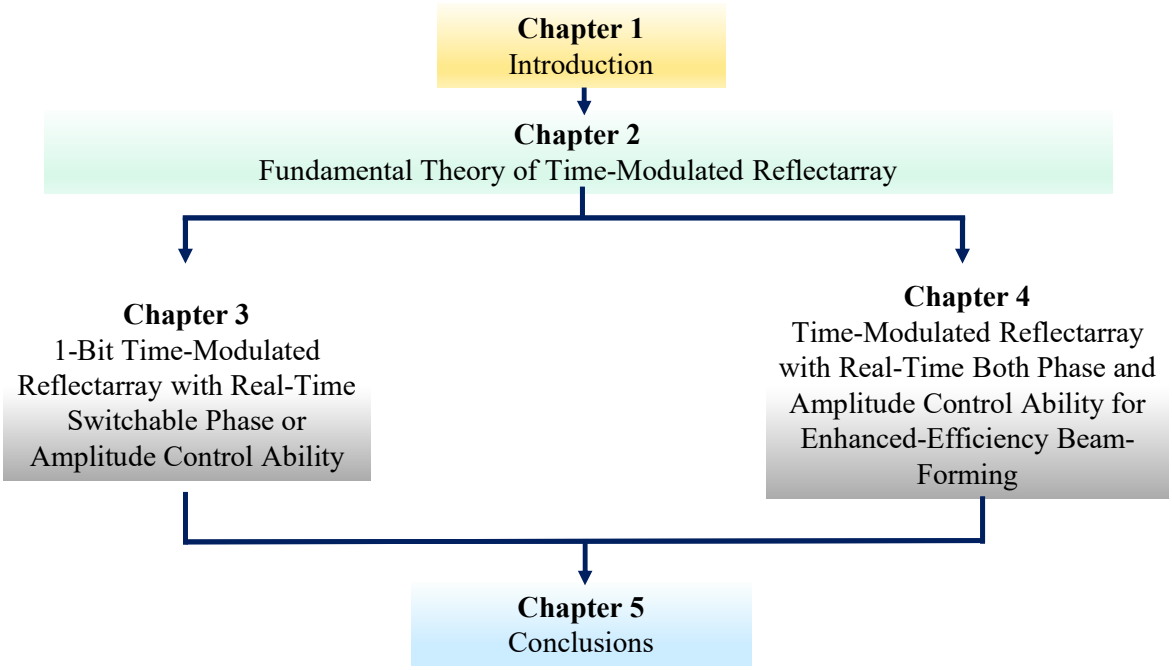

Figure 1.6: Dissertation outline.

and established. By introducing the time modulation into the existing 1-bit RRA, the phase and amplitude of the reflection coefficients of the TMRA element can be controlled separately.

In Chapter 4, a method to achieve enhanced efficiency beam-forming at the carrier frequency using TMRA is proposed. By simultaneously applying the independent amplitude control signal and the phase control signal, the phase and amplitude of the element's reflection coefficient can be controlled independently. Furthermore, the effectiveness of the proposed method is verified by theoretical calculations and experimentally verified by a 1-bit TMRA prototype.

In Chapter 5, finally general conclusions and future works are drawn at the end of the dissertation.

Chapter 2

Fundamental Theory of TMRA

2.1 Theory of TMAA

Antenna arrays are typically composed of multiple identical antenna elements arranged according to certain rules, overcoming the limitations of individual antennas in terms of directivity and gain. Therefore, array antennas find extensive applications in wireless communications and radar domains. Compared to conventional antenna arrays, high-speed RF switches controlled by specific control board (e.g., FPGA, CPLD, MCU) are added to the array structure of a time-modulated antenna array (TMAA), introducing time modulation into the system. The addition of "time" as a new dimension in TMAAs provides an additional degree of freedom compared to traditional arrays. In the frequency domain, time modulation can be obtained by applying Fourier transform to achieve corresponding time weighting. Time weighting can be equivalent to amplitude weighting at the center frequency and amplitude-phase weighting in the side-bands, thus eliminating the reliance on amplitude and phase weighting in traditional arrays when achieving desired radiation characteristics. Consequently, TMAAs can significantly reduce the amplitude dynamic range of excitations and alleviate the design complexity of feed networks compared to traditional arrays while achieving the same radiation characteristics.

The basic physical architecture of an N-element TMAA is shown in the 2.1. Generally, it consists of three main components: the antenna array, the amplitude-phase control network, and the switch control network. Structurally, the most significant difference

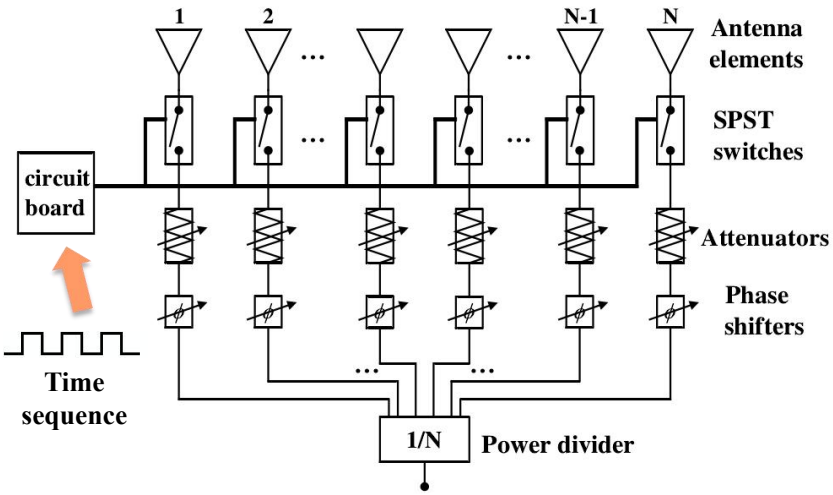

Figure 2.1: The schematic of TMAA system

between TMAA and conventional arrays lies in the fact that each elements in TMAA is connected to one or more high-speed RF switches controlled by control modules. As a result, compared to conventional arrays, TMAA is capable of periodically modulating the signals received or transmitted by the array elements at the RF end using pre-defined switch timing. This modulation enables the achievement of desired radiation performance in TMAA.

For an arbitrary structure of an antenna array consisting of N ideal point sources in space, assuming that the position vector of the i-th antenna element in spherical coordinates is denoted as $\boldsymbol{r}_i$ and can be expressed as

$$\boldsymbol{r}_i = \rho_n(\sin\theta_i\cos\varphi_i, \sin\theta_i\cos\varphi_i, \cos\theta_i) \tag{2.1}$$

where ρ_i represents the distance of the i-th antenna element from the origin of the coordinate system, and θ_i and φ_i represent the elevation angle and azimuth angle, respectively, of the i-th antenna. Assuming the propagation vector of the array is denoted as $\boldsymbol{k}$ which can be expressed as

$$\boldsymbol{k} = \frac{2\pi}{\lambda}(\sin\theta_i\cos\varphi_i, \sin\theta_i\cos\varphi_i, \cos\theta_i) \tag{2.2}$$

where λ represents the wavelength of the array's carrier frequency (also known as the center frequency). The position vector $\boldsymbol{r}_i$, propagation vector $\boldsymbol{k}$, as well as θ_i and φ_i, for the antenna element are illustrated in the figure below

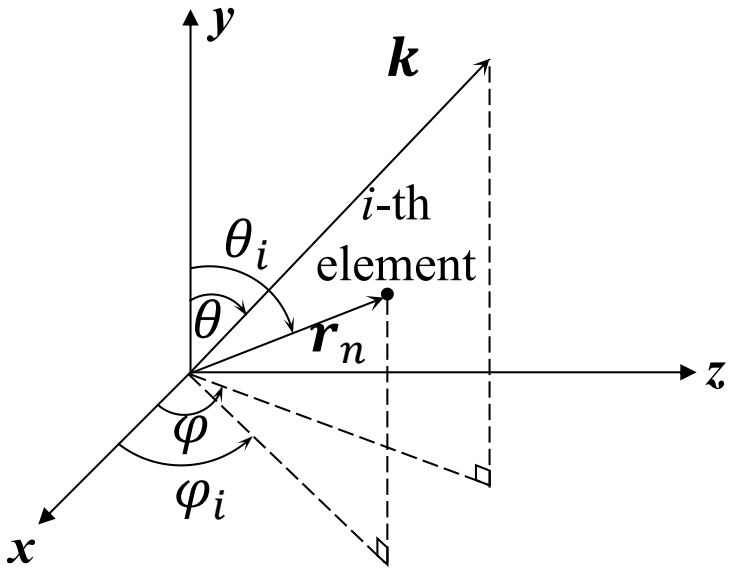

Figure 2.2: Schematic diagram of array antenna position vector and propagation vector

Based on the basic principles of array antennas, the array factor $AF(\theta, \varphi, t)$ at any given observation time t can be expressed as follows

$$AF(\theta, \varphi, t) = e^{j2\pi f_0 t} \sum_{i=1}^{N} I_i e^{j(\boldsymbol{k}\cdot\boldsymbol{r}_i + \alpha_i)} \tag{2.3}$$

where f_0 is the center frequency at which the array operates, An represents the static excitation amplitude generated by the attenuator of the nth antenna element, and an represents the static excitation phase generated by the phase shifter of the nth antenna element.

Since the antenna elements of a time-modulated array are controlled by high-speed RF switches operating periodically, the timing of these RF switches determines the radiation characteristics of the TMAA. Here, we will illustrate the working principle of TMAA

using the most basic form of amplitude modulated time sequences (AMTS). For AMTS, the RF switch timing sequence $U_i(t)$ for each element is given by the following equations

$$U_i(t) = \sum_{m=-\infty}^{m=+\infty} g_i(t - hT_{p,i}) \tag{2.4}$$

$$g_i(t) = \begin{cases} 1, & t_{on,i} < t < t_{off,i} \\ -1, & 0 < t < t_{on,i} \ or \ t_{on,i} < t < T_{p,i} \end{cases} \tag{2.5}$$

The operational states of $U_i(t)$ are illustrated in the following figure, where t_i represents the conduction time within the switching modulation period $T_{p,i}$. The operational states of $U_i(t)$ are illustrated in the Fig. 2.3.

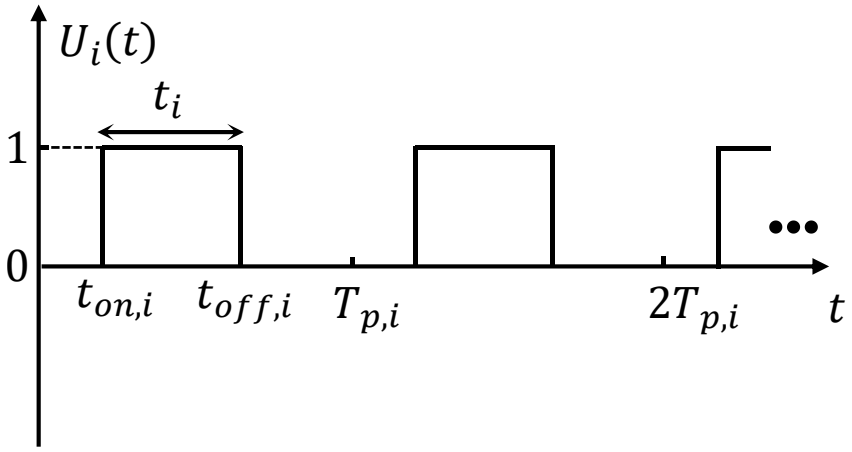

Figure 2.3: Amplitude modulation time sequence

The TMAA, controlled by RF switches, can be equivalently represented by modulating the static excitation with the modulation term $U_i(t)$. Consequently, the expression for the array factor $AF(\theta, \varphi, t)$ of TMAA can be obtained as follows

$$AF(\theta, \varphi, t) = e^{j2\pi f_0 t} \sum_{i=1}^{N} I_i U_i(t) e^{j(\boldsymbol{k}\cdot\boldsymbol{r}_i + \alpha_i)} \tag{2.6}$$

Since $U_i(t)$ is a periodic function in the time domain, it can be expanded into a Fourier series

$$U_i(t) = \sum_{h=-\infty}^{h=+\infty} a_{i,h} e^{j2\pi h F_{p,i} t} \tag{2.7}$$

where $a_{i,h}$ is the Fourier coefficient of the h-th harmonic of the modulation pulse for the i-th element and can be expressed as

$$\begin{aligned} a_{i,h}(t) &= \frac{1}{T_{p,i}} \int_0^{T_{p,i}} g_i(t) e^{-j2\pi h F_{p,i} t} \\ &= \begin{cases} \dfrac{\sin\left(\pi h \dfrac{t_{off,i} - t_{on,i}}{T_{p,i}}\right)}{\pi h} e^{-j\pi h F_{p,i}(t_{off,i}+t_{on,i})}, & h \neq 0 \\ \dfrac{t_{off,i} - t_{on,i}}{T_{p,i}}, & h = 0 \end{cases} \\ &= \begin{cases} \tau_i \operatorname{sinc}(\pi h \tau_i) e^{-j\pi h(\tau_{off,i}+\tau_{on,i})}, & h \neq 0 \\ \tau_i, & h = 0 \end{cases} \end{aligned} \tag{2.8}$$

where the $\tau_{on,i}$ and $\tau_{off,i}$ are the normalized turn on/off moments of the i-th element and are defined by $\tau_{on,i} = t_{on,i}/T_{p,i}$ and $\tau_{off,i} = t_{off,i}/T_{p,i}$. The τ_i is the switch-on duration and is defined by $\tau_i = t_i/T_{p,i}$ or $\tau_{off,i} - \tau_{on,i}$. The modulation frequency $F_{p,i}$ is defined as the inverse of the modulation period. Therefore, the array factor of TMAA can be expressed as

$$AF(\theta, \varphi, t) = \sum_{h=-\infty}^{h=+\infty} e^{j2\pi(f_0 + hF_p)t} \sum_{i=1}^{N} a_{i,h} I_i(t) e^{j(\boldsymbol{k}\cdot\boldsymbol{r}_i + \alpha_i)} \tag{2.9}$$

where the amplitude term of a_i and the static excitation amplitude An both control the excitation amplitude of the array element and have the same physical effect, and are therefore called time modulation (TM) excitation amplitude. Similarly, the phase term of a_i is referred to as the TM excitation phase. Furthermore, it can be found that the amplitude of a_i is controlled only by the on-time τ_i, while the phase of a_i is controlled

by both $\tau_{on,i}$ and $\tau_{off,i}$. It is also worth stating that the array factor of TMAA contains an infinite number of harmonic frequency components, which is an important feature that distinguishes TMAA from conventional antenna arrays. The complete TMAA array factor in frequency domain can be expressed as

$$AF_h(\theta,\varphi) = \begin{cases} \sum_{i=1}^{N} \tau_i \operatorname{sinc}(\pi h \tau_i) e^{j\pi(\tau_{off,i}+\tau_{on,i})} e^{j(\boldsymbol{k}\cdot\boldsymbol{r}_i+\alpha_i)}, & h \neq 0 \\ \sum_{i=1}^{N} \tau_i I_i(t) e^{j(\boldsymbol{k}\cdot\boldsymbol{r}_i+\alpha_i)}, & h = 0 \end{cases} \tag{2.10}$$

It can be observed that due to the modulation by periodic pulse signals, the TMAA generates side-band radiation at the side-band frequencies according to the theory of Fourier series. If only the carrier frequency component is utilized, it is necessary to suppress the undesired side-band radiation to reduce energy loss. However, on the other hand, since the TM excitation at the side-band frequencies is controllable, the desired beam-forming effects can be achieved using the side-band frequency components. Additionally, it can be noted that in AMTS, only the TM excitation amplitude is present at the carrier frequency.

2.2 Theory Expansion to TMRA

The antenna array is excited through feeding lines, allowing the implementation of TM excitation by inserting high-speed RF switches between each feeding line. In other words, TMAA achieves TM function by directly controlling the temporal characteristics of the excitation (input current) in the feeding lines. While the RA utilizes spatial feeding method, where the aperture excitation (induced current) for each array element comes from a common feeding source and cannot be independently controlled by manipulating the feeding source. Therefore, when extending the concept from TMAA to TMRA, the control objective shifts from excitation in the feeding line to aperture excitation. In terms of the physical process, the excitation of each element in RA is derived from the reflection of incident waves. Hence, the fundamental principle behind designing TMRA lies in achieving independent control of the reflection coefficients of each element. On the other hand, the key aspect of TM is the physical implementation of the time sequence, that is, controlling the variation of element excitation with respect to time

sequence. In summary, the core of designing TMRA is to independently control the reflection coefficients of each element and to dynamically switch between these reflection coefficients in real time according to the pre-designed time sequence. As shown in 2.4, a typical TMRA system consists of three main components: the feeding source, the RRA, and the control board that generates the time sequence control signals. In addition, it is evident that the previous works mentioned in Chapter 1, as referred to as [43] and [44], utilize the strong reflection state of RRA to correspond to the high-level state ("1" state) of AMTS, and the weak reflection state of RRA to correspond to the low-level state ("0" state) of AMTS. They switch between the strong and weak reflection states according to a pre-designed time sequence, thereby designing a TMRA with a specific scattering pattern.

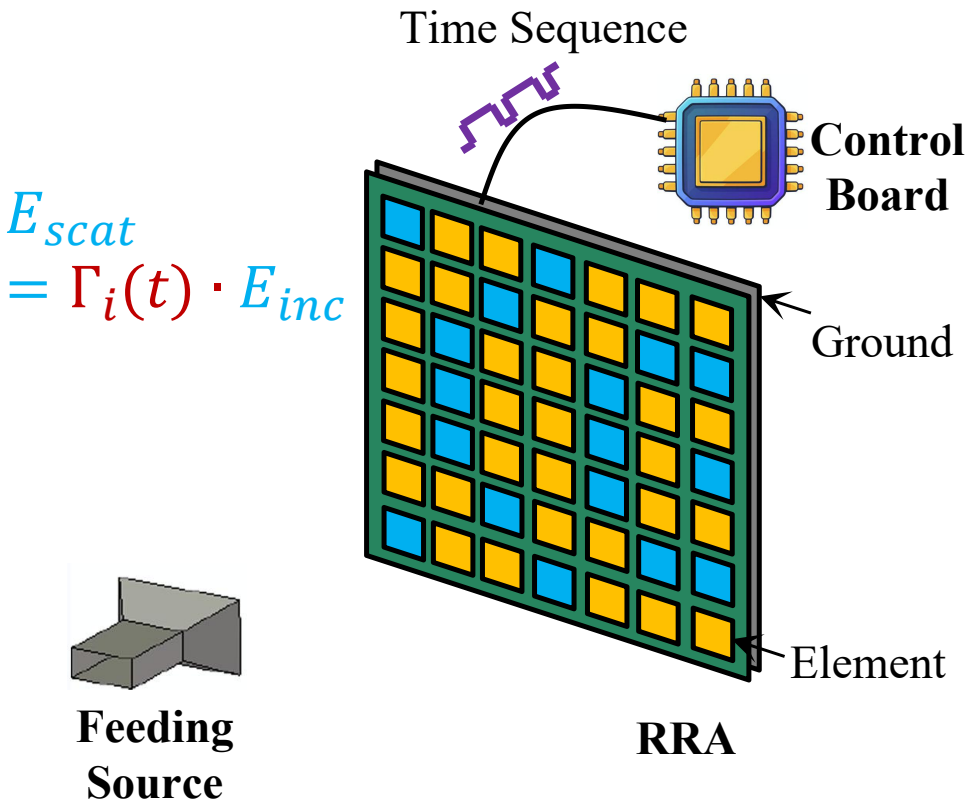

Figure 2.4: The schematic of TMRA system.

2.3 Efficiency Definitions of TMRA

The analysis of efficiency is essential to assess the TMRA performance, but there is a lack of relevant rigorous definitions. Therefore, it is necessary to propose an analysis method for TMRA efficiency, which is of great importance for the study of TMRA. Since the feeding source can be placed in the far-field or near-field region of the TMRA depending on the operating scenario, it is necessary to discuss these two scenario separately.

2.3.1 Near-Field Incidence Scenario

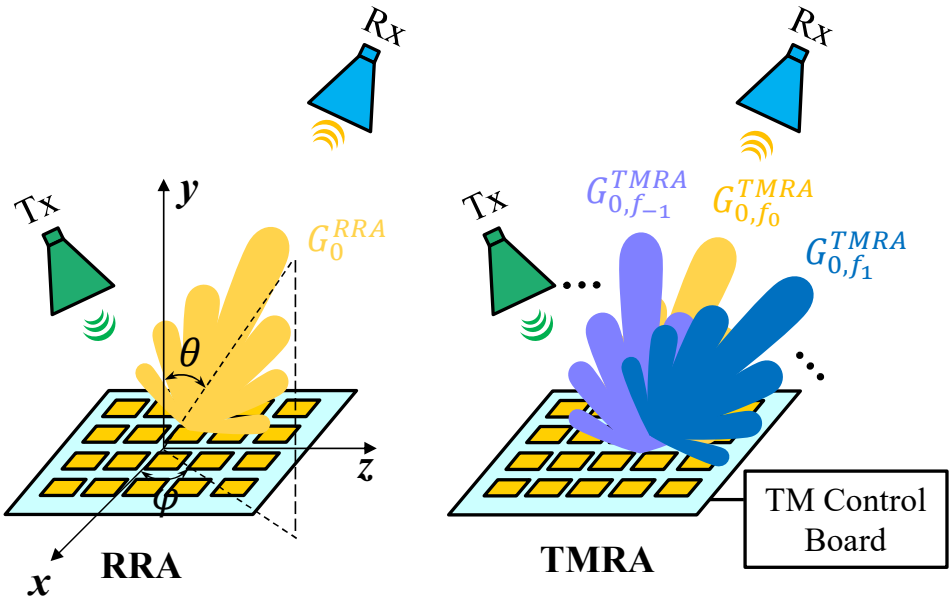

Figure 2.5: Near-field Incidence Scenario.

As shown in Fig. 2.5, when the feeding source is located in the near-field region of the TMRA's aperture, the aperture is non-uniformly illuminated, similar to the case of a reflectarray antenna (RAA). Therefore, it is appropriate to analyze TMRA efficiency using the relevant definitions of aperture efficiency from RAA theory. For an RAA with an aperture area of A, the theoretical maximum directivity can be given by the following equation [50]:

$$D_{max} = \frac{4\pi A}{\lambda^2} \tag{2.11}$$

where λ is the wavelength of the operating frequency.

According to RA theory [51] [9], the ratio of the measured gain (G^{RRA}) to the theoretical maximum directivity represents the aperture efficiency of the RAA in a certain direction (θ, φ), and the definition is as follows [9]:

$$\eta_{ap}^{RRA}(\theta, \varphi) = \frac{G^{RRA}(\theta, \varphi)}{D_{max}} \tag{2.12}$$

For TMRA with the same aperture, because of time modulation, the scattered field of TMRA generates an infinite number of harmonic frequency components, as shown in the figure. Typically, we are only interested in the scattering characteristics of a specific harmonic frequency component (e.g., h-th harmonic component). Therefore, the aperture efficiency of h-th harmonic frequency component in a particular direction can be defined as

$$\eta_{ap,f_h}^{TMRA}(\theta, \varphi) = \frac{G_{f_h}^{TMRA}(\theta, \varphi)}{D_{max}} \tag{2.13}$$

Usually, we are primarily concerned with the maximum aperture efficiency. Hence, the maximum aperture efficiency of TMRA for the h-th harmonic can be given as:

$$\eta_{ap0,f_h}^{TMRA} = \frac{G_{0,f_h}^{TMRA}}{D_{max}} \tag{2.14}$$

where G_0 is the maximum gain of the entire observation range.

2.3.2 Far-Field Incidence Scenario

As shown in Fig. 2.6, when the feed source is located in the far-field region of the TMRA's aperture, the aperture is uniformly illuminated. It is well known that the Radar

Cross Section (RCS) is a physical quantity used to evaluate the scattering intensity of a target after being illuminated by incident waves in the far-field region. Therefore, it is appropriate to analyze TMRA efficiency using the relevant definitions of RCS. For a metal sheet, when a plane wave is incident from the (θ_i, φ_i) direction, the bistatic RCS (BRCS) measured in the $(\theta_i, \varphi_i - \pi)$ direction can be denoted as σ^{MS} and defined as follows [52]:

$$\sigma^{MS} = \lim_{r\to\infty} 4\pi r^2 \frac{|\boldsymbol{E}^{scat}|^2}{|\boldsymbol{E}^{inc}|^2} \tag{2.15}$$

where $\boldsymbol{E}^{scat}$ is the scattered field and $\boldsymbol{E}^{inc}$ is the field incident at the target. r is the distance from the scatterer to the point where the scattered power is measured.

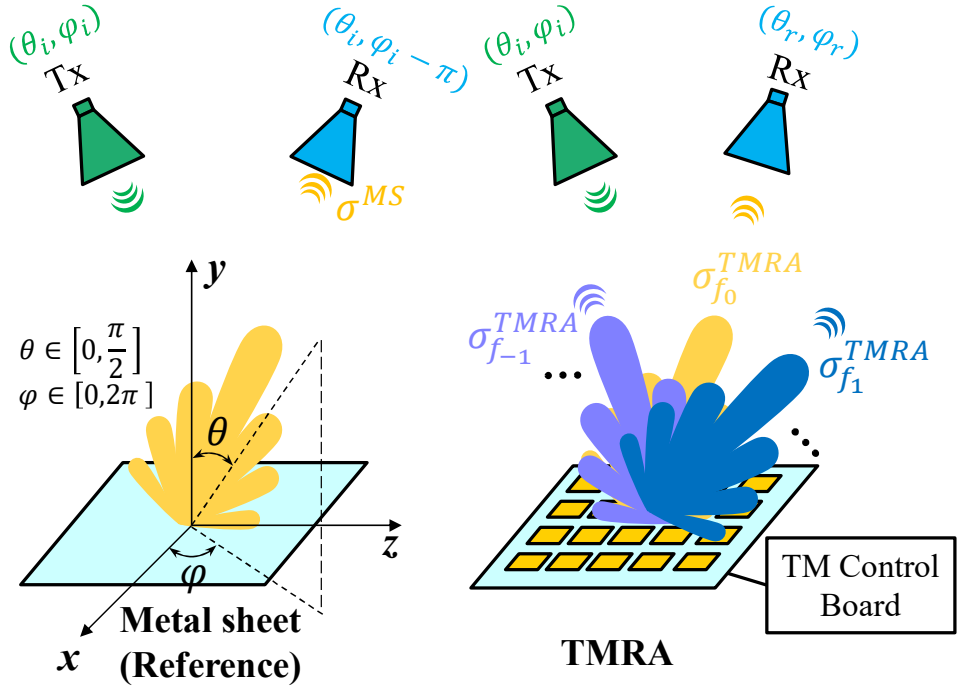

Figure 2.6: Far-field Incidence Scenario.

In terms of TMRA, when TMRA is illuminated by the same incident wave, TMRA generates an infinite number of harmonic frequency components. Therefore, we can

measure the BRCS of different harmonics at different angles. We define these BRCS values as time-modulated RCS (σ^{TMRA}). In RCS measurement, the RCS of the target object needs to be normalized to the RCS of a standard reference (such as a metal sphere or metal sheet). Inspired by this, we define the efficiency of a particular harmonic component (e.g., h-th harmonic component) of TMRA as the ratio of the time-modulated RCS of h-th harmonic component to the RCS of a metal sheet with the same aperture area at measured frequency of f_h. It can be represented as:

$$\eta_{f_h}^{TMRA}(\theta_r, \varphi_r) = \frac{\sigma_{f_h}^{TMRA}(\theta_r, \varphi_r)}{\sigma_{f_h}^{MS}} \tag{2.16}$$

Usually, we are primarily concerned with the maximum efficiency. Hence, the maximum efficiency of TMRA for h-th harmonic can be given as:

$$\eta_{0,f_h}^{TMRA}(\theta_r, \varphi_r) = \frac{\sigma_{0,f_h}^{TMRA}}{\sigma_{f_h}^{MS}} \tag{2.17}$$

where σ_{0,f_h}^{TMRA} represents the maximum value of the time-modulated RCS of the h-th harmonic component at different test angles. It can be observed that TMRA efficiency represents the scattering ability of TMRA relative to a standard reference (metal sheet) with the same aperture area.

2.4 Applications of TMRA

Leveraging its flexible beam control and harmonic characteristics, TMRA finds extensive utility in diverse domains, including beam-forming [43,46–49], direction-of-arrival (DOA) estimation [53,54], wireless communication [55–57], radar deception [58–60], camouflaging [61] and imaging [62, 63]. This paper introduces two prototypical applications, namely beam-forming and environment sensing, to illustrate the fundamental workflow of TMRA and showcase its potential in a broader range of applications.

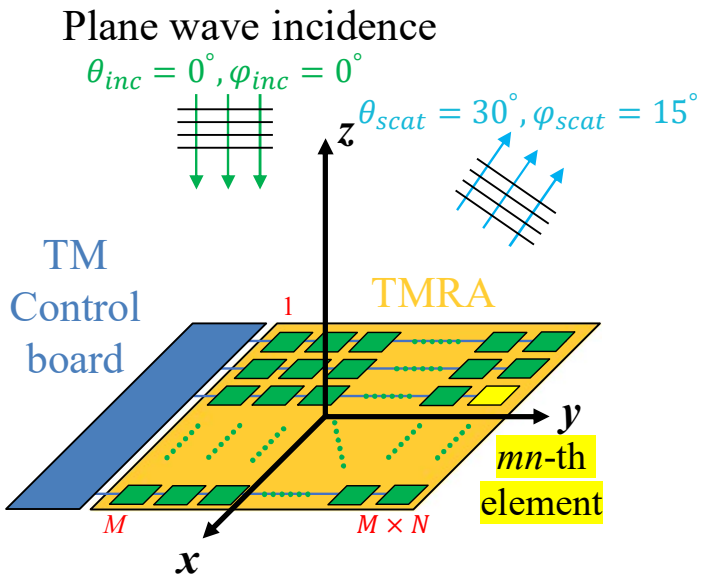

Figure 2.7: TMRA configuration and beam-forming objective.

2.4.1 Beam-Forming

As demonstrated by Eq. (2.8), TMRA possesses the capability to simultaneously manipulate the amplitude and phase of the reflection coefficient at the harmonic frequency, enabling the realization of beam-forming. In this study, TMRA is employed to achieve a scattering pattern with ultra-low side-lobes, a task that is challenging to accomplish with conventional reflection arrays due to the requirement for a significant amplitude taper at the aperture. Illustrated in Fig. 2.7, a TMRA comprising 10×10 elements is considered, with a vertically incident plane wave.

The objective of beam-forming is to achieve a 30 dB Chebyshev Pattern while redirecting the scattered beam towards a specific direction at coordinates $(30°, 15°)$. The design procedures, as depicted in 2.8, involves several steps. Initially, the desired scattering beam-forming objective is defined. Subsequently, the calculation of the required distribution of reflection amplitude and phase to achieve the target is performed, as exemplified in Fig. 2.8(b) and Fig. 2.8(c).Next, the time sequence variables, τ_i and $\tau_{on,i}$, are calculated using Eq.(2.8), with the results displayed in Fig. 2.8(d) and Fig. 2.8(e). Finally, by implementing the calculated time sequences, a time-modulated scattering

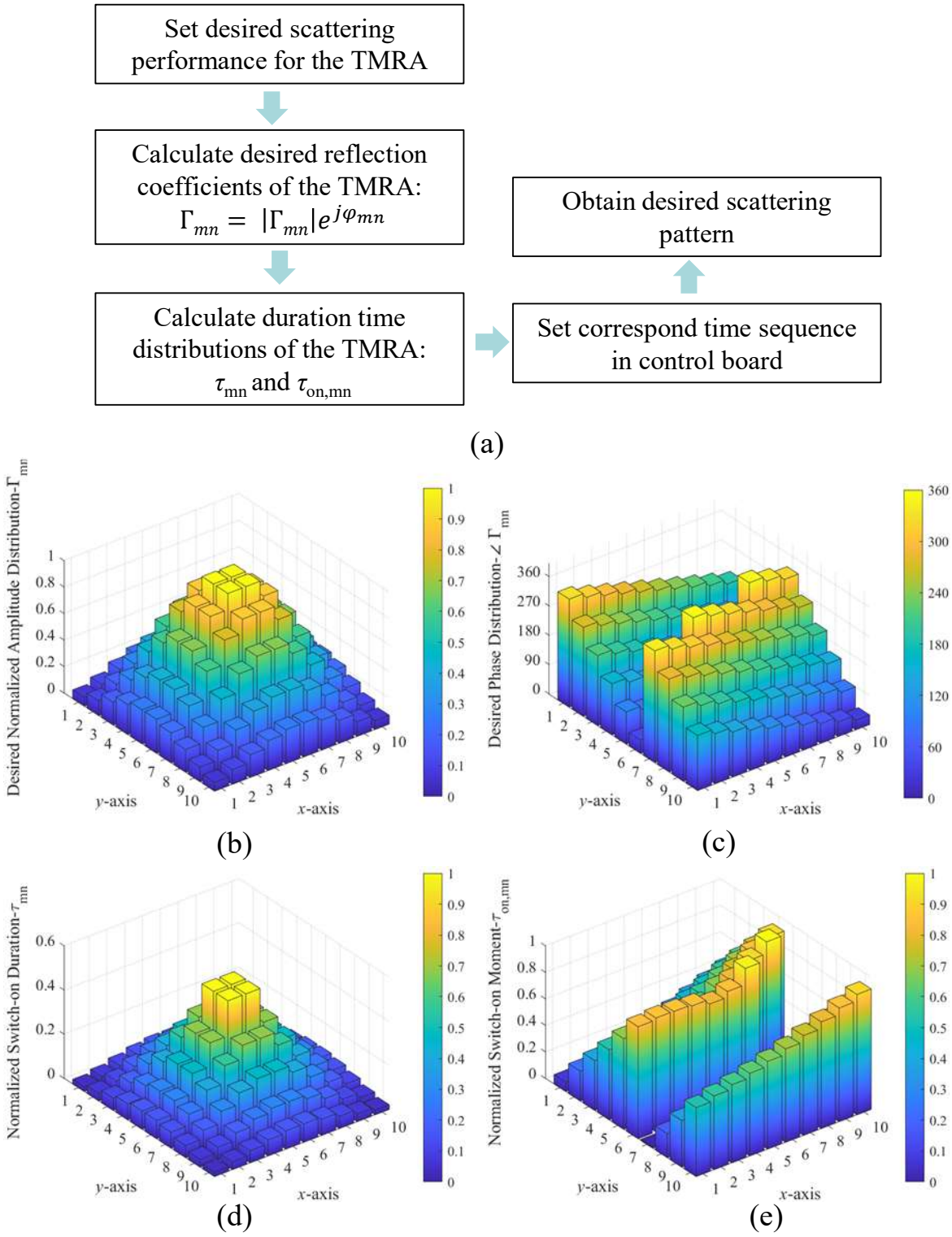

Figure 2.8: Realization of beam-forming by TMRA. (a) Design procedure. (b) Desired amplitude. (c) Design phase. (d) Calculated τ_i. (e) Calculated $\tau_{on,i}$.

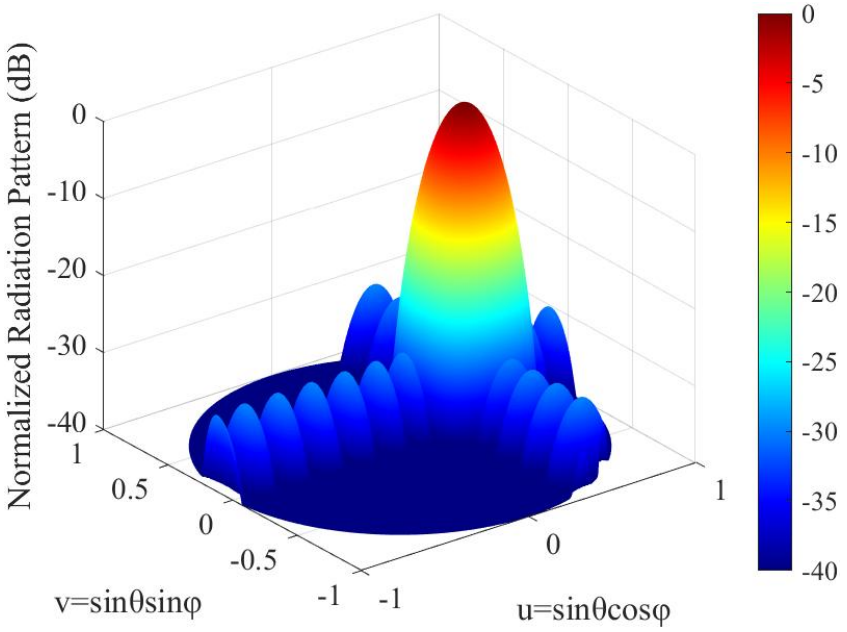

Figure 2.9: Obtained scattering pattern.

beam is generated, as depicted in Fig. 2.9. It is noteworthy that the achieved scattering beam aligns perfectly with the intended beam-forming goal.

2.4.2 Environment Sensing

As shown in Fig. 2.10(a), a specific set of time function, called scanning time sequence, is applied to the array. Specifically, array's elements are "lit up" in sequence and remain "off" at other times, as expressed as

$$g_n(t) = \begin{cases} 1, & \frac{n-1}{N}T_p \le t \le \frac{n}{N}T_p \\ -1, & \text{elsewhere} \end{cases}, 1 \le n \le N \tag{2.18}$$

The green zone corresponds to "1" state and others correspond to "0" state in Fig. 2.10(a). Note that the TM period $T_{p,i}$ is same for each element.

It can be referred from Eq. (2.8) and Eq. (2.18) that by the utilizing scanning time sequence the equivalent excitations of different harmonics would have same amplitudes

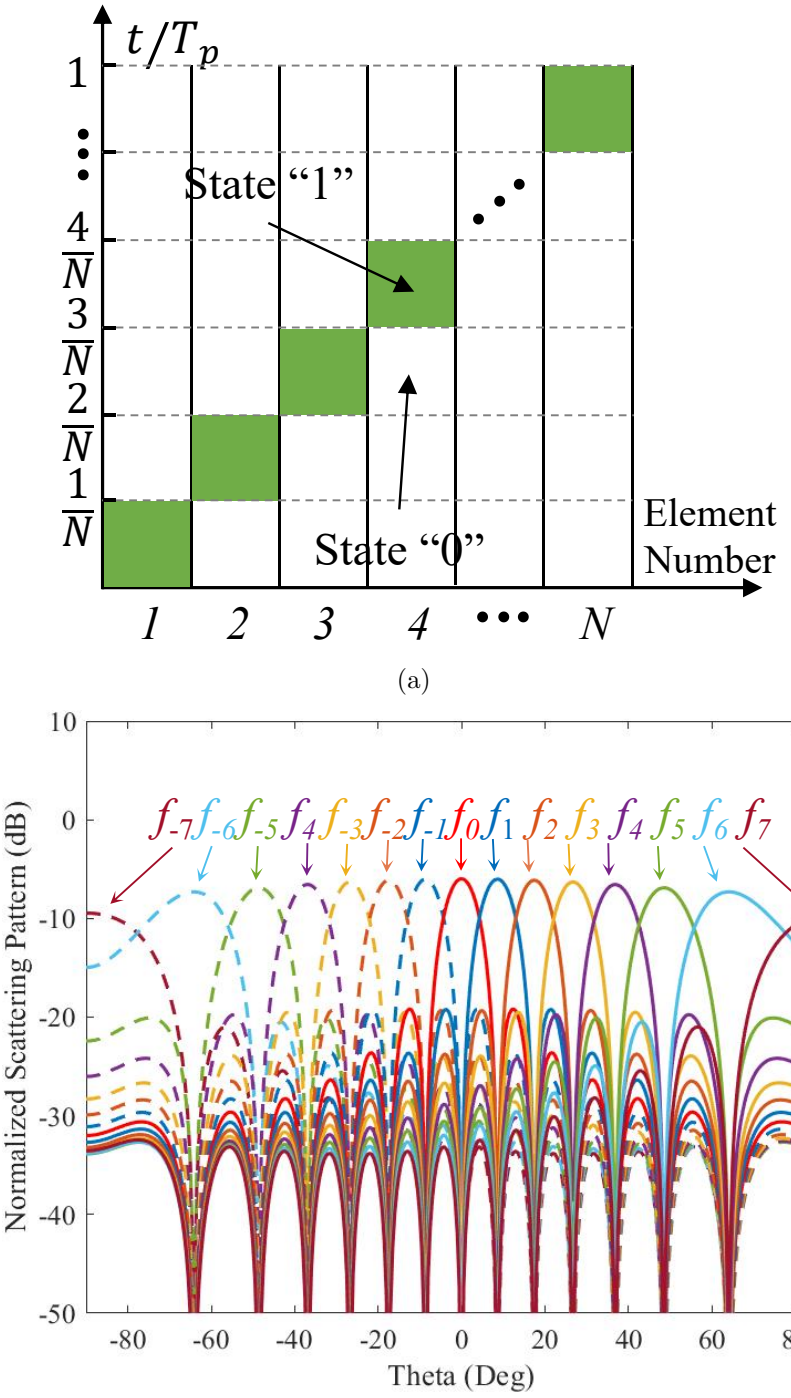

Figure 2.10: TMRA for environment sensing. (a) Scanning time sequence. (b) Corresponding scattering pattern

and progressive phases. This would generate a specific set of scattering patterns. It can be observed that the main beams of different harmonics appear sequentially and point to adjacent directions as the harmonic order changes, achieving multi-beam coverage in a large angular range. This unique combination of harmonic scattering patterns is only determined by time sequence and element number. This unique combination of harmonic scattering patterns is named multi-harmonic multi-beam (MHMB) characteristic, which is only determined by time sequence and element number. That is, the deviation angles of each harmonic beam direction relative to the center frequency's beam direction are known. As a result, the beam direction of a certain harmonic can be easily derived if its order and the beam direction of center frequency is known, which is the principle for applying 1-bit TMRA to realize DOA estimation and object localization.

Fig. 2.11(a) shows the schematic diagram of TMRA applied to DOA estimation. Both the receiving antenna (Rx) and the incoming signal to be recognized are located in the far-field region of the TMRA. The angles of the Rx and the incoming signal with respect to the normal of the aperture of TMRA are θ_r and θ_i, respectively. When the incoming signal with an operating frequency of f_0 propagates to the TMRA controlled by the scanning time function with a TM frequency of F_p, it would be reflected towards different directions with different frequencies based on HMHB characteristic. Now we have $\theta_i = \theta_r + \theta_h$, where θ_h is the angle between the direction of the received harmonics and the Rx direction. Based on the aforementioned mapping relationship, the DOA can be derived from the spectrum response of signal captured by Rx. Once the dominant harmonic component (has maximum power level), denoted as f_{target}, is found from the spectrum response, the order of dominant harmonic can be obtained as $h_{target} = \frac{f_{target} - f_0}{F_p}$. Then θ_h can be obtained from the Fig. 2(b) by comparing the beam direction difference with f_{target} and f_0. As a results, θ_i is derived, indicating a completed DOA estimation of incoming signal.

Furthermore, object localization can also be realized based on the MHMB characteristic of TMRA. In this application, the antenna first sends a CW signal with frequency of f_0 to the TMRA, and a specific harmonic component (denoted as f_{target}) of the scattering waves would impinge the target, as shown in Fig. 2.11(c). Then the target would reflect the wave of f_{target} component towards TMRA. Accordingly, f_{target} component would be scattered again under the effect of TM, as shown in Fig. 2.11(d). The following pro-

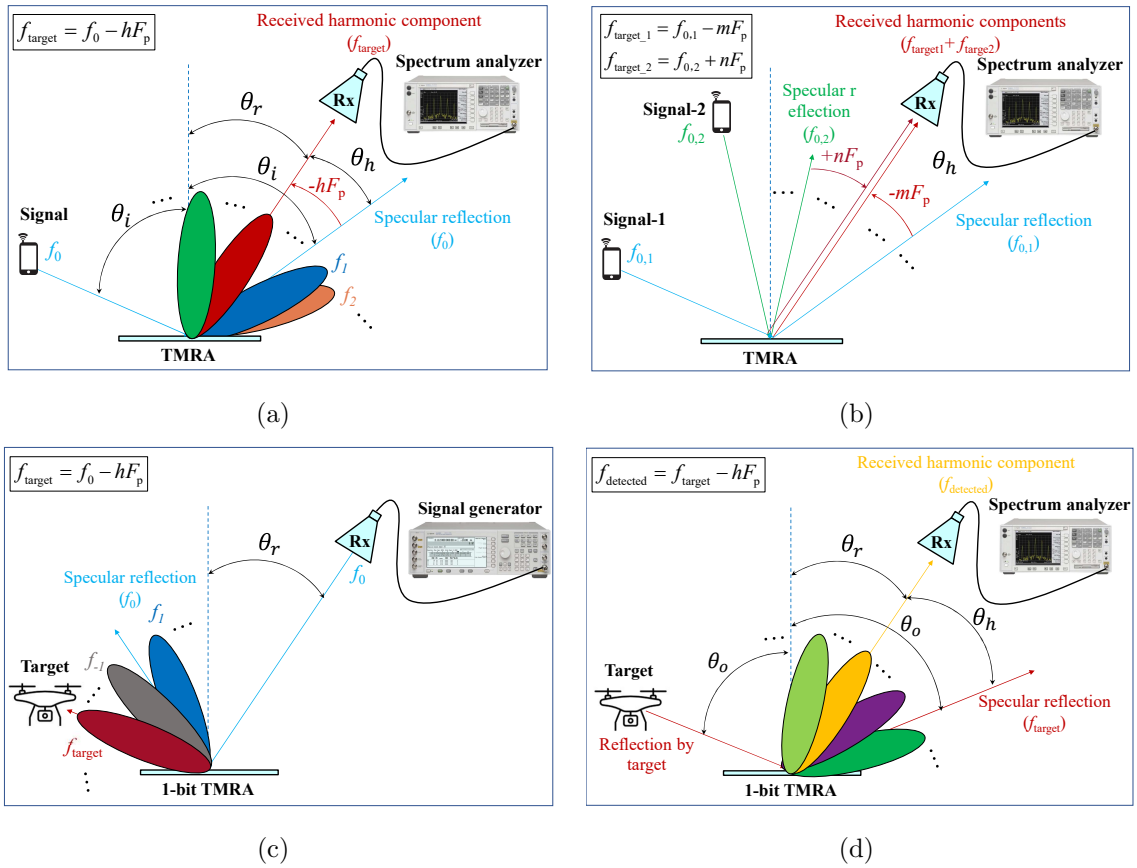

Figure 2.11: Principles and methods of environmental perception. (a) Single target DOA estimation. (b) Multi-target DOA estimation. (c) Single target object localization: first step. (d) Single target object localization: second step.

cedures are as same as the analysis of DOA estimation. Note that if the final detected dominant harmonic component is $f_{detected}$, the actual order of harmonic which carries target's angular feature $h_{target} = \frac{1}{2}h_{detected} = \frac{f_{detected} - f_o}{F_p}$. Thus, θ_h is obtained and the direction of object can be derived by $\theta_o = \theta_r + \theta_h$.

Since different directions correspond to different harmonic components, it is possible to simultaneously realize multi-target perception. Limited by the paper length, here we only give an example of multi-target DOA estimation scenario to concisely demonstrate the operating principle. As shown in Fig. 2.11 (b), there are two user signals with

different operating frequencies of $f_{0,2}$ and $f_{0,2}$. Different from the single target scenario, two dominant harmonic components would appear in the spectrum response results and correspond to two detected directions. The other procedure of perception is as same as single target scenario. Note that the operating frequencies of targets should be different to each other to ensure the TM effect. Moreover, to avoid overlap of targets' signal, the operating frequencies of each target $f_{0,m}$ should satisfy the following equation: $f_{0,i} - f_{0,j} \neq nF_p, i, j \in m, i \neq j, n \in \mathbb{Z}$.

The aforementioned examples illustrate that the scattering characteristics of TMRA are entirely governed by the applied time sequence, thus presenting notable advantages such as effortless control, real-time adjustment, and a high degree of control freedom. These attributes make TMRA particularly well-suited for RIS applications.

2.5 Fast and Low-Cost Evaluation Methods for Reflectarray Element's Reflection Coefficient

The Rectangular Waveguide (RWG) Method [64] is a common test method to verify the performance of periodic structures. This method places the tested elements on the cross-section of a rectangular waveguide and uses the current along the metallic walls of the waveguide to simulate an infinitely large periodic structure through the principle of current imaging. In a confined space, this method achieves the purpose of testing periodic structures with a small number of elements, making it naturally cost-effective for electronically controlled periodic structures that may have higher production costs. However, this method has two limitations: First, according to the principle of mirroring, the current mirroring on the waveguide walls and the current direction of the periodic structure are shown in Fig. 2.12(a). Strictly speaking, this method is only applicable to elements structures that are mirror-symmetric along both the x and y directions. Second, due to the limitations of waveguide transmission modes, the electromagnetic waves incident on the elements surface are mainly in the form of obliquely incident TE_{10} mode waves, as shown inFig. 2.12(b). The oblique incidence angle θ satisfies the equation

$$\sin\theta = \frac{\lambda_0}{2a} \tag{2.19}$$

where λ_0 is the free-space wavelength corresponding to the operating frequency, and a is the length of the longer side of the waveguide cross-section. For different frequencies, the oblique incidence angle has a fixed specific value. Taking the WR-90 waveguide used in this work as an example, at 10 GHz, the oblique incidence angle is 41°.

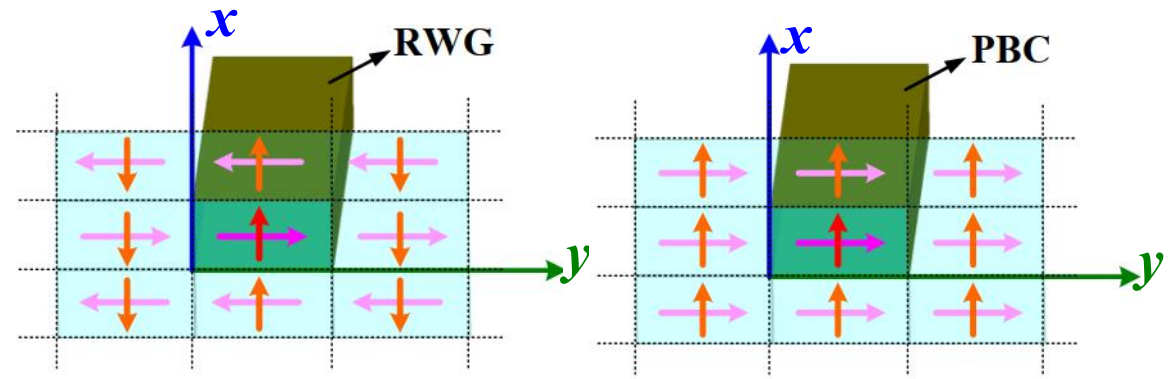

(a)

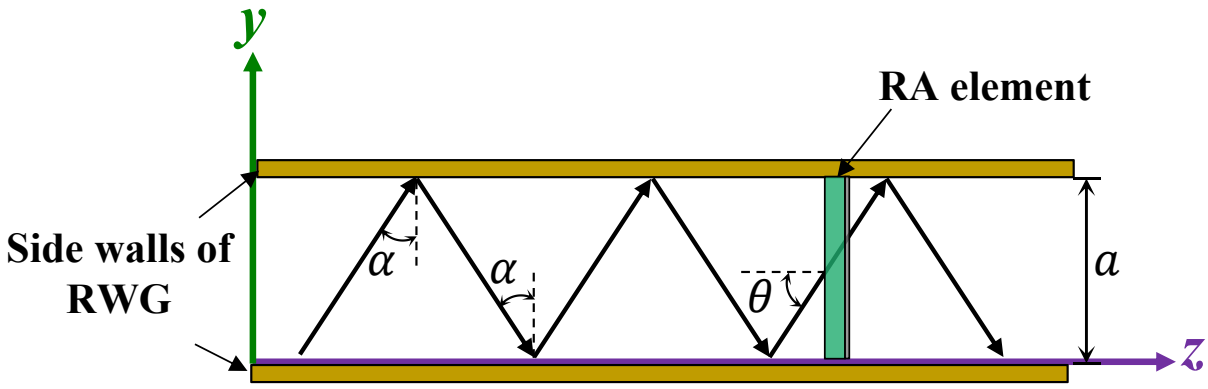

(b)

Figure 2.12: Illustration of RWG method. (a) Boundary difference. (b) Oblique incidence in waveguide.

Here we use the RWG method to test RA elements with rectangular patch shapes. It is important to emphasize that the results obtained from the RWG method cannot be directly compared with the reflection results of periodic elements under normal incidence. The purpose of using the waveguide method here is to simulate the characteristics of periodic structures in a fast, convenient, and cost-effective way. The goal is to validate

the agreement between the waveguide-based simulation results and the experimental results, thus confirming the reliability of the simulation.

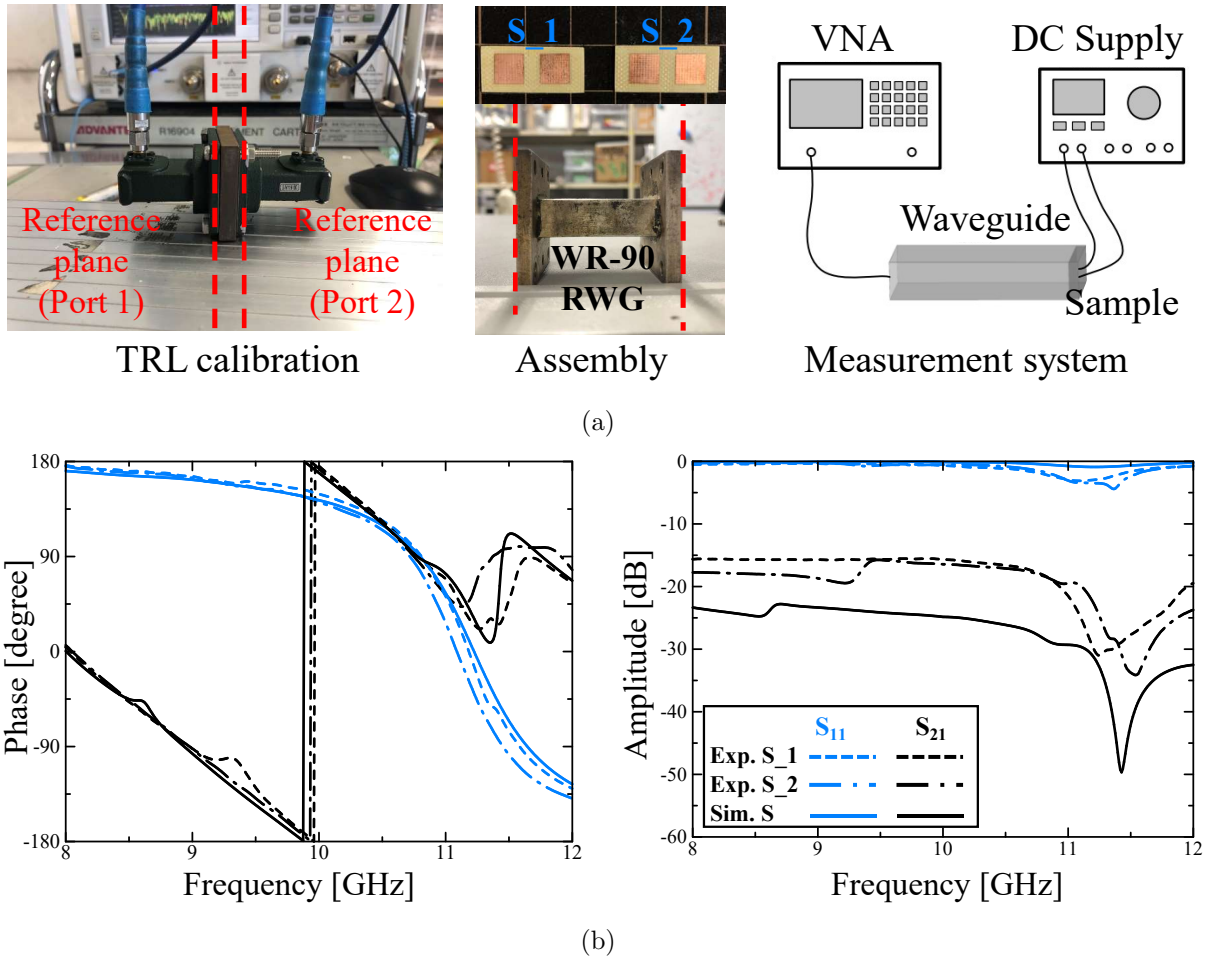

Figure 2.13: Experimental validation of RWG method. (a) Experimental setup. (b) Measured results.

As shown in Fig. 2.5(a), two RA element prototypes were designed and fabricated. It should be noted that the length of the longer side of the standard rectangular waveguide cross-section is nearly twice the length of the shorter side. In order to make the equivalent array formed by mirroring the RA unit through the RWG closer to the infinite array, the RA element prototypes for testing were designed in a 1×2 layout with dimensions

of 20 mm × 10 mm, which closely matched the cross-section of the WR-90 waveguide (dimensions of 22.86 mm × 10.16 mm). The fabricated elements were placed on a section of the RWG's cross-section, and the surfaces of the RA elements prototypes were aligned with the flange surface of the RWG. The measurement system for measuring the elements reflection coefficients was set up as shown in Fig. 2.5(a). The vector network analyzer (VNA) model used in the experiment was Keysight N5224A. Note that the through-reflect-line (TRL) calibration method was employed to move the measurement plane to the surface of the test sample.

The experimental and simulation results are shown in Fig. 2.5(b), and it can be observed that the test results of both RA element prototypes are in good agreement with the simulation results, validating the accuracy of the RWG method.

2.6 Experimental Verification of PIN Diode's Performance and Evaluation of Its Modeling Accuracy

In this dissertation we used PIN diode-based RRA to design and implement TMRA. Therefore, it is necessary to verify if the performance of the PIN diode meets the requirements for time modulation. Additionally, the accuracy of diode modeling in the simulation also affects the performance of the final TMRA design, thus it is necessary to evaluate the accuracy of the diode simulation model. The selected PIN diode model is MACOM MA4AGP910, and the microscopic photos of the diode are shown in Fig. 2.14.

First, we measured the S-parameters to evaluate the on/off characteristic characteristics of the diode. The measurement system is shown in Fig. 2.15(a). The diode was soldered and fixed in the middle of a microstrip transmission line, and we applied the bias voltage from the DC supply to the diode's terminals using probes to control its on/off state. The microstrip transmission line was fixed using a fixture model Anritsu 3680-20, with the fixture's ends connected to the two ends of the VNA. Prior to measurement, TRL calibration was performed to move the measurement plane to the diode's terminals and eliminate the influence of cables, fixture, and transmission lines on the results.

The experimental results are shown in Fig. 2.15(b). As it can be seen, when the diode

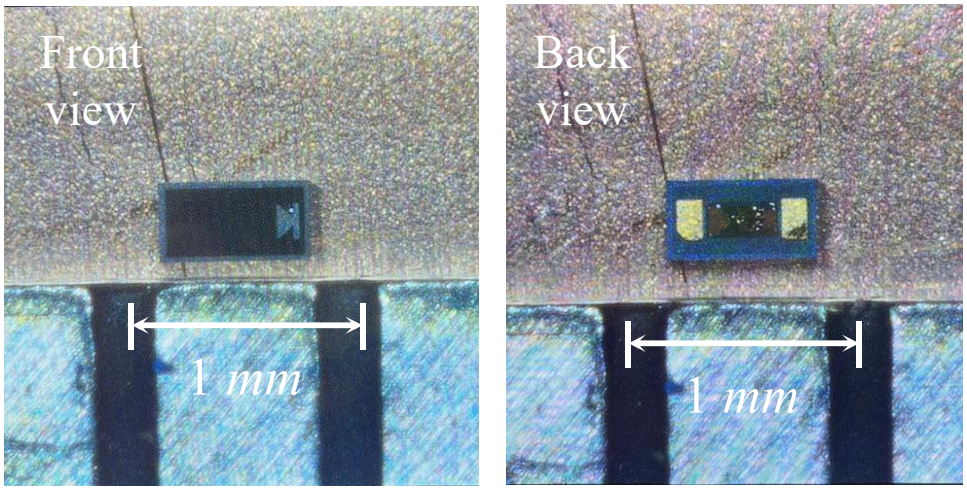

Figure 2.14: Photo of selected diode.

is in the off state, the amplitude of the transmission coefficient ($|S_{21}|$) at the operating frequency of 10 GHz is -12.3 dB, indicating good isolation. On the other hand, when the diode is in the on state, $|S_{21}|$ at the operating frequency of 10 GHz is only -0.6 dB, demonstrating low insertion loss. The discrepancies between measured data and manufacture's data are mainly caused by the capacitance between the soldering pads on the both sides of diode and the undesired scattering from the two ends of the fixture. These results indicate that the selected PIN diode exhibits excellent on/off characteristics at the operating frequency of 10 GHz and is suitable for designing RRA based on PIN diodes.

Furthermore, the switching speed of the PIN diode is also measured and evaluated, which is crucial for successfully achieving time modulation. The measurement system is shown in Fig. 2.16(a). We generated two synchronized square wave signals using a function generator, with one signal directly connected to an oscilloscope as a reference signal, and the other signal passing through the diode before entering the oscilloscope as the measured signal. We use a grounded matching load to provide stable grounding and potential for the measured signal. The testing method for the diode in this experiment is the same as described earlier. The function generator model used is Agilent 33250A, and the oscilloscope model used is IWATSU DS-5105B. The time period (T_p) of the

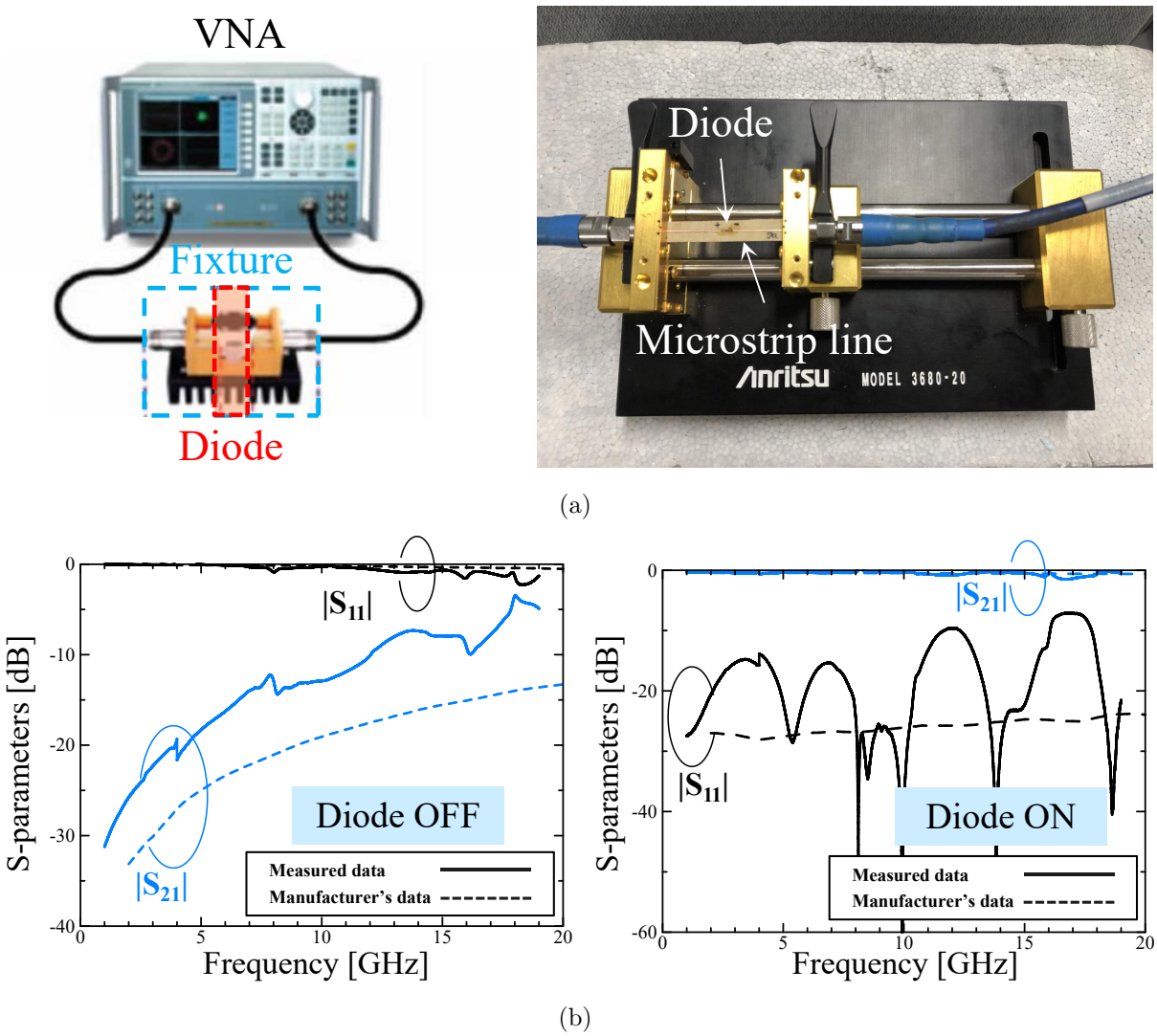

Figure 2.15: Measurement of diode's S-parameters. (a) Experimental Environment. (b) Measured results.

square wave signal generated by the function generator is set to 1 μs, corresponding to a frequency of 1 MHz.

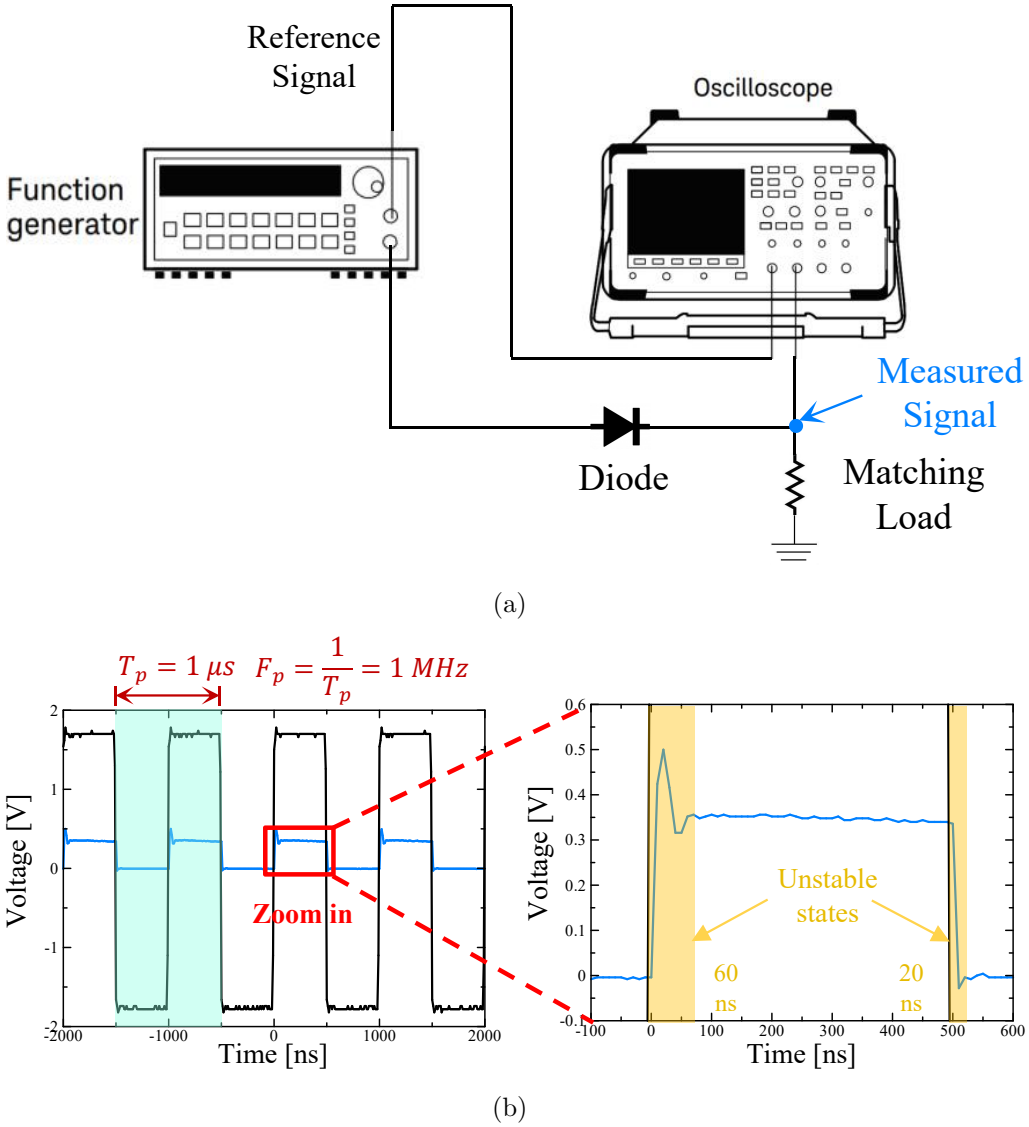

Figure 2.16: Measurement of diode's switching speed. (a) Experimental Environment. (b) Measured results.

As shown in Fig. 2.16(b), the experimental results reveal that the measured signal is essentially synchronized with the reference signal, indicating good switching speed.

However, it can also be observed from the zoomed results that there is some overshoot present after the rising and falling edges of the measured signal, indicating the presence of undesirable high-frequency harmonic components. Therefore, to ensure the effectiveness of time modulation, it is preferable for the diode switching frequency not to exceed 1 MHz. For the following experiments in Chapter 3 and Chapter 4, the modulation frequency of diode is set to 100 kHz.

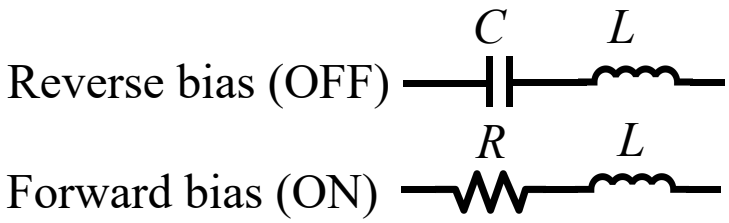

Figure 2.17: Lump circuit model for PIN diode modeling

Accurate modeling of diodes in simulation software is crucial for the successful design of TMRA. However, precise modeling of diodes is challenging as it requires considering the effects of various parasitic parameters and performing co-simulation with nearby electromagnetic structures [65–67]. Since the operating frequency is not very high (below 20 GHz), most RRA studies simplify the design by using lumped circuit models for diode modeling in simulation software [9, 14, 18]. As shown in the figure, when the diode is in the on state, its electrical characteristics are equivalent to a series circuit of capacitance and inductance. On the other hand, when the diode is in the off state, its electrical characteristics are equivalent to a series circuit of resistance and inductance.

Next, a microstrip line model with a diode inserted in the middle is considered to verify the effectiveness of the above lumped circuit model by comparing its simulation and measurement results. In the simulation, three modeling methods are used to simulate the diode and calculate the S-parameter results at both ends of the microstrip line. These three modeling methods are pre-measured diode S-parameters, lumped circuit model and S-parameters provided by the manufacturer, respectively. Based on continuous iterations to make the simulated results match the measured results, the values of the lumped components are finally set as $R = 4.8\ \Omega,\ C = 0.026\ pF,\ L = 30\ pH$. In the measurement, the S-parameters of the microstrip line at both ends are directly measured.

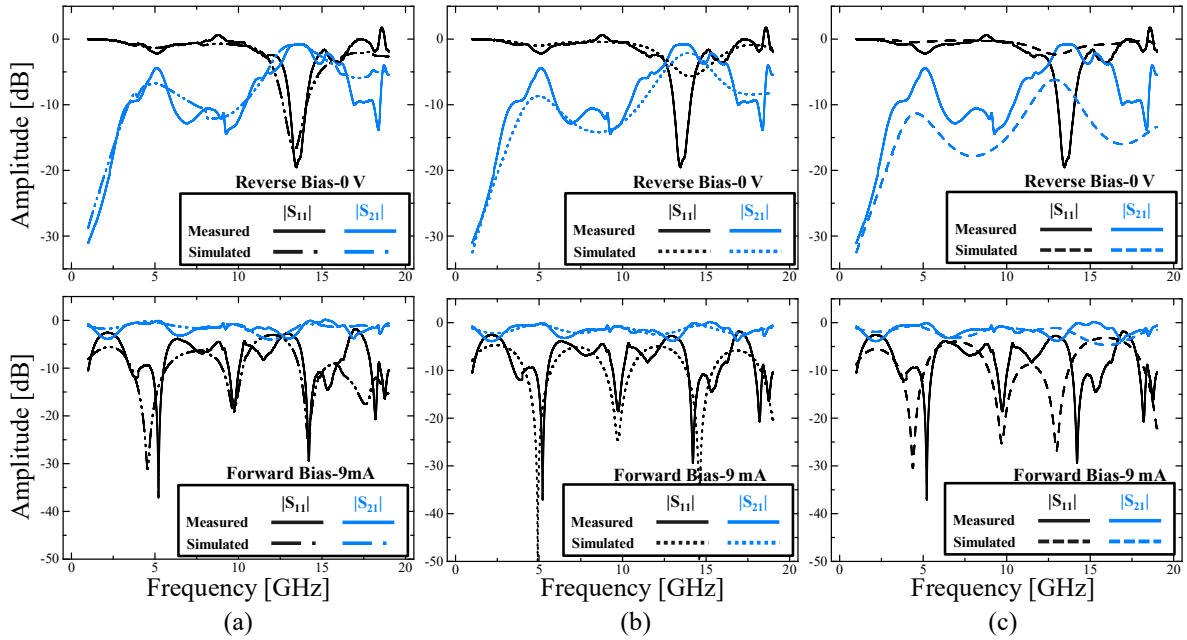

Figure 2.18: Measured and simulated results for different modeling methods. (a) Pre-measured S-parameters. (b) Lumped circuit. (c) Manufacture's S-parameters.

The simulation and measurement results of the three modeling methods are shown in Fig. 2.18.

It can be observed that the simulation results of the three modeling methods are in good agreement with the measurement results. The method using measured diode S-parameters shows the best agreement, as the measured data includes the capacitance effects on both sides of the diode from the solder pad structure and soldering. On the other hand, the simulation results using S-parameters provided by the manufacturer show the largest deviation from the measurement results, as the S-parameters provided by the manufacturer represent the diode's ideal performance and do not account for effects in the actual surrounding environment after assembly. In comparison, the lumped circuit model mentioned above not only exhibits good accuracy but also eliminates the need for upfront diode measurement, reducing the design complexity and workload. Considering these advantages, the subsequent work utilizes the lumped circuit model to simulate diodes in the simulation software.

2.7 Summary

In this chapter, firstly the theory of TMAA was introduced in detail, and the concept of time modulation was extended to TMRA. The focus was on discussing the implementation methods of TMRA and highlighting the differences compared to TMAA. Next, the analysis methods and definition of TMRA efficiency were presented. Furthermore, two typical applications of TMRA are introduced to show the flexible beam control abilities. In addition, the RWG method for fast measurement of element's reflection coefficient was illustrated and experimentally validated. Lastly, the performance of the used PIN diode was evaluated, and the accuracy of the diode modeling methods in simulation was verified.

Chapter 3

1-Bit TMRA with Real-Time Switchable Phase or Amplitude Control Ability

3.1 Introduction

In order to solve the problem that RRA can only control the phase, in this chapter we introduce the time modulation technique to the 1-bit RRA system to make it have the function of amplitude control, and name this new system as "1-bit TMRA". The proposed 1-bit TMRA has switchable phase or amplitude control capability, and can generate a scanning beam or a specially shaped beam to meet different communication needs according to the working scenario. A imaginary application scenario of proposed 1-bit TMRA is shown below.

3.2 Theoretical Analysis

3.2.1 Operating Principle

As emphasized in Chapter 2, the core of designing TMRA is to independently control the reflection coefficients of each element and to dynamically switch between these reflection

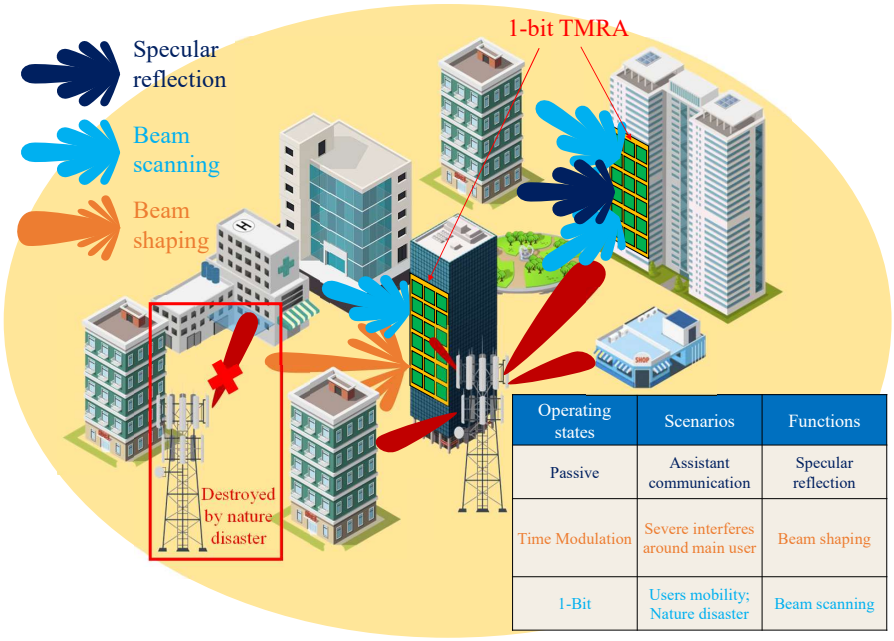

Figure 3.1: Imaginary application scenario of proposed 1-bit TMRA.

coefficients in real time according to the pre-designed time sequence. Previous studied of TMRA used strong/weak reflection states of RRA to realize high/low logic states of AMTS. Moreover, they have only amplitude control ability at carrier frequency. These characteristic makes them inefficient and impractical in the actual applications.

Due to the low efficiency observed in previous works, where strong/weak reflection states were used to implement TMRA, we considered the possibility of using two strong reflection states to achieve TMRA. Interestingly, as aforementioned, the 1-bit RRA has two strong reflection state with the same amplitudes and opposite phases. Therefore, it is natural to use these two strong reflection states to correspond the two logic states of time sequence. We named this concept that uses a 1-bit RRA to realize TMRA as "1-bit TMRA". Since the two logical states have same amplitudes but opposite phases, this kind of time sequence is called phase modulation time sequence (PMTS). The corresponding relationship between 1-bit TMRA and PMTS is shown in Fig. 3.2.

The Fourier coefficients of PMTS can be mathematically expressed as follows:

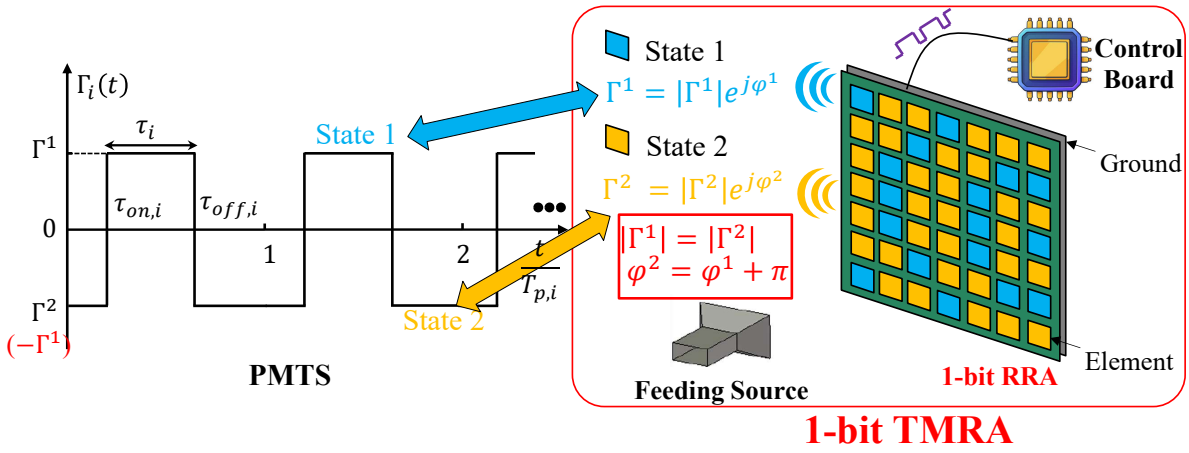

Figure 3.2: Concept of 1-bit TMRA.

$$a_{i,h}(t) = \frac{1}{T_{p,i}} \int_0^{T_{p,i}} \Gamma_i(t) e^{-j2\pi h F_{p,i} t} = \begin{cases} 2\tau_i \operatorname{sinc}(\pi h \tau_i) e^{-j\pi h(\tau_{off,i}+\tau_{on,i})}, & h \neq 0 \\ 2\tau_i - 1, & h = 0 \end{cases} \tag{3.1}$$

3.2.2 Errors Analyses of 1-bit TMRA Realization

As mentioned, at the core of the proposed 1-bit TMRA concept is the similarity between the two reflected states and the two logic states of the time function. As much, it is necessary to analyze the influence on the time modulation effect when the reflected states deviate from their theoretical states. Assuming the two reflection states of the 1-bit RRA are Γ^1 and Γ^2, respectively. They can be written as

$$\Gamma^1 = |\Gamma^1| e^{j\varphi^1}, \ \Gamma^2 = |\Gamma^2| e^{j\varphi^2} \tag{3.2}$$

where $|\Gamma|$ and φ are reflection amplitude and phase. Theoretically, the relationships of above two reflection states in 1-bit RRA should be as follows:

$$\begin{aligned} |\Gamma^2| &= |\Gamma^1| \\ \varphi^2 - \varphi^1 &= 180^\circ \end{aligned} \tag{3.3}$$

However, the corresponding relationships should be revised as follows to reflect the discrepancies expected in actual applications:

$$\begin{aligned} |\Gamma^2| &= |\Gamma^1| e^{-\frac{\Delta|\Gamma|}{20}} \\ \varphi^2 - \varphi^1 &= 180^\circ + \Delta\varphi \end{aligned} \tag{3.4}$$

where $\Delta|\Gamma|$ and $\Delta\varphi$ are amplitude error (dB) and phase error (degree), respectively.

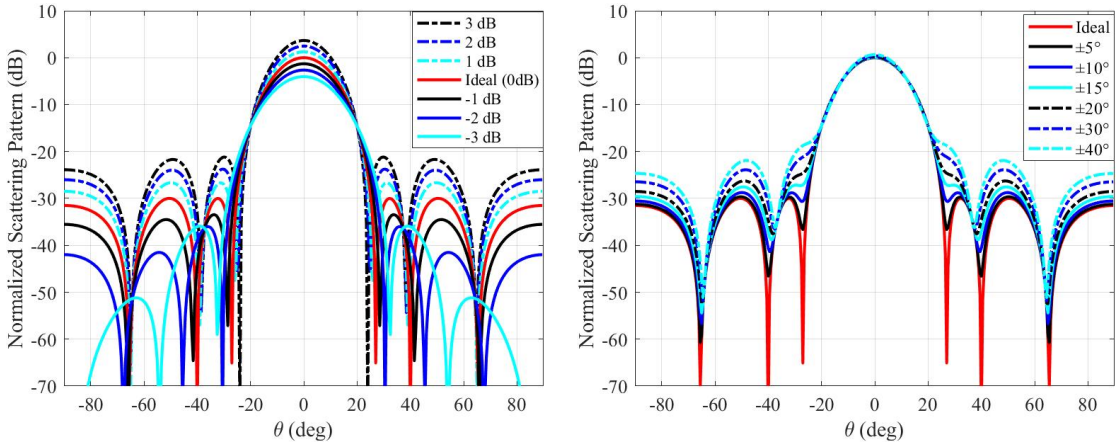

(a) (b)

Figure 3.3: Influence of errors of the amplitude and phase on TM. (a) Amplitude error. (b) Phase error.

The target of time modulation is to shape the reflected beam with equal SLLs of -30 dB. For simplicity, the vertical incidence is considered. The calculated results, all normalized to the ideal result, are plotted in Fig. 3.3. It can be observed from Fig. 3.3(a) that when $\Delta|\Gamma|$ is larger than 0, as $\Delta|\Gamma|$ increases, both the main beam and side-lobes increase simultaneously, and the overall SLLs increase as well. However, when $\Delta|\Gamma|$ is less than 0, as $\Delta|\Gamma|$ decreases, the SLLs are no longer equal even though the max SLL decreases, and the difference increases as $\Delta|\Gamma|$ decreases. It can be found that when $\Delta|\Gamma|$=-3 dB, the shape of the scattering pattern and the SLLs do not meet the design requirements at all. These results suggest that in the 1-bit TMRA design, -3 dB$< \Delta|\Gamma| \leq$0 dB should be satisfied to ensure the expected results are obtained.

On the other hand, it can be seen from Fig. 3.3(v) that the SLLs overall as $\Delta\varphi$ increases, and the first side-lobe gradually deteriorates and overlaps with the main beam when $\Delta\varphi$ is greater than 20°. For this reason, the 1-bit TMRA should be designed and implemented in such a way that the phase difference between the two reflective states is kept within the operating band of $180° \pm 20°$. It should be point out that the error analyses are based on the realization of equal SLLs of -30 dB. While the specific threshold value may differ in other time modulation applications, the analysis method described here is universal.

3.3 Design of 1-bit TMRA

3.3.1 1-bit TMRA element

The configuration of the proposed 1-bit TMRA element is shown in Fig. 3.4(a) and (b). The tunable resonator approach [68] is adopted to control the reflection. The polarization of the electric field is along the x-axis. The microstrip patch as a scatterer is printed on the top side of the element and connected to one end of the phase delay line printed on the bottom side through the metallization vias. A PIN diode is placed in the middle of the phase delay line, and the resonant property of the element is changed by biasing the circuit to turn the diode ON or OFF the diode, thus obtaining a 180° phase difference. The bias point is positioned at the zero-electric-field point at the center of the microstrip patch. Moreover, an open-ended radial stub and a quarter-wavelength microstrip line are designed to choke the RF signal. These approaches ensure good isolation of dc and RF performance and reduce the additional loss resulting from the bias network. In this design, the phase delay line, bias circuit, PIN diode, and the associated solders are arranged such that they are placed on the bottom side below the ground to avoid undesired scattering and the deterioration of the radiation performance of the 1-bit TMRA.

The initial structure of the element is inspired by the work reported by Yang et. al [9]. Since it offers low insertion loss and ultra-high switching speed, MACOM MA4AGFCP910 is chosen as the PIN diode, which acts as a switch in time modulation. As shown in Fig. 3.4(b) for ON or OFF state, the PIN diode is modeled as a series of lumped resistance

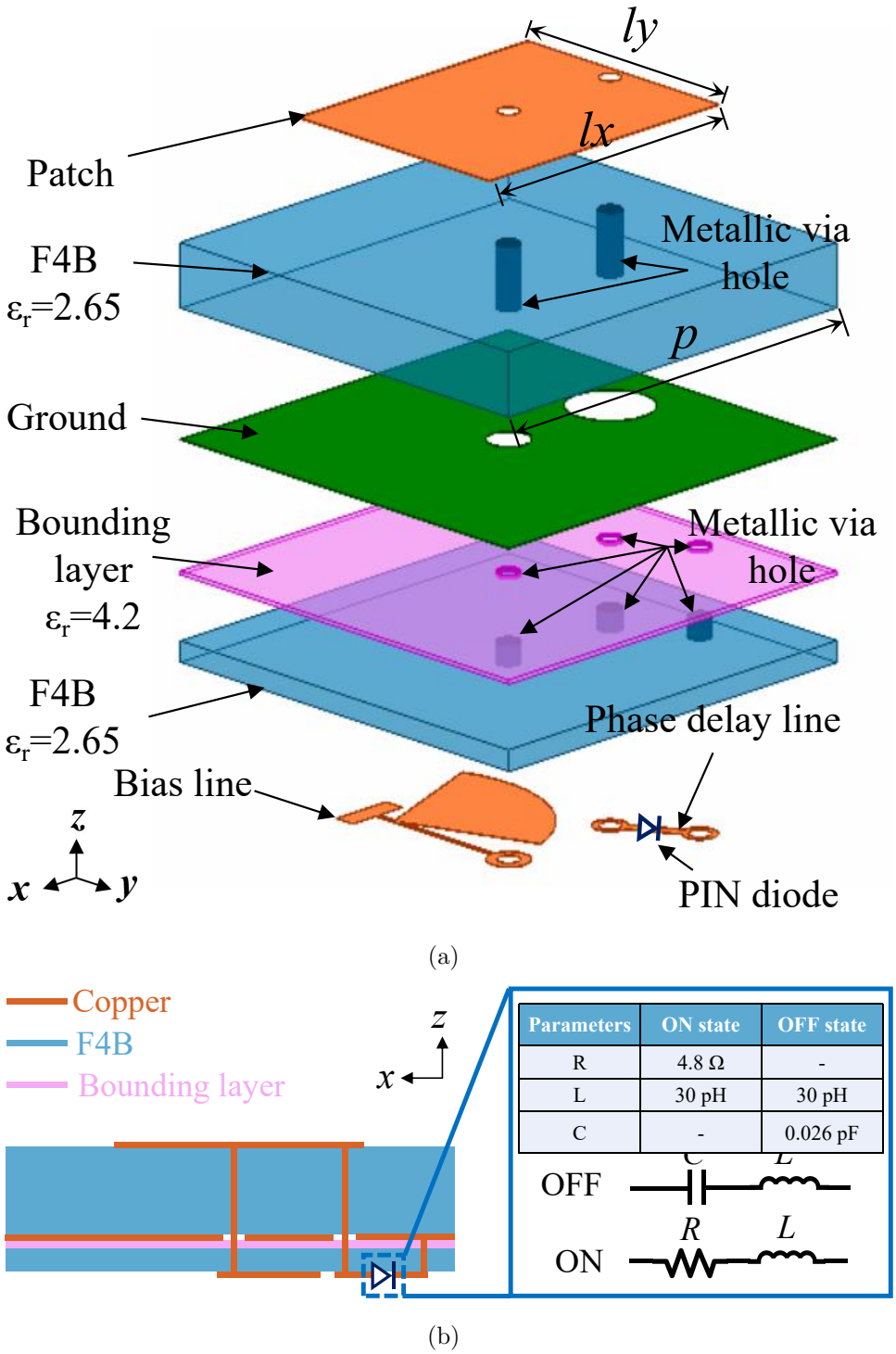

Figure 3.4: 1-bit RRA element. (a) Perspective view. (b) Side view and diode modeling.

(R) and inductance (L) or capacitance (C) and inductance (L), respectively. As in Fig. 3.5(a), parametric studies of some key parameters is conducted in order to achieve a 1-bit reflection state at 10 GHz, and the simulation results are shown in Fig. 3.5(b). As it can be found, the reflection states are sensitive to the element's period, patch size, length of phase delay line and diode's position. After parametric studies, the optimal result is obtained and shown in the Figure. To achieve a center operating frequency of 10 GHz, the periodicity of the element p is set at 10 mm ($\frac{1}{3}\lambda_0$, λ_0 is the free-space wavelength at 10 GHz) to avoid grating lobes. The main geometrical parameters of the 1-bit RRA element are as follows: lx=7 mm, ly=6 mm. The thicknesses of the three substrate layers from top to bottom are 1.5 mm, 0.1 mm, and 0.5 mm, respectively. Fig. 3.6 shows the simulated amplitudes and phase difference of the two reflection coefficients. under vertical incidence using Floquet ports and periodic boundaries in HFSS. At 10 GHz, the 180∘ phase difference is obtained when the PIN diode turns from one state to another. From 9.72 GHz-11.03 GHz, the phase difference between the two states is within 180 ∘ ±20∘, indicating good element-bandwidth performance. The element loss is less than -1 dB within the frequency band of interest, regardless of the PIN states.

For experimental validation, 1×2 1-bit TMRA elements are fabricated and measured using the waveguide simulator. The front and back views of the fabricated prototype element are shown in Fig. 3.7(a). Wires are soldered with the element to offer DC power for biasing the diodes. Fig. 3.7(b) shows the photo of the waveguide assembled with the fabricated prototype element. The model of the waveguide is WR90 with a cross-section of 22.86 mm × 10.16 mm , which is just enough to accommodate the prototype element. In the experiment, the prototype element is located at the surface of the waveguide, and the assembled waveguide is connected to a coaxial-to-WR90 transition structure. The other side of the transition structure is connected to the vector network analyzer (VNA) with the model of Anritsu MS46122B-020. Therefore, the reflection coefficient at the surface of the prototype element can be directly measured after using TRL calibration on the transition structure.

For comparison purposes, a WR-90 waveguide model is built, and the 1×2 1-bit RRA elements are placed in it for simulation. Fig. 3.8 shows the simulated and the measured reflection coefficients. It can be seen from Fig. 3.8(a) that the simulated and measure reflection phases are in good agreement. As shown in Fig. 3.8(b), despite the small

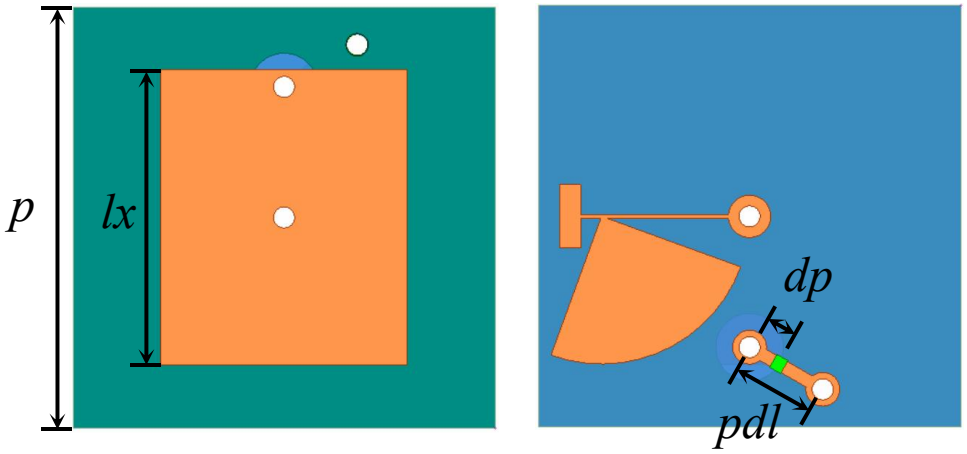

(a)

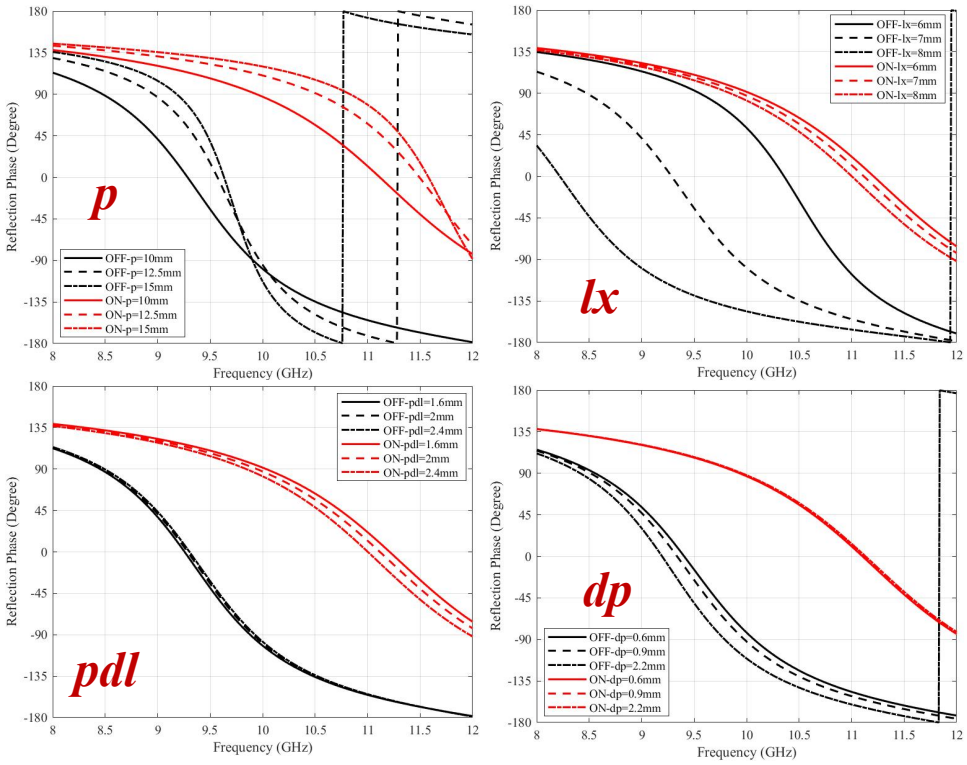

(b)

Figure 3.5: Parameter study of 1-bit RRA element. (a) Perspective view. (b) Side view and diode modeling.

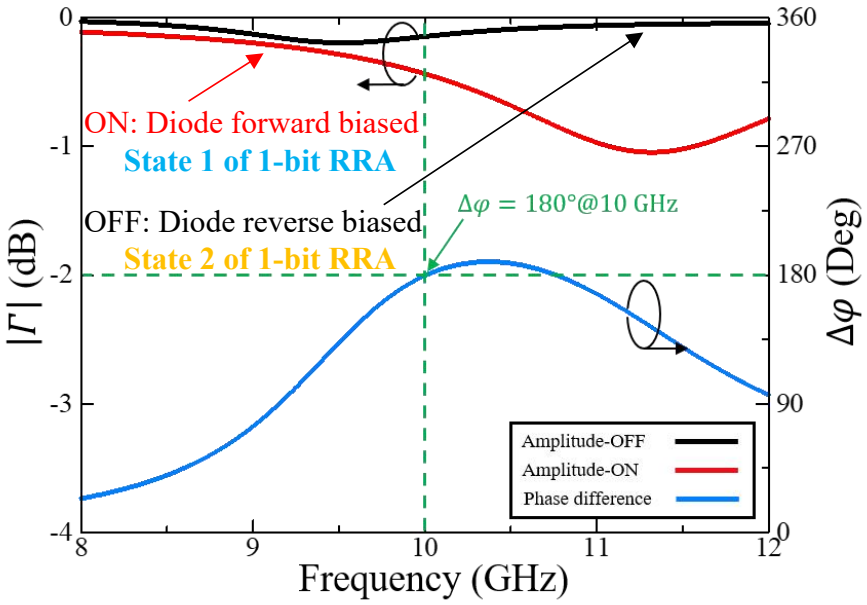

Figure 3.6: Simulated reflection amplitude and phase difference of the two states.

differences in the reflection amplitude of the OFF state, they are all above -1 dB near 10GHz. In addition, the resonance at the ON state is caused by the oblique incidence in the waveguide, which is not the characteristic of the element itself. These slight differences can be attributed to the fabrication tolerance and assembly misalignment among the waveguide, the transition structure, and the fabricated sample. Therefore, 1-bit phase reconfigurability with low loss is achieved, making it suitable for large 1-bit TMRA designs.

3.3.2 1-bit 10×10 TMRA Prototype

Based on the proposed element structure, we designed and fabricated a 1-bit RRA prototype using printed circuit board (PCB) technology, as shown in Fig. 9. The 1-bit RRA has an aperture of 100 mm $\times$ 100 mm ($3.33\lambda_0 \times 3.33\lambda_0$). Each element is soldered with a PIN diode and connected to a specific bias line to achieve independent control of 100 elements. The 1-bit RRA and the control board are soldered with sockets, which are connected to each other by flat cables. Since each socket controls five elements indepen-

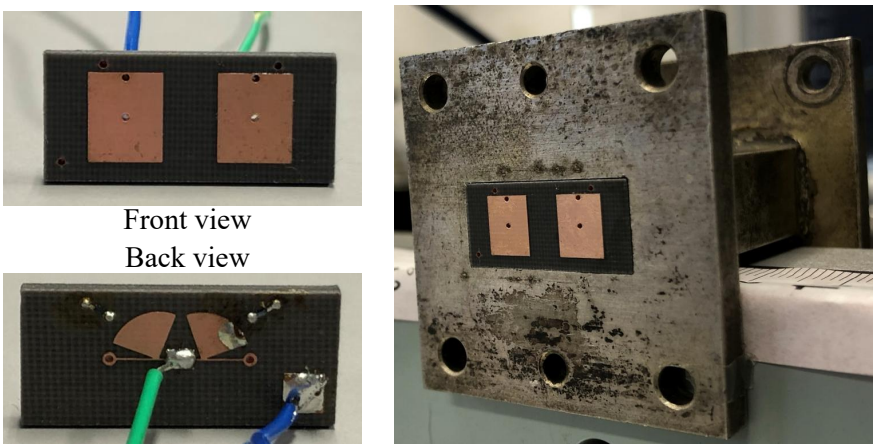

(a) (b)

Figure 3.7: Photographs of fabricated element prototype and assembly with a waveguide. (a) 1×2 1-bit TMRA element prototype. (b) Assembly with a waveguide.

dently, so there are 20 sockets soldered to the 1-bit RRA, symmetrically arranged on both sides of the 1-bit RRA. Through the control board, 100 elements can be controlled in real-time to realize 1-bit and time modulation characteristics.

3.3.3 Feed Source Selection and System Design

The near-field feed method is widely used in RA systems to realize higher aperture efficiency [9]. Although the corrugated horn antenna, which provides a symmetric radiation pattern and excellent antenna efficiency, is widely used in RA design. Its bulk would cause severe blockage for such a small aperture of the fabricated 1-bit TMRA prototype. Instead, in this work, a printed antipodal fermi antenna (APFA) with tapered slots [69] is used as the feed source with the advantages of small volume, low profile, and lightweight, where the schematic and the parameters are shown in Fig. 3.10. The APFA is linear polarization with the polarized direction along the short side. Two opposite slots are etched on both sides of the dielectric substrate, with the slot curve satisfying the Fermi-Dirac function. The operating principle and detailed characteristics of the APFA can be found in [69] and is omitted in this paper. Therefore, only the radiation characteristics of interest are shown here and plotted in Fig. 3.11. All the results are obtained by the

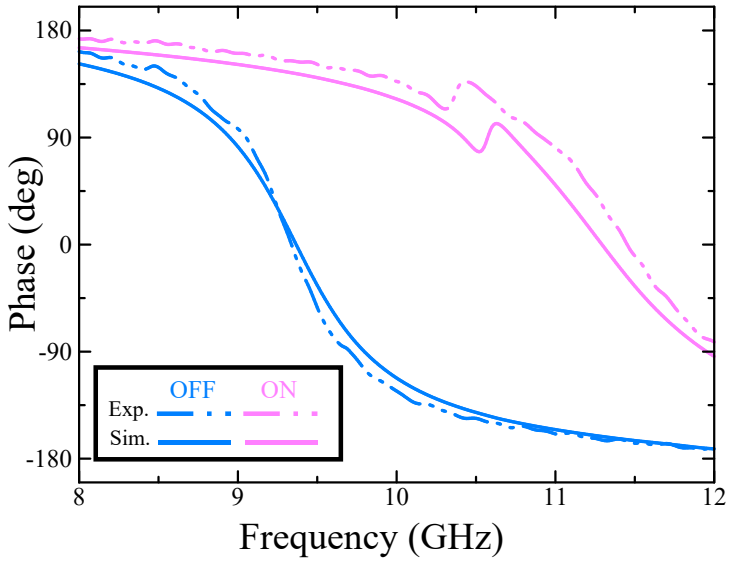

(a)

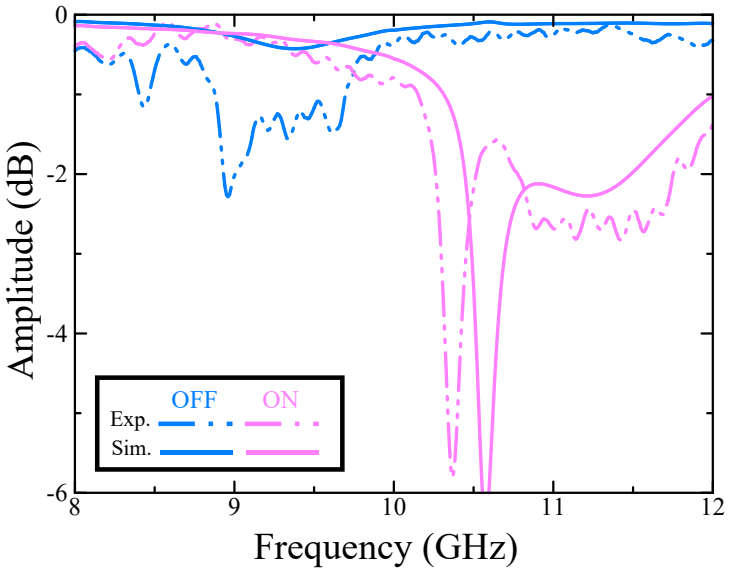

(b)

Figure 3.8: Comparison between simulated and measured reflection coefficients. (a) Reflection phases. (b) Reflection amplitudes.

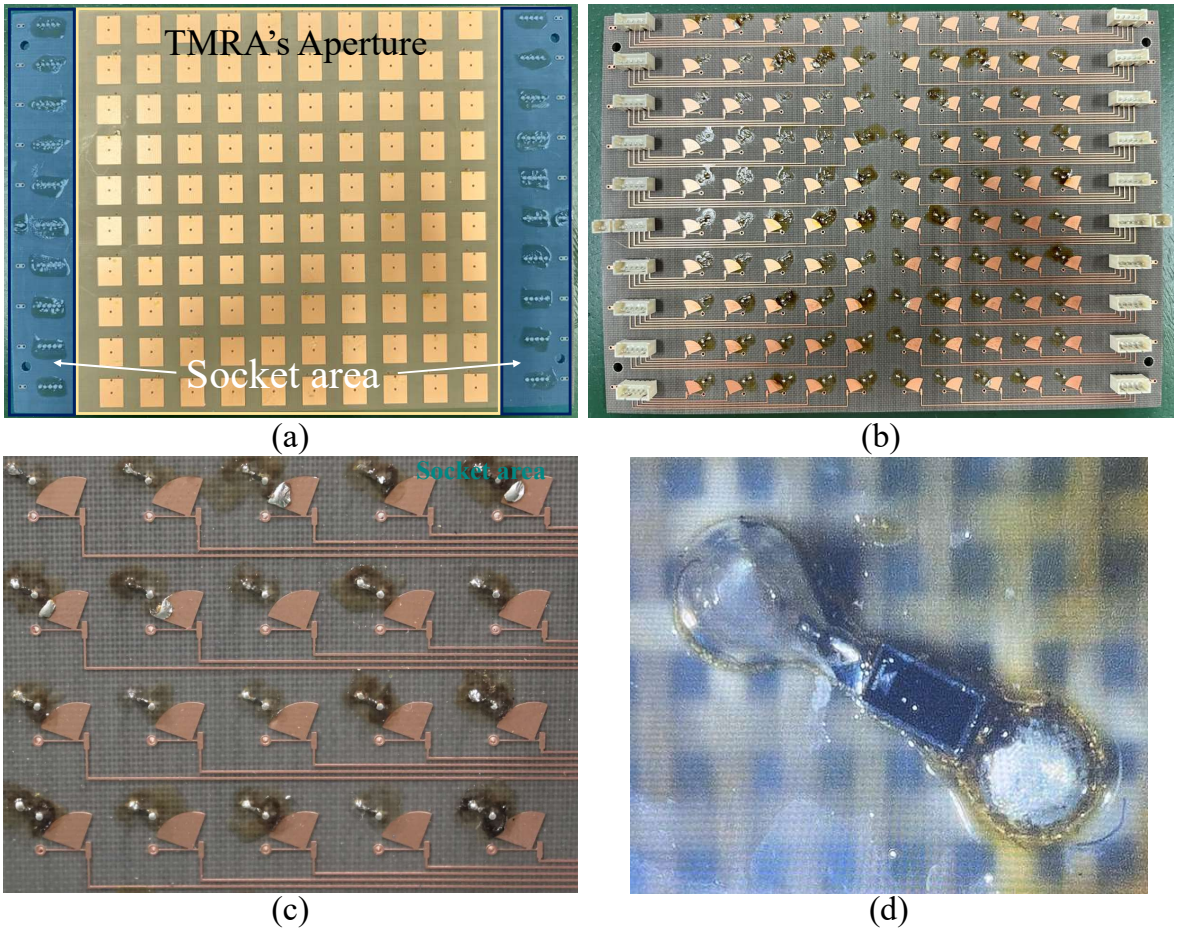

Figure 3.9: 1-bit 10×10 TMRA prototype. (a) Top view. (b) Bottom view.(c) Detail of the bias lines. (d) Detail of PIN diode soldering

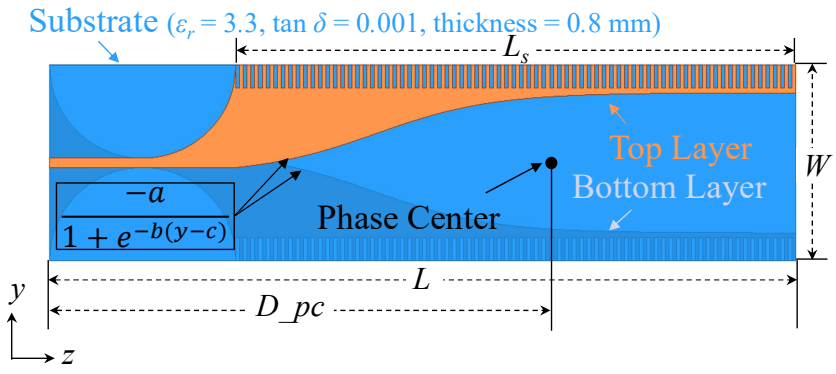

Parameters	Value
a	16
b	0.83
c	60
L_s	120 mm
L	160 mm
W	42 mm

Figure 3.10: APFA schematic view.

full-wave simulation via High Frequency Structure Simulator (HFSS). The realized gain and radiation efficiency are shown in Fig. 3.11(a), indicating the high gain and high efficiency of the APFA. The downward trend with increasing frequency of the efficiency is mainly attributed to larger metal and dielectric losses in the high-frequency range. Fig. 3.11(b) shows the phase center response and demonstrates greater than 65 mm variation in X-band. Besides, the normalized Co-Pol radiation patterns in E-/H-plane are plotted in Fig. 3.11(c) and (d), indicating the asymmetric radiation characteristic with a wider H-plane and narrower E-plane.

Fig. 3.12 shows the system design and configuration. To reduce the feed blockage, the APFA is located offset from the normal of RRA aperture with an oblique angle of -20 degrees in the yz plane, as shown in Fig. 3.12(a). F is the distance between the phase center of APFA and the center of RRA's aperture whose side length is D. Moreover, for realizing the optimal system performance, which is aperture efficiency, the feed location (described by F/D) must be carefully chosen to balance the spillover efficiency and the illumination efficiency [51]. The $\cos^q(\theta)$ feed power pattern method is used to calculate the efficiencies mentioned above, and the results are shown in Fig. 3.12(b), indicating the theoretical maximum aperture efficiency of 76.7 % with the F/D equal 1. Based on the optimal configuration, the final feed position is $P(0, 34, 96)$ mm and the corresponding taper distribution on the 1-bit RRA aperture is shown in Fig. 3.12(c). It should be noted that the edge taper at some positions is larger than the common threshold of -10

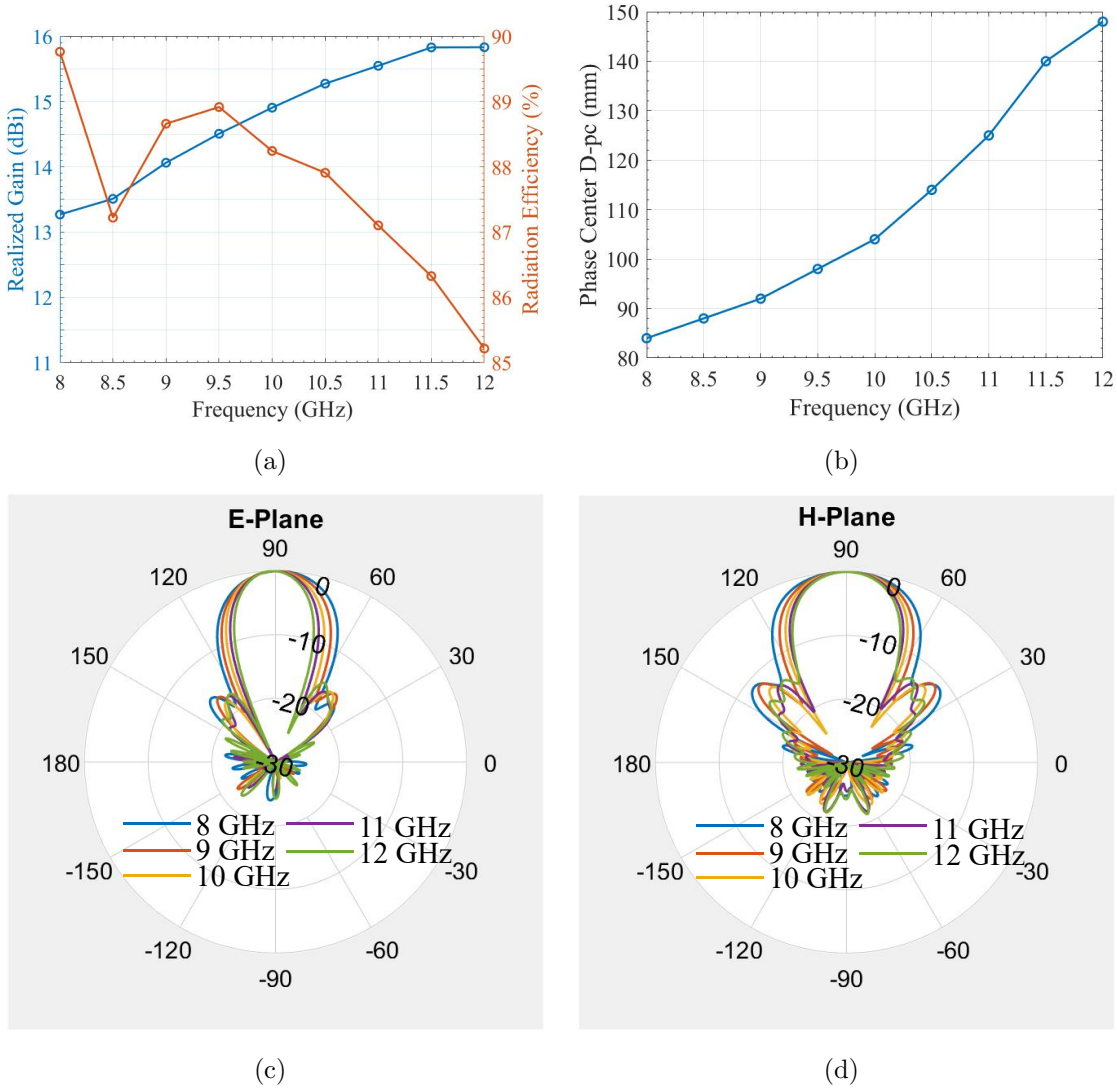

Figure 3.11: APFA performance in terms of (a) realized gain and radiation efficiency and (b) phase center response. (c) E-plane normalized radiation pattern. (d) H-plane normalized radiation pattern.

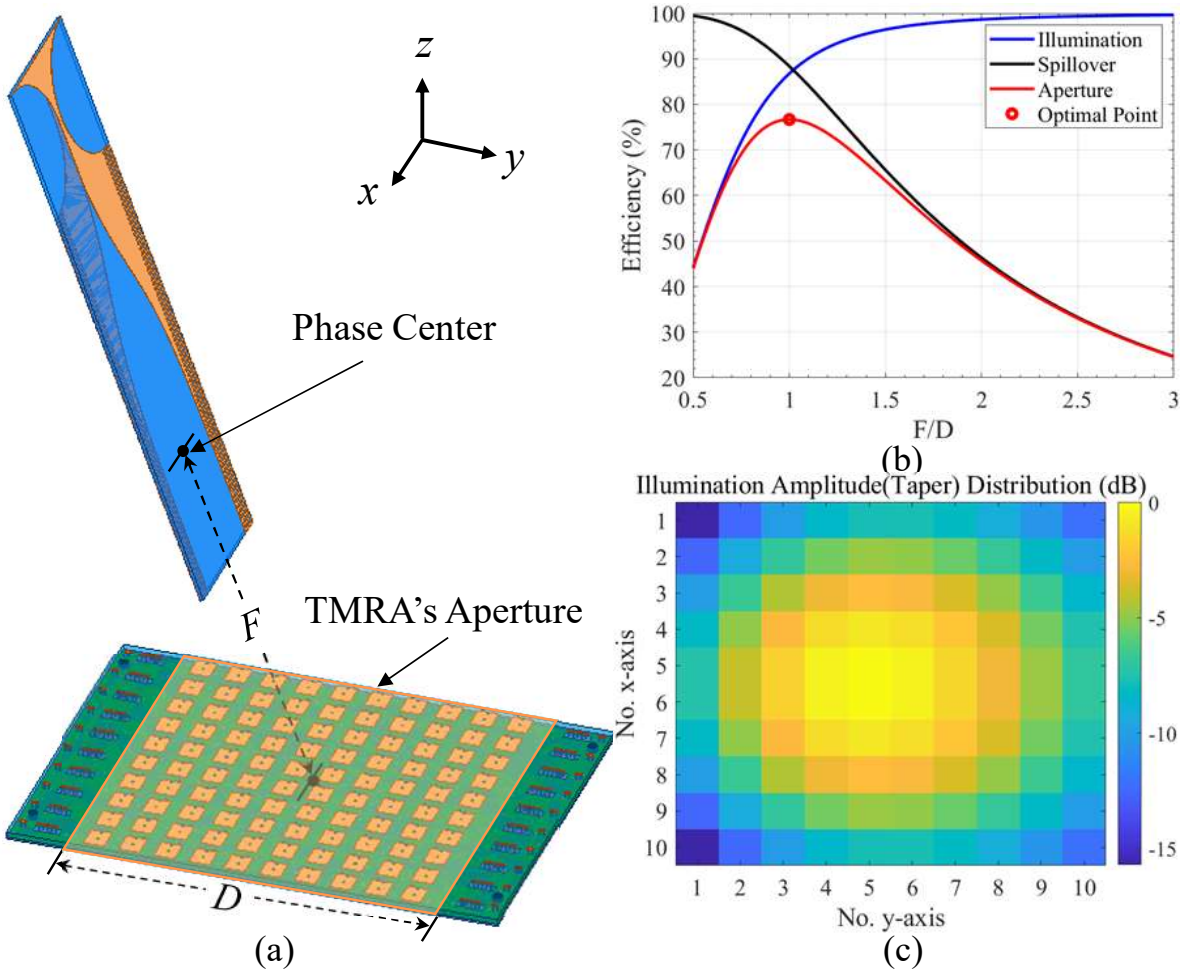

Figure 3.12: System configuration. (a) Schematic view of feed. (b) Effect of F/D on efficiencies of RA antenna system. (c) Normalized taper distribution on 1-bit TMRA aperture when the aperture efficiency is optimal.

dB in RA design [17], which may increase the SLLs of the radiation pattern, especially for large-angle beam scanning. However, the effect of feed blockage on radiation performance would be more severe when decreasing the F/D to obtain a lower edge taper, due to the small size of the fabricated prototype.

3.3.4 Design of Control Board

As shown in Fig. 3.13 and Fig. 3.14, the control boards were designed and fabricated for beam-scanning and time modulation, respectively. Fig. 3.13 shows the control board that implements the 1-bit RRA state (to realize beam-scanning). The control circuit design is shown in Fig. 3.13(a). It can be clearly seen that each bias line is connected in series with a light-emitting diode (LED) indicating the PIN diode's state and a slide switch controlling the PIN diode's state. The LED matrix also directly displays the 1-bit phase distribution of the 1-bit RRA, making the debugging and testing procedure easier and more straightforward. Fig. 3.13(b) shows a picture of all lighted LEDs on the control board.

The control board that implements the time modulation state is shown in Fig. 3.14. Constrained by the quantity of the function generator, each column consisting of 10 elements of the 1-bit RRA prototype is set up as a group for control. Moreover, as shown in Fig. 3.14(a), the desired reflection distribution for Chebyshev pattern is symmetric about the center of the RRA. This allows 10 groups (100 elements) to be controlled using 5-channel time signals (20 elements per channel). The time signal is a square wave signal generated by a function generator, whose high level corresponds to the ON state of PIN diode and "1" state of the time function, and vice versa. The modulation frequency $F_{p,i}$ and switch-on duration τ_i of the time function are controlled by setting the frequency and duty cycle of the square wave in function generator, respectively. It can be clearly seen from Eq. (3.1) that the time-modulated equivalent amplitude weighting of the center frequency is independent of the normalized turn on time $\tau_{on,i}$, thus the time signal $\tau_{on,i}$ is set the same for each channel and has $\tau_{on,i} = 0$. Note that the control board of time modulation controls each column of elements, which requires the same amplitude of elements within a column in order to guarantee an effective control effect. In the near-field feed, the amplitude of the elements composing each column varies. Therefore, in

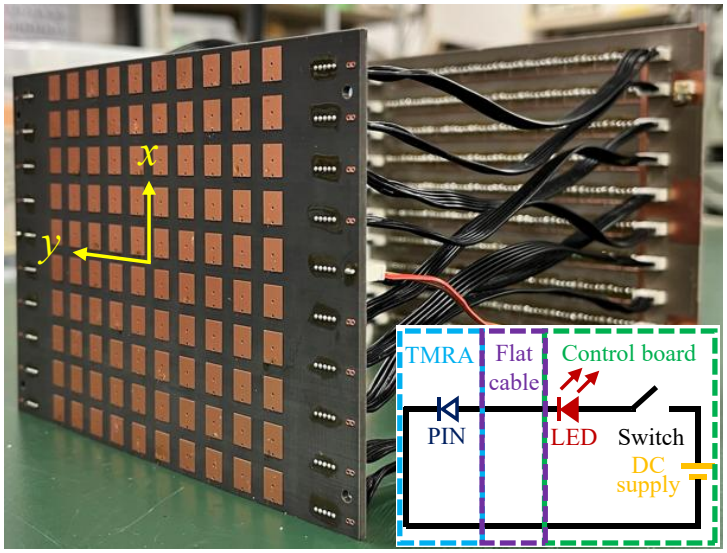

(a)

(b)

Figure 3.13: Control board of 1-bit RRA state. (a) Control circuit design.(b) Control board with LEDs all ON.

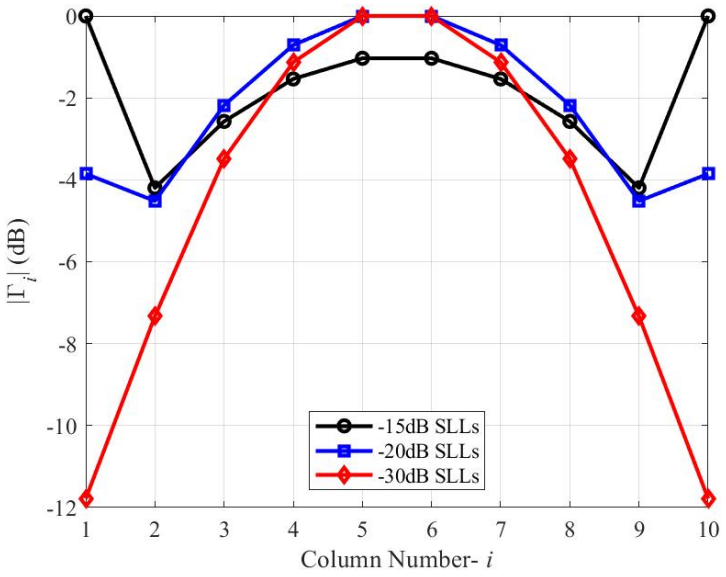

(a)

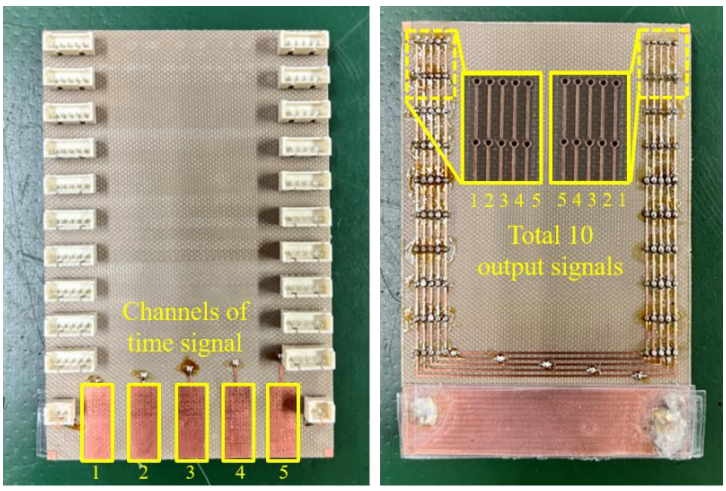

(b)

Figure 3.14: Control board of TM state. (a) Desired $|\Gamma|$ distribution. (b) Photo of control board

the experiment to validate the time modulation characteristic, the feed should be placed in the far-field region of the TMRA.

It should be pointed out that whether the control boards are designed separately or different feed distances are used for different validation experiments, they are only measures limited by the existing experimental environment and not drawbacks of the proposed concept of 1-bit TMRA.

3.4 Experiment Validation and Results

First, the reflection characteristic of 1-bit TMRA prototype is verified through the measurement of reflection coefficients.Then, the phase control ability of 1-bit TMRA prototype is verified by realizing beam-steering through 1-bit phase quantization. The amplitude control ability of 1-bit TMRA prototype is verified by realizing beam-shaping through time modulation.

3.4.1 Validation of Reflection Characteristic

The first experiment is designed to verify the reflection characteristics of the designed TMRA. The results of this experiment will form the basis of the subsequent experiments, as shown in Fig. 3.15(a). This experiment uses the space-wave method and is performed in the microwave anechoic chamber. A linear polarized standard gain horn antenna of model Flann-16240 is used as the transmitting (Tx) antenna with a gain of 20 dBi. The Tx antenna is connected to the vector network analyzer (VNA) through a coaxial line as the feed source for the experiment. The model of the VNA is Anritsu MS46122B-020, which covers a frequency band from 1 MHz to 20 GHz. The Tx antenna is placed facing the RRA, and the aperture centers of the Tx antenna and RRA are coaxial and 1.822 m apart. Both Tx and 1-bit RRA are vertically polarized. To reduce the influences from the socket area's ground of the 1-bit RRA prototype and experimental environment (e.g., control board and supporting structure), the surroundings of RRA's aperture are shielded with absorbing material. Note that the time domain gating function of the VNA is used in the measurement to eliminate undesired scattering from the experimental environment.

The reflection characteristics of the 1-bit RRA are obtained by measuring the reflec-

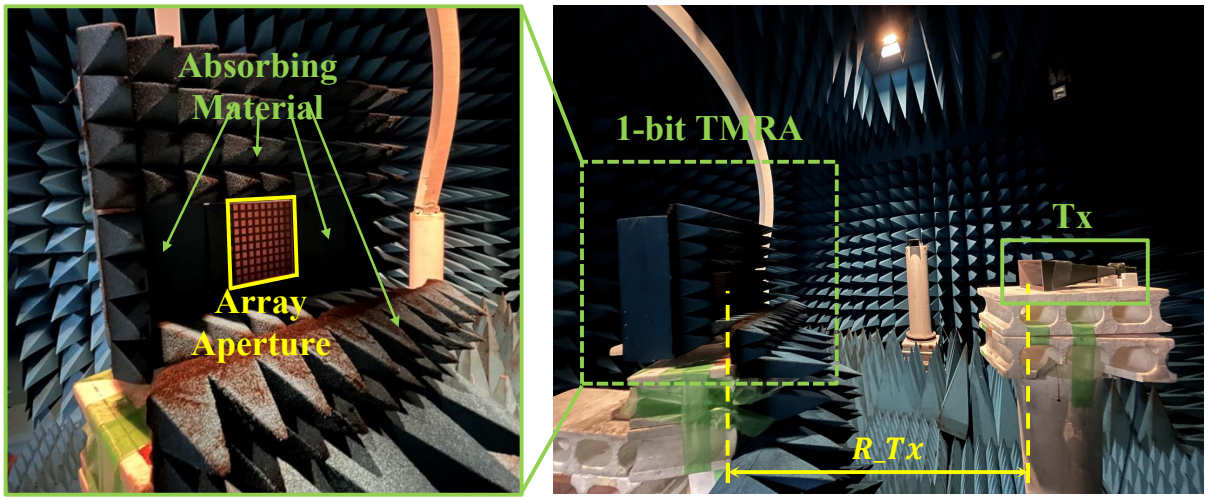

(a)

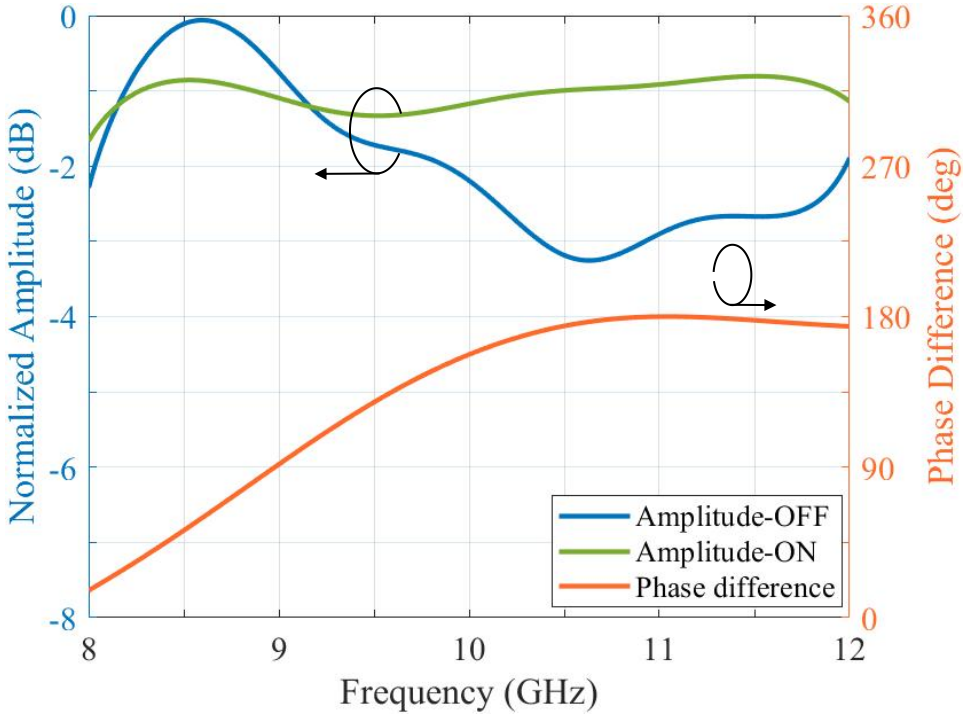

(b)

Figure 3.15: Measurement of reflection characteristic of 1-bit 10×10 TMRA prototype. (a) Experimental environment. (b) Experimental results.

tion coefficients of RRA with all diodes set to ON and all diodes set to OFF, respectively. In addition, the reflected amplitudes for the two states are both normalized to the reflected amplitude of a metal sheet of the same size as the 1-bit RRA prototype. The measured results are shown in Fig. 3.15(b). It can be found that the reflected amplitude of the ON state is very stable with a magnitude of -1 dB, while the reflected amplitude of the OFF state has a larger vibration. However, the maximum difference between the reflection amplitudes of the two states is less than 2.2 dB, indicating that the 1-bit RRA prototype can realize two relatively stable reflection states. From 10.08 GHz to 12 GHz, the phase difference stays within $180° \pm 20°$. Specifically, it can be observed from 10.5 GHz to 11.5 GHz that the phase difference is close to 180°, and its curve varies very smoothly. Note that the frequency point of a 180° phase difference between the two states is 11.1 GHz, which is the experimentally verified 1-bit frequency point of the proposed RRA and operating frequency in the following experiments. Moreover, the amplitude difference is 1.9 dB for the two states at 11.1 GHz.

It should be pointed out that the discrepancies in reflection characteristics of the element are mainly due to the reflection from the ground of the socket area of the fabricated RRA prototype (shown in Fig. 3.3.2(a) and (b)). The reflection severely interferes with the original reflected fields produced by the RRA's aperture only, thus affects the reflection characteristics of the 1-bit RRA prototype. Note that this is a design fault of the control circuit of the fabricated prototype, not a drawback of the proposed 1-bit TMRA concept, and this problem can be completely solved by removing the ground beneath the socket area. Moreover, other common reasons such as estimated error of the equivalent capacitance in the PIN diode modeling [18], inconsistency in the hand soldering of the diodes and array fabrication error would also introduce experimental errors.

3.4.2 Validation of Phase Control Ability

As shown in Fig. 3.16, the measurement system consists of the RRA system, the rotary table, and the receiving antenna (Rx). The RRA system includes the RRA, the control board and the feed antenna (Tx). The control board is placed at the back of the RRA and connected to the RRA using the flat cables (not marked in Fig. 3.16). The Tx is vertically polarized and its location is described by the feed distance R_Tx and feed angle

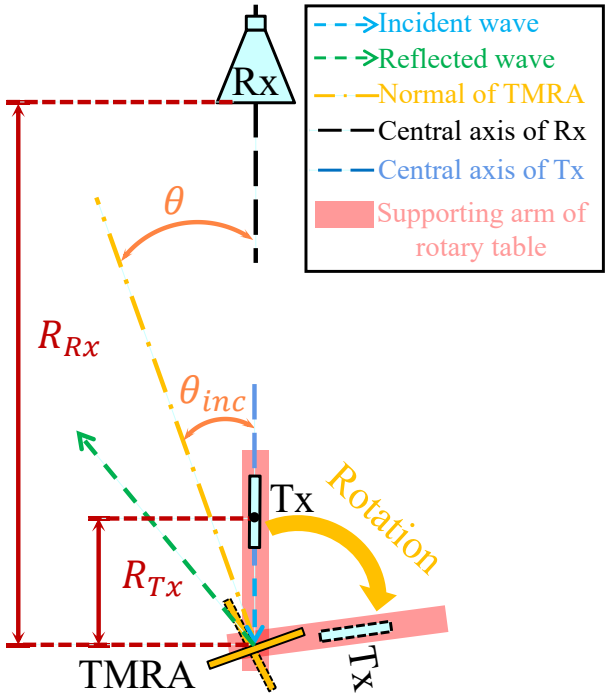

(a)

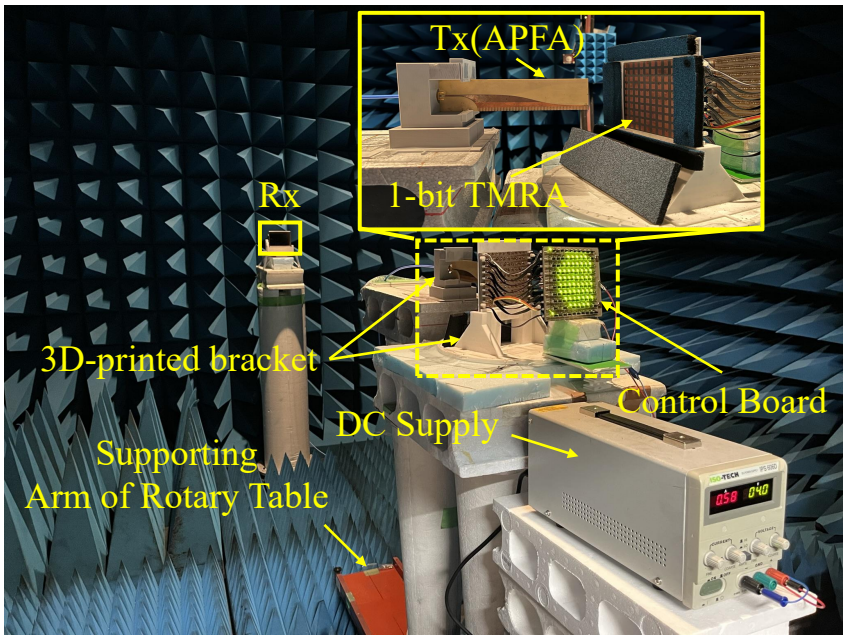

(b)

Figure 3.16: Experimental environment for validation of beam scanning characteristic. (a) Schema of the measurement system (top view). (b) Overall perspective photograph.

θ_{inc}, whose values are determined in the " Feed Source Selection and System Design " part of the last section. The RRA and Tx are placed at the center and the supporting arm of the rotary table, respectively. The RRA is fixed by 3D-pritend brackets. The surrounding of the RRA's aperture is covered by the absorbing material to decrease the interference of the ground of the socket area. The relative position of the RRA and Tx is kept constant in the rotation of the rotary table. The Rx is the same horn antenna used in the previous experiment and is fixed in the far-field region of the RRA with a distance of R_{Rx}, and the angle between its central axis and the normal of the RRA aperture is defined as the scanning angle θ. Therefore, by rotating the rotary table in the horizontal plane, the radiation pattern of the RRA can be measured. A photograph of the experimental environment is provided in Fig. 3.16(b). The relevant parameters are as follows: $R_{Tx} = 100$ mm, $\theta_{inc} = -20°$ and $R_{Rx} = 2400$ mm. Note that the measured gain of Tx (APFA) at 11.1GHz is 14.4 dBi.

The phase control ability is verified by realizing beam scanning using a reconfigurable 1-bit phase distribution. Fig. 3.17(a) shows the 1-bit phase distribution for different scan angles. The yellow area corresponds to the state "1", which corresponds to the diode ON state, and the blue area corresponds to the state "-1", which corresponds to the diode OFF state. The measured radiation patterns of co-polarization (Co-Pol) are plotted in Fig. 3.17(b). It is be observed that the reflected beam of the 1-bit RRA can be controlled to scan in the range of $10° - 50°$ with the above phase setting. Note that the slight distortions on the main beams of small scanning directions can be observed, which are mainly caused by the blockage of Tx and feed cable. The radiation performances in terms of gain and maximum SLL for scanned directions are summarized in Table 3.1. In addition, the beam error is $-3°$ when the scanning beam towards $50°$. As aforementioned, the incident angle is $-20°$, and therefore the maximum reflected beam occurs in the $20°$ direction. The measured gain at this direction is 15.6 dBi, corresponding to a maximum aperture efficiency of 21.1 % using the following definition:

$$\eta = \frac{G}{4\pi A/\lambda^2} \tag{3.5}$$

where G is the measured gain and A is the aperture area. Besides, it is observed that the gain variation does not exceed 1 dB within the scanning direction range, indicating the

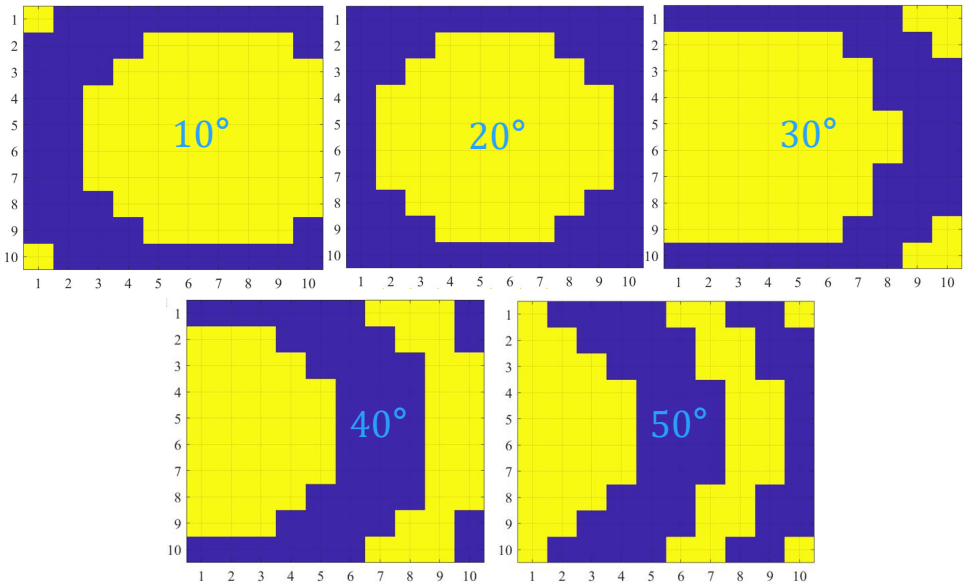

(a)

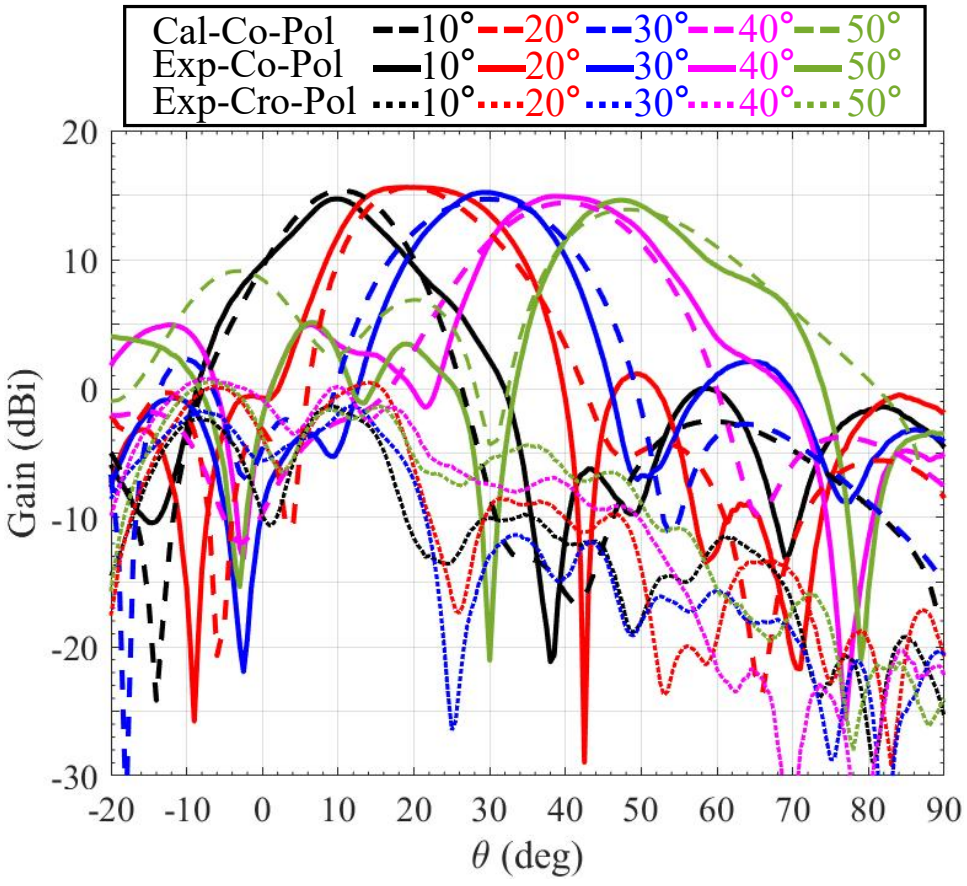

(b)

Figure 3.17: Experimental result of beam scanning. (a) 1-bit phase distribution for scanning directions. (b) Measured and theoretical radiation pattern.

Table 3.1: Measured Gain and Maximum SLL at Scanned Direction

Radiation Performance	10°	20°	30°	40°	50°
Gain (dBi)	14.7	15.6	15.2	14.9	14.6
Maximum SLL (dB)	-14.7	-14.3	-13.2	-9.7	-9.4

stable radiation performance of beam scanning. In terms of SLLs, good results with the maximum SLL below -13 dB can be observed for the beam scanning range of $10° - 30°$. It can also be found that the SLLs become worse for large-angle scanning. This is mainly due to the small aperture size of the fabricated prototype and the large edge taper it causes, which was detailly discussed earlier. Table 3.2 lists the loss budget for the main reflection direction (20°) at 11.1 GHz. It suggests that the 1-bit phase quantization error is the main reason of gain loss in this design. The theoretical radiation patterns of Co-Pol calculated by the MATLAB program are also plotted as references. Good agreement can be observed from measured and theoretical results, validating the correctness of the measurement. Note that the slight differences on gain variation for the calculation and measurement results are may be attributed to the simplified modelling of the ground of socket area in the program and experimental errors. In addition, the cross-polarization (Cro-Pol) is also measured and plotted in Fig. 3.17(b). The overall relatively high Cro-Pol is mainly caused by the offset feed system [51] and is constrained by the Cro-Pol level of the APFA itself. Even though, the results show good polarization purity for all scanning directions, corresponding to the Cro-Pol level (normalized to Co-Pol level) of -16.1, -22.3, -28, -22.1 and -21.2 dB, respectively.

It should be noted that the gain and SLLs are mainly limited by the large edge taper, which is caused by the small aperture size of the fabricated prototype. Therefore, the gain and SLLs can be improved by increasing the aperture size and configuring a more appropriate feed system. In addition, the specular reflection from the ground of the socket area also increases the SLLs for large-angle scanning. In terms of the aperture efficiency, although it can be slightly improved by increasing the aperture size, i.e., reducing the feed blockage in this work, it is difficult to further improve the aperture efficiency due to the 1-bit phase quantization loss and losses of diodes, which are inevitable in 1-bit RA design. In summary, the 1-bit characteristic of the proposed 1-bit TMRA is verified by

Table 3.2: Loss Budget for the Main Reflection Direction at 11.1 GHz

Factor	Loss (dB)
Spillover	0.54
Illumination	0.62
Feed antenna	0.61
1-bit phase quantization	2.56
Diode	0.72
Feed blockage, phase error, metal loss, dielectric loss, others	1.71
Total	6.76

the experiment.

3.4.3 Validation of Amplitude Control Ability

Fig. 3.18 shows the experimental environment and measurement system to verify the amplitude control ability. As aforementioned, Tx should be placed in the far-field region of the TMRA in this experiment. Constrained by the length of the rotary table supporting arm, Tx has finally placed 820 mm away from the center of the TMRA aperture, which almost satisfies the far-field condition. To increase the signal-to-noise ratio in measurement, the horn antenna is adopted as the Tx. The rest of the experimental setup is the same as the previous experiment. Note that the normalized scattering patterns are measured in this experiment to properly evaluate the scattering performance of the proposed 1-bit TMRA. Specifically, all measured results are normalized to the scattering pattern of a metal plate of the same size as the fabricated 1-bit TMRA prototype.

The experimental target is to realize the scattering pattern with -20 dB equal SLLs by means of the time modulation (TM). The modulation frequency is 100 kHz for all channels. Fig. 3.20(a) shows the required time sequence of each channel. The dark area corresponds to the state “1”, which corresponds to the diode ON state, and the light square corresponds to the state “-1”, which corresponds to the diode OFF state. The measured results are shown in Fig. 3.20(b). Note that the theoretical calculation result of adopting time modulation is also plotted as a reference. In addition, the results of the

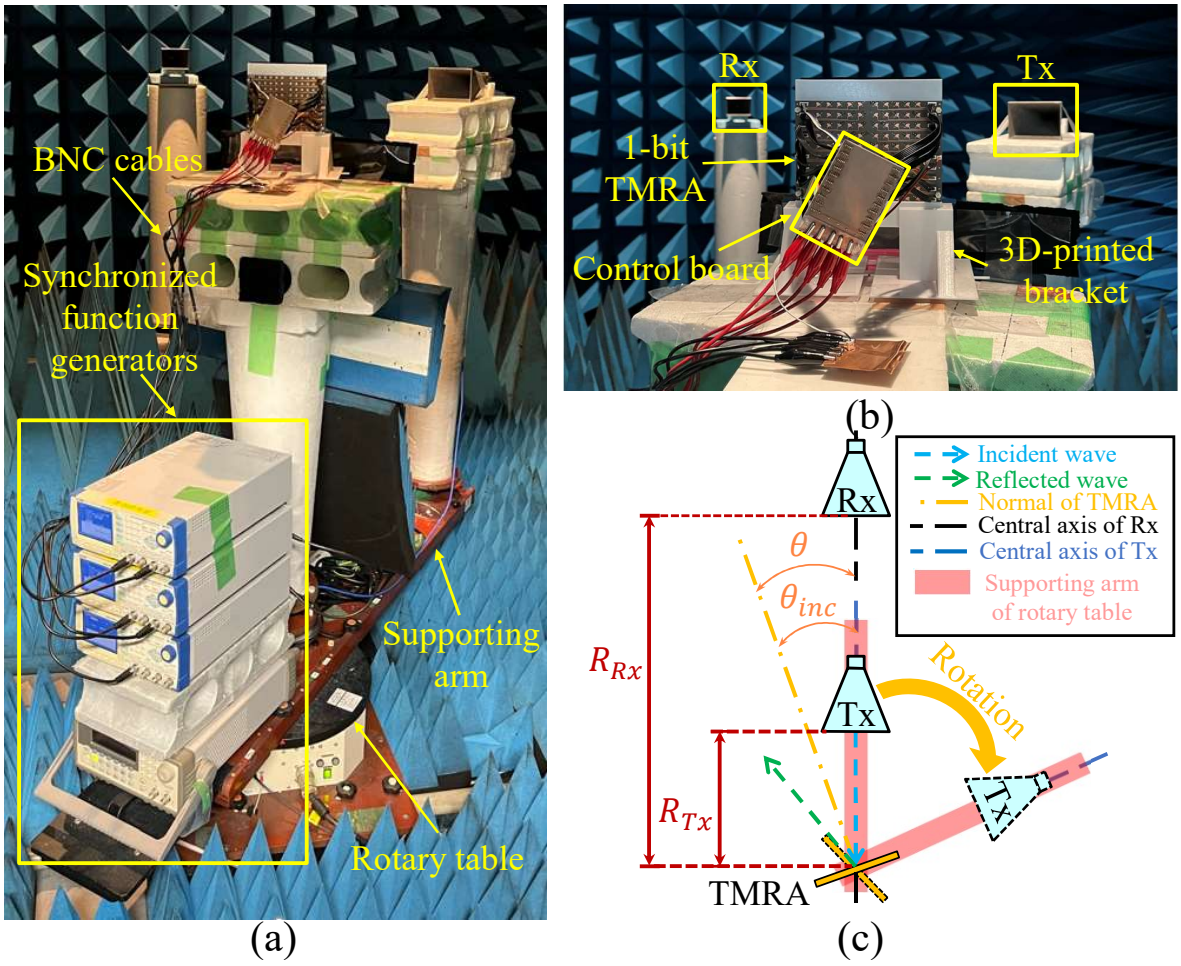

Figure 3.18: Experimental environment for validation of TM characteristics. (a) Overall perspective photograph. (b) Detailed photograph of TMRA placement. (c) Schema of the measurement system.

metal sheet are plotted as a benchmark. It is found that the SLLs are significantly reduced by time modulation. The comparisons of simulated and measured SLLs are summarized in the Table. Except the SLL of the -1st side lobe, all other SLLs are essentially near -20 dB. Note that SLL of the -1st side lobe is slightly larger than other side lobes. This is caused by the finite distance between the Tx and TMRA and this phenomenon can be observed in the theoretical result. That is, the experimental target is achieved. In addition, it can be observed that the measured results agree well with the theoretical results, which verifies the correctness of the measurement results. Note that the drop of the received power in the range of $[-20°, -10°]$ is mainly caused by the Tx antenna's blocking of the reflected wave during the measurement. The other imperfection observed in measured results of using time modulation is mainly attributed to the existence of the socket area's ground of the fabricated prototype, whose scattering field interferes with the original scattering field produced by TMRA's aperture only. It is worth mentioning that the maximum scattering intensity of the temporal modulation results is only 1.9 dB smaller than that of the metal sheet results, corresponding to 64.6 % TMRA efficiency, which indicates the good efficiency characteristics of the proposed 1-bit TMRA. The losses are mainly caused by the appearance of harmonic components and the loss of diodes, with theoretically calculated values of 1.45 dB and 0.55 dB, respectively. In summary, the time modulation characteristic of the proposed 1-bit TMRA is successfully verified by the experiment.

To further evaluate the performance of the time modulation, the normalized scattering patterns for both Co-Pol and Cro-Pol of realizing equal SLLs of -15 dB and -30 dB are measured and plotted together with the results of form equal -20 dB SLLs in Fig. 3.19. Note that the measured results of 45° incidence are also measured to verify the capability of time modulation at other incident angles. As can be seen in Fig. 3.19(a), the measured main beams are the same for the different time sequences, while the side-lobes are different, which indicates that the time modulation achieves effective control of the SLLs. Specifically, the equal -15 dB and -20 dB SLLs are clearly successfully achieved. The results of forming -30 dB SLLs show that only the reduction of the first SLL is achieved, while the other SLLs are not effectively controlled. This is also caused by the interference of the ground of socket area discussed previously. Note that the interference will be more severe when trying to achieve lower SLLs. This is because

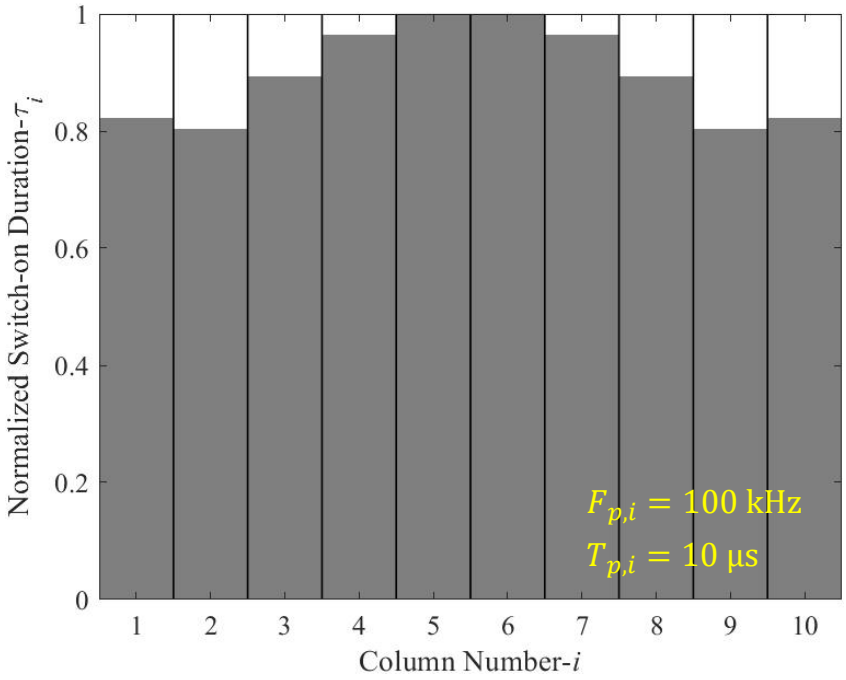

(a)

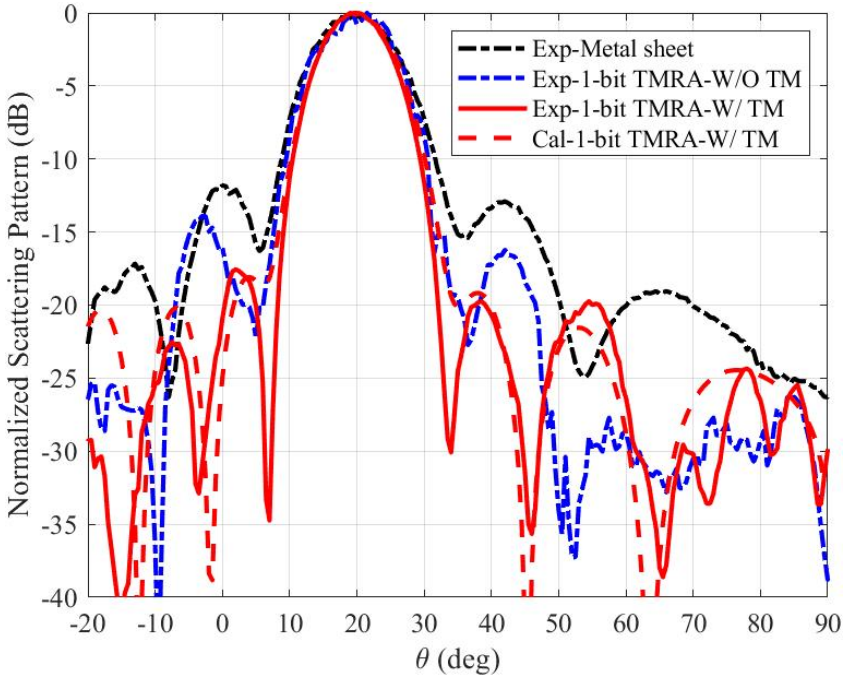

(b)

Figure 3.19: Measured scattering pattern of different SLLs. (a) $-20°$ incidence.(b) $-45°$ incidence.

achieving lower SLLs requires smaller induced currents at the edges of TMRA's aperture, while the induced currents generated by the ground of the socket area on either side of the aperture are very large. Although the absorbing material is used in experiments to decrease the induced current by the ground, when the required induced current at the edges of TMRA's aperture is smaller than the induced current from the ground, the latter will have a decisive role in the generation of SLLs. This is the reason why -15 dB and -20 dB SLLs can be observed, while -30 dB and lower SLLs cannot be observed by this fabricated prototype. In terms of the SLLs control, the results in Fig. 3.19(b) and Fig. 3.19(a) are basically the same, demonstrating that the effect of time modulation is not affected by the incident angle. Furthermore, high polarization purity can be observed from all measured Cro-Pol results.

The variation of the 1-bit TMRA radiation characteristics with frequency when using the time modulation is discussed below. The maximum scattering strength of the main beam does not fluctuate more than 1 dB over the entire measurement band (10.75 GHz-11.2 GHz). Note that we define an SLL bandwidth as the frequency range in which the difference between the first right SLL and the design target (-20 dB in this experiment) does not exceed 1dB. The experimental results show that the SLL bandwidth exceeds 250 MHz. However, from the signal transmission point of view, it is necessary for the bandwidth of the time-modulated signal to be smaller than the time modulation frequency F_p (100kHz in this work) to avoid spectrum aliasing [70]. That is, the operating bandwidth of the proposed 1-bit TMRA system is mainly limited by the time modulation frequency.

Therefore, the normalized scattering patterns for different time modulation frequencies are also measured and are plotted in Fig. 3.21. From 1 kHz to 1 MHz, the measured results remain essentially the same, which verifies that the modulation frequency does not affect the scattering characteristic of the TMRA under the time modulation state. Note that in this experiment, the upper limit of the modulation frequency is determined by the function generator. This is because when the modulation frequency exceeds 1MHz, the duty cycle of the square wave signal generated by the function generator does not satisfy the time sequence requirement of forming -20dB SLLs. In most case, the modulation frequency is determined by the operating frequency of the switching components (e.g., diodes, MEMS, etc.) and the operating frequency of the time signal generated by the control board. Note that the time modulation frequency of TMRA applied to

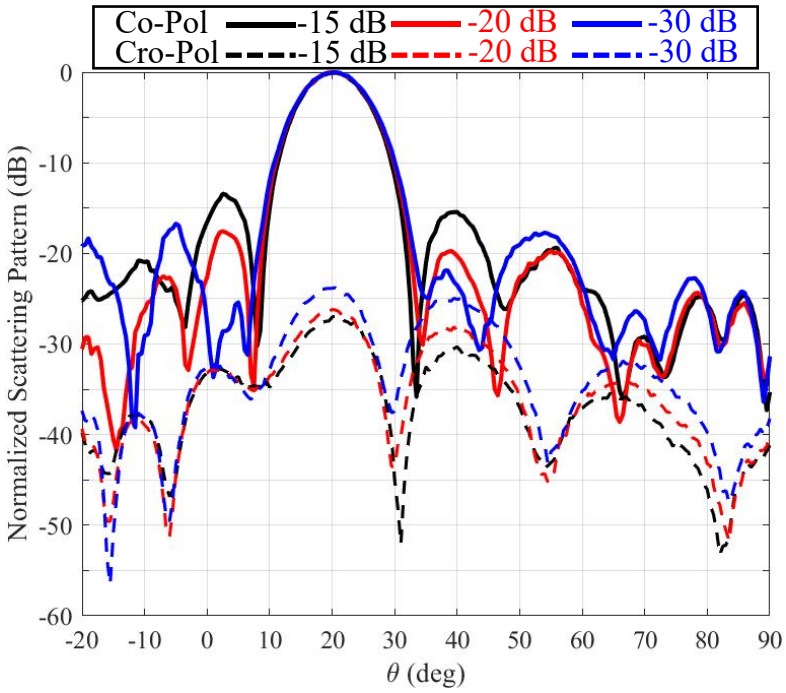

(a)

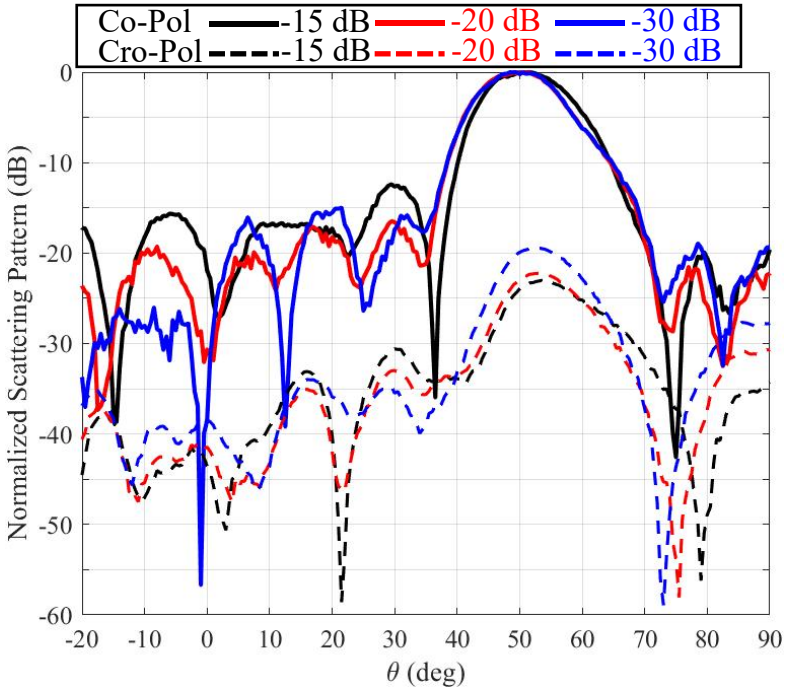

(b)

Figure 3.20: Experimental results. (a) Switch-on duration τ_i. (b) Measured normalized scattering patterns.

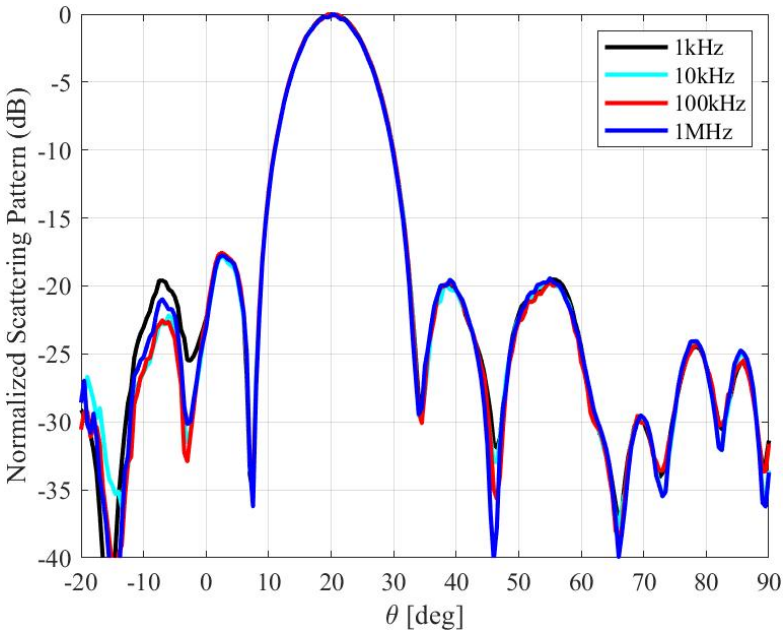

Figure 3.21: Measured scattering pattern of different modulation frequencies.

communication can only reach a few MHz [62] at this stage, which is suitable for narrowband communication. However, with the development of semiconductor technology, TMRA with larger signal bandwidth will meet the requirements of more communication scenarios.

Although the 1-bit TMRA prototype is fabricated and validated in X-band in this work, the effectiveness of time modulation technology is independent of the carrier frequency (as long as much larger than the time modulation frequency). Therefore, the proposed 1-bit TMRA concept can be implemented in any frequency band of interest, such as sub-6G, milli-wave or THz band. Also note that although the proposed 1-bit TMRA works in single-linearly polarization, the initial element structure used in this work is possible to be modified to realize dual-linear polarization [71], which is an important requirement for RIS applications in mobile systems. It can be inferred that the complicated bias circuit design would be one of the biggest challenges, and we believe this issue would be addressed in future research to make the proposed 1-bit TMRA more practical.

It is worth pointing out that the interference from the socket area's ground is severe, which deteriorates the overall performance of the fabricated 1-bit TMRA prototype. Although the interference is greatly reduced by covering the absorbing material in the experiment, it cannot be completely eliminated. It is for this reason that leads to the shift of the 1-bit frequency point, increasing the SLLs of beam scanning and limiting the effect of time modulation. However, it is not the drawback of the proposed 1-bit TMRA concept, and experiments have fully validated the effects of the proposed concept. In addition, to further improve the performance, we think a well-designed prototype layout, larger aperture size, and more accurate modeling of diodes should be further developed in the future.

3.5 Summary

In this Chapter, a new RIS implementation named 1-bit TMRA with real-time switchable phase or amplitude control capacities was proposed. A 10×10 1-bit TMRA prototype operating at the carrier frequency of 10 GHz was fabricated and validated by a series of experiments. The proposed 1-bit TMRA successfully realized beam scanning in the range of $10^\circ - 50^\circ$ by setting the corresponding 1-bit quantization phase to each element, which verifies the 1-bit phase control ability. The measured maximum gain is 15.6 dBi with a corresponding aperture efficiency of 21.1 % at 11.1 GHz. The amplitude control ability was verified by shaping the scattering pattern with low SLLs through applying time modulation. A 20 dB Chebyshev pattern was realized by the proposed 1-bit TMRA with a TMRA efficiency of 64.43 %, indicating efficient time modulation characteristic. Moreover, it is shown that it is not the radiation characteristic bandwidth (i.e., gain and SLL bandwidth) but the time modulation bandwidth which is the key factor limiting the bandwidth of 1-bit TMRA operation. The experiment also validated that the modulation frequency does not affect the radiation characteristics of 1-bit TMRA under the time modulation state.

Benefit from the established corresponding relationship between 1-bit RRA and PMTS, it is possible to use two anti-phased reflection states of 1-bit RRA to realize TMRA, which make the proposed 1-bit TMRA versatile and more practical compared with conventional TMRAs. Furthermore, the time modulation function is naturally introduced into a 1-bit

RRA system with structure unchanged, reducing the system complexity.

The findings of this study can be used as a resource for refining the theory of time modulation technique-based RRA design. The proposed 1-bit TMRA has practical potential in RIS applications, and further developments will contribute to the beyond 5G and 6G technologies of the future.

Chapter 4

TMRA with Real-Time Both Phase and Amplitude Control Ability for Enhanced-Efficiency Beam-Forming

4.1 Introduction

In the last Chapter, a 1-bit TMRA with switchable phase or amplitude control ability is successfully designed and verified. However, it can only work in the phase control state or the amplitude control state at a certain moment, which is insufficient to realize beam-forming. To address this problem, a method to design a TMRA with following features/characteristics are analyzed and proposed in this Chapter:

1. Simultaneous and independent control of both amplitude and phase
2. Operating at center frequency
3. Enhanced efficiency compared with conventional TMRAs.

4.2 Operating Principle

To control the amplitude and phase of the reflection coefficient simultaneously and independently, we need to start from the scattering mechanism of TMRA. The array factor of the TMRA scattering pattern can be expressed as:

$$AF(\theta,\varphi)=\sum_{h=-\infty}^{\infty}\sum_{m=1}^{M}\sum_{n=1}^{N}E_{inc}(\theta,\varphi)\Gamma_{mn}^{RRA}\Gamma_{mn}^{TMRA} \tag{4.1}$$

where Γ_{mn}^{RRA} represents the reflection coefficient generated by RRA, and Γ_{mn}^{TMRA} represents the TM reflection coefficient, which can be expressed as:

$$\begin{aligned}\Gamma_{mn}^{RRA}&=|\Gamma_{mn}^{RRA}|e^{j\varphi_{mn}^{RRA}}\\ \Gamma_{mn}^{TMRA}&=|\Gamma_{mn}^{TMRA}|e^{j\varphi_{mn}^{TMRA}}\end{aligned} \tag{4.2}$$

Since our designed TMRA operates at the carrier frequency, we are only concerned with the scattered field at the carrier frequency component, which can be written as

$$AF_0(\theta,\varphi)=\sum_{m=1}^{M}\sum_{n=1}^{N}E_{inc}(\theta,\varphi)\cdot|\Gamma_{mn}^{RRA}|e^{j\varphi_{mn}^{RRA}}\cdot|\Gamma_{mn}^{TMRA}|e^{j\varphi_{mn}^{TMRA}} \tag{4.3}$$

Based on the discussions in the previous two chapters, it is known that, in theory, RRA can only control the phase of the reflection coefficient. Additionally, TM can only generate TM excitation for the amplitude of the reflection coefficient at the carrier frequency, i.e., $\varphi^{TM}=0$. Therefore, the above equation can be rewritten as:

$$AF_0(\theta,\varphi)=\sum_{m=1}^{M}\sum_{n=1}^{N}E_{scat}(\theta,\varphi)|\Gamma_{mn}^{TMRA}|e^{j\varphi_{mn}^{RRA}} \tag{4.4}$$

where $E_{scat}=E_{inc}\cdot|\Gamma_{mn}^{RRA}|$.

It can be seen that the phase and amplitude of the element are controlled by RRA and TM, respectively. In other words, if RRA and TM function can be independently

and simultaneously controlled, the independent controllability of the element's reflection amplitude and phase can be achieved, allowing TMRA to achieve beam-forming at the carrier frequency.

The schematic of Q-bit TMRA is shown in Fig. 4.1 below. Theoretically speaking, RRA can achieve arbitrary phase states. Without loss of generality, Q-bit RRA is used for analysis in this work. In the schematic diagram, Q-bit RRA is represented by a phase shifter network with L ($L = 2^Q$) branches, where each branch corresponds to a phase state of the Q-bit. The TM function is represented by a switch that can switch between the L branches. When using TMRA for beam-forming, the phase states of each element are set according to the desired phase distribution. Then, a time sequence is applied to the switch to switch between the preset phase and other phases, achieving the desired amplitude distribution. However, it should be noted that since there are L different phase states, there are countless ways to switch between the preset phase and the other phases, which increases the complexity of analysis and implementation.

To address this issue, an anti-phase switching method inspired by the 1-bit PMTS from the previous chapter is proposed. Specifically, when implementing the TM function, we restrict the switching of the switch to switching from the preset phase to its opposite phase and from the opposite phase back to the original preset phase. Assuming the preset phases are φ^i and its anti-phase is φ^j, and they have the following relationship:

$$\varphi^j = \varphi^i + \pi \tag{4.5}$$

Thus, the corresponding PMTS can be derived, as shown in Fig. 4.2. The excitation amplitude of the TM at the carrier frequency can be obtained by the following equation:

$$\Gamma_{mn,0}^{TM} = \tau_{mn}^{\varphi^j} - \tau_{mn}^{\varphi^i} = 2\tau_{mn}^{\varphi^j} - 1 \tag{4.6}$$

With the proposed anti-phase switching method, it is convenient and efficient to design a TMRA with beam-forming capability at the carrier frequency.

4.3 Theoretical Analysis

In this section, we validated the effectiveness of the proposed method through theoretical calculations. Assume a TMRA with 15×15 elements and the element interval is half

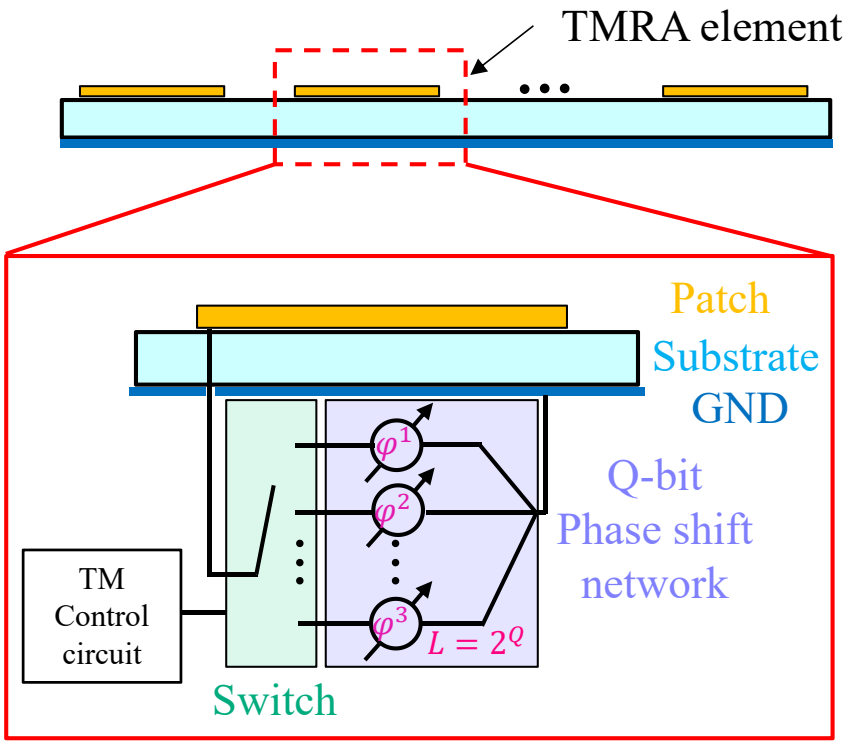

Figure 4.1: Measured scattering pattern of different modulation frequencies.

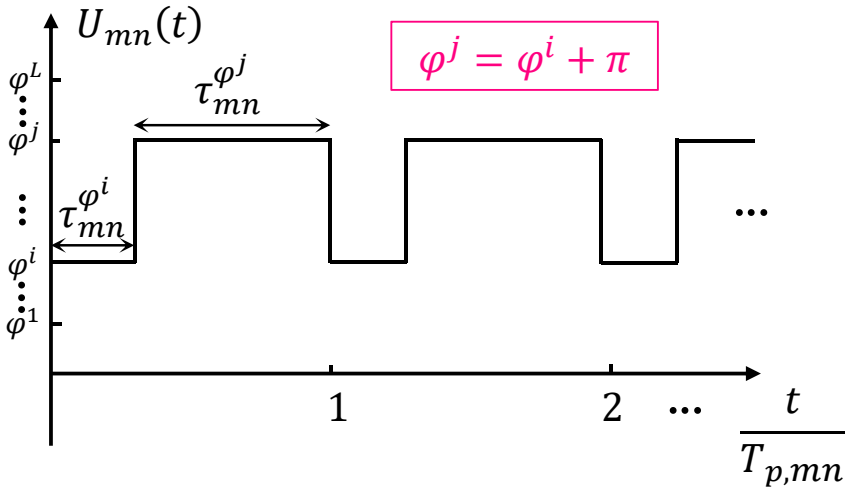

Figure 4.2: Measured scattering pattern of different modulation frequencies.

a wavelength of the carrier frequency. The incident wave is a vertically incident plane wave. The objectives of the beam-forming are:

1. Achieving a 20dB Chebyshev pattern
2. Scanning within the range of 10 to 50 degrees

In the theoretical calculations, we design the TMRA based on the proposed method using a 4-bit RRA, i.e., Q=4. To accurately evaluate the effectiveness of the proposed method, we also calculate the results for a 4-bit RRA and a conventional TMRA that uses the first harmonic component for beam-forming (referred to as 1st harmonic TMRA) as a reference. The theoretical calculation results are shown in Fig. 4.3. The black dashed line, blue dashed line, and red solid line represent the results for the 4-bit RRA, the 1st harmonic TMRA, and the proposed TMRA, respectively.

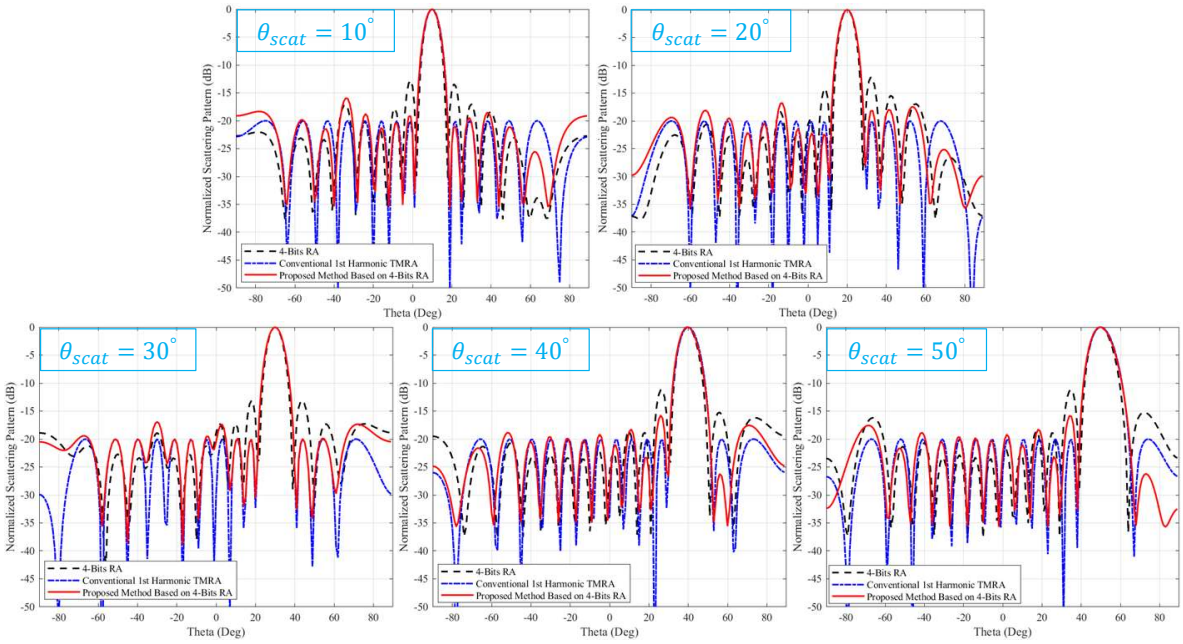

Figure 4.3: Theoretical calculation results of beam-forming based on 4-bit RRA.

Firstly, it can be observed that the 1st harmonic TMRA achieves the best beam-forming performance. This is because the 1st harmonic TMRA operates at the harmonic frequency component, allowing for precise control of both amplitude and phase using TM. However, it is difficult to be directly applied to existing communication systems

because it changes the frequency of the scattered wave, and the excitation amplitude of the TM at the harmonic frequency component is smaller than that at the carrier frequency component, resulting in lower efficiency. This is the reason why this thesis focuses on the design of TMRAs operating at carrier frequencies. Observation of the result plot of the proposed TMRA reveals that the scanned pattern of the scattered beam from 10 degrees to 50 degrees is obtained, and the goal of beam steering is achieved. On the other hand, the proposed TMRA basically achieves the goal of beam-forming with a 20 dB Chebyshev pattern. It is worth noting that the SLL is slightly higher than - 20 dB for some angles, which is due to the phase error of the 4-bit RRA and will be explained in detail later.

To fully evaluate the effectiveness of the proposed method, the directivity of the proposed method and the related reference model are also calculated and compared, and the results are shown in Fig 4.4(a). It should be noted that here we additionally calculate the results for ideal beam steerable RA. The ideal beam steerable RA refers to the ideal steerable RA with continuous and accurate phase compensation, denoted as IBSRA, which represents the maximum directivity that can be achieved with the same physical aperture. The green, blue and red solid lines in the Fig 4.4(a) represent the calculated results of IBSRA, 1st harmonic TMRA and proposed TMRA, respectively. The green dashed line refers to the theoretical variation law of the directivity with the scanning angle. Firstly, it can be seen that the directivity of the proposed TMRA is smaller than those of the ISBRA. In terms of the beam-forming mechanism, this is the cost of achieving a 20 dB Chebyshev pattern while forming a taper in the aperture; in terms of the physical process, this is the result of transferring part of the scattered power to each harmonic component of the TMRA through TM. Comparing the results of the proposed TMRA with those of the conventional 1st harmonic TMRA, it is found that the directivity of the proposed TMRA is much larger than that of the 1st harmonic TMRA, with an improvement of nearly 4 dB. This is due to the higher excitation amplitude of the TM at the carrier frequency.

Furthermore, the efficiency analysis was also performed using the proposed method in Chapter 2, and the results are shown in Fig 4.4(b). It can be found that the proposed method can increase the TMRA efficiency from 26 % of the conventional 1st harmonic TMRA to 63 %, an improvement of nearly 1.5 times. In addition, it can be found

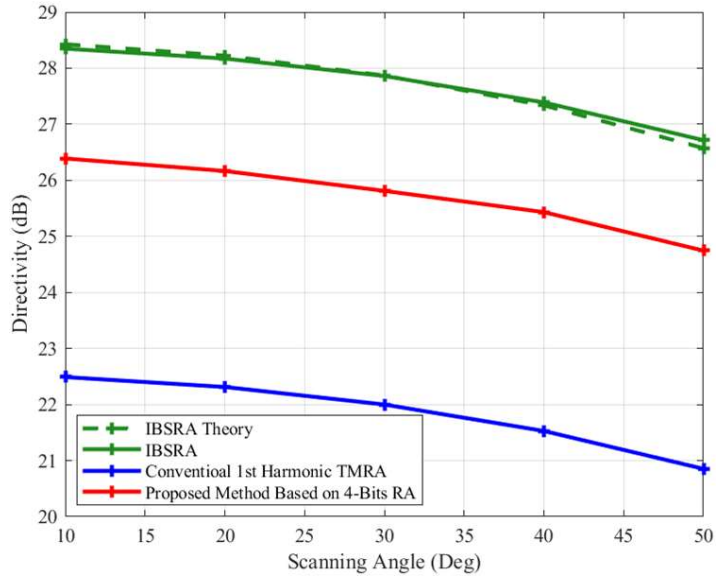

(a)

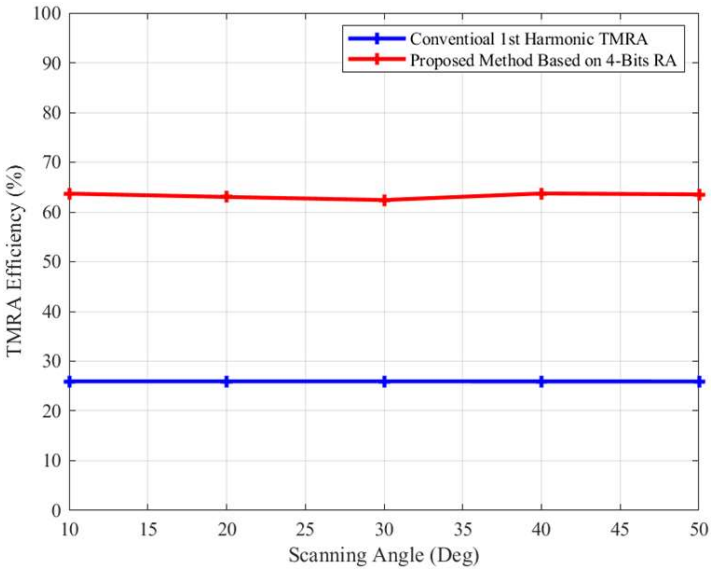

(b)

Figure 4.4: Scattering performance of 4-bit TMRA in terms of (a) Directivity. (b) Efficiency.

that the TMRA efficiency almost does not change with the scanning angle. The above findings show that the proposed method has significantly higher efficiency compared to the conventional method. And it works at the center frequency, which has a good practicality.

In order to illustrate the effect of the number of phase quantization bits (equal to 2^Q) on the beam-forming effect, three sets of scattering pattern were calculated for the Q-bit based TMRA with Q=2, 4 and 6. The objective of the beam-forming is to form a 20 dB Chebyshev pattern while the main beam direction is pointing at 10, 30 and 50 degrees, respectively. The calculation results are shown in Fig. 4.5. It can be observed that at Q=2, in addition to the main beam, there is a large side and grating lobes in the direction of deviation from the main beam, and at Q=4, the SLL is well suppressed and the design goal of equal-20 dB sub-beam level is basically achieved except for a few angles. When Q=6, the SLLs are all less than -20 dB, achieving the design goal and in good agreement with the 1st harmonic TMRA results. As mentioned earlier, the phase control principle of Q-bit RRA is quantization sampling of continuous phase, and the quantization accuracy is $360°/(2^Q)$. When Q increases, the quantization accuracy increases, the smaller the error between the quantized phase and the continuous phase, and the closer the obtained pattern is to the desired target. Therefore, increasing the number of bits of RRA can reduce the quantization error by phase and thus improve the beam-forming effect of TMRA.

In addition, the effectiveness of the proposed method is investigated for different beam-forming targets. Keeping the remaining conditions of the above example unchanged, only the beam-forming target is changed to form a 30 dB Chebyshev pattern, and the results are calculated. The calculation results are shown in Fig. 4.6. Firstly, the same phenomenon as the above example can be observed, the larger the Q, the better the beam-forming effect. Secondly, it can be found that the result of Q=4 in the above example achieves the target of 20 dB Chebyshev pattern. In this example, the result of Q=4 still shows large SLLs and the design goal is not achieved. When Q=6, the SLLs are well suppressed and the design target is basically achieved, but there are still one or two angles with slightly higher SLLs. This shows that even if the Q is the same, when the target of beam-forming is different, the effect of beam-forming is also different. It can be concluded that a suitable Q value should be selected according to the target

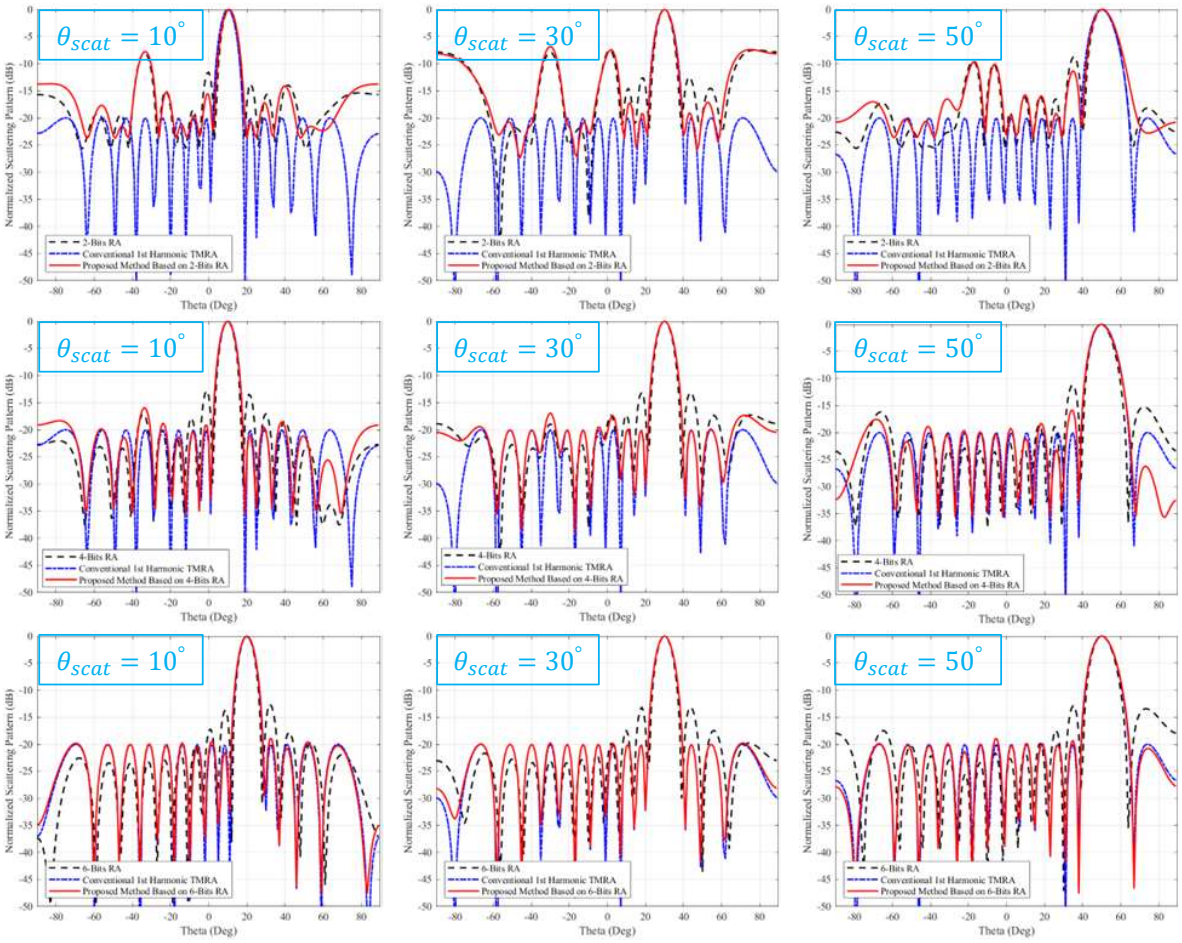

Figure 4.5: Theoretical calculation results of 20 dB Chebyshev pattern with different Q.

requirements to achieve the best balance of control effect and cost. This is because the larger the Q, the more difficult the design and the complexity and cost of the system will increase significantly. The above findings are of good use and guidance for practical applications.

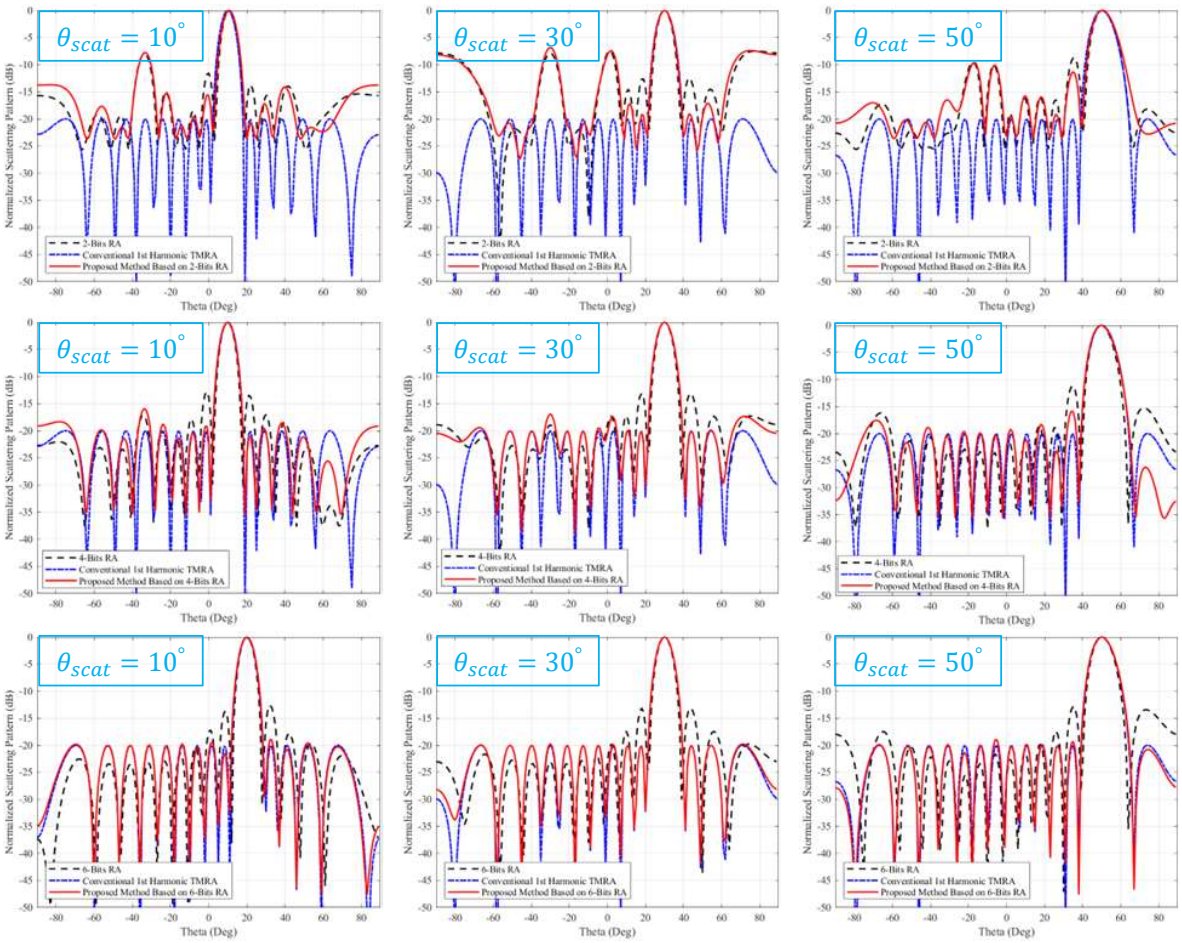

Figure 4.6: Theoretical calculation results of 30 dB Chebyshev pattern with different Q.

It should be noted that the effect of the number of phase quantization bits, or rather the phase error it causes, on the beam-forming effect is not specific to the proposed method. Even without the use of TM, the phase error causes a similar effect on the scattered beam, which can be observed in the results of the RRA in Fig. In other words,

the imperfections in the beam-forming results of TMRA based on low-bit RRA are caused by the phase error of the RRA and are not introduced by the proposed method, nor are they a drawback of the proposed method. In order to show this conclusion more clearly, a series of resultant plots of beam-forming of TMRA based on Q-bit RRA, where Q is equal to 1 to 6, respectively, are calculated. For comparison, the target of beam-forming is set uniformly to form a 20 dB Chebyshev pattern and to steer the main beam direction to 40 degrees, and the rest of the conditions remain unchanged from the previous examples.

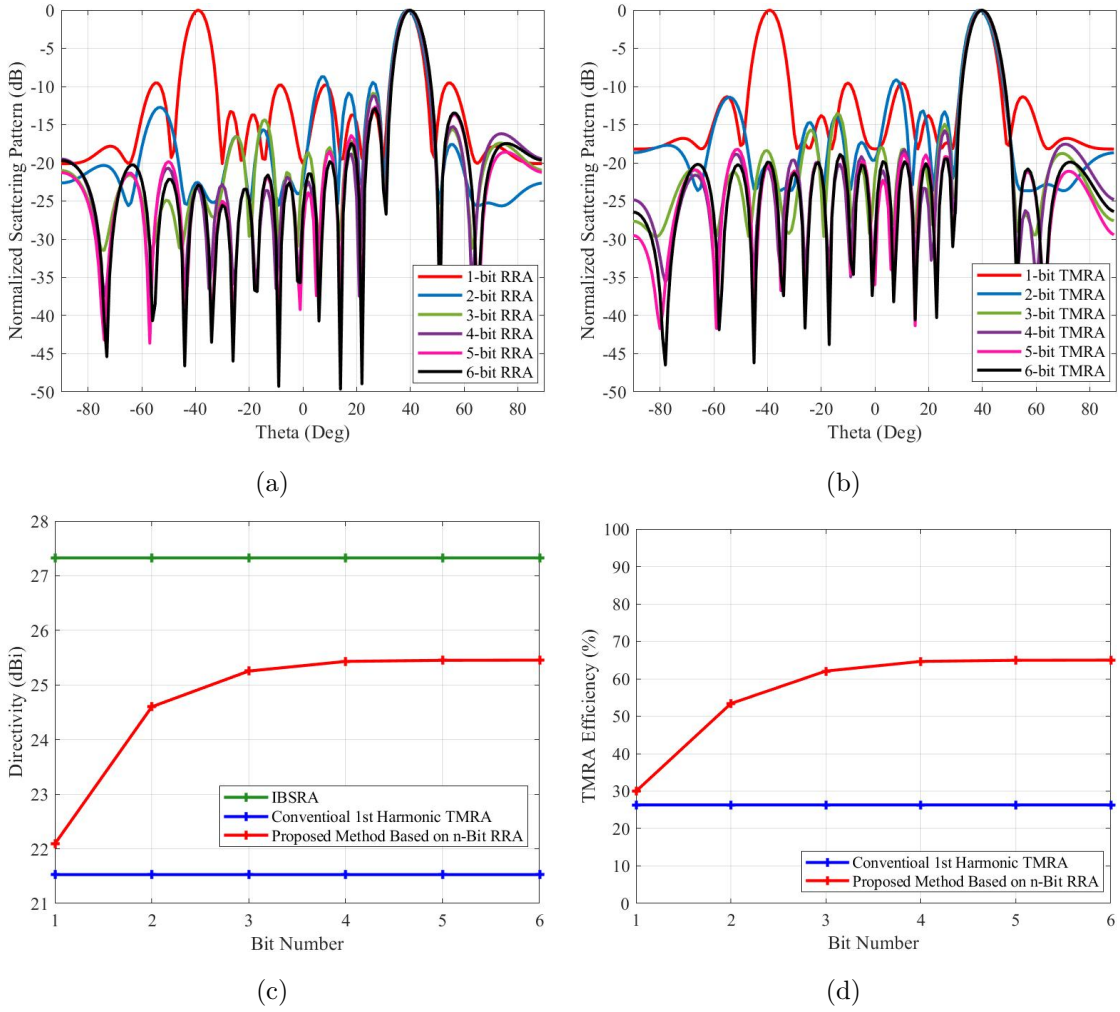

Figure 4.7: Effect of Q-bit phase quantization. (a) Scattering pattern of RRA. (b) Scattering pattern of TMRA. (c) Directivity of TMRA. (d) Efficiency of TMRA.

Fig. 4.7(a) shows the calculation results of Q-bit RRA. Because of the lack of amplitude control capability, the RRA is only able to achieve beam-steering of scattering pattern. It is evident that with the increase in Q, the SLLs exhibit a diminishing trend. When Q is less than or equal to 3, a significant high side-lobe appears at and near the mirror angle ($-40°$) of the design steering angle. It is worth pointing out that when Q=1, a grating-lobe with the same shape as the main beam and the same maximum level value appears at -40 degrees. This is due to the fact that the phase distribution after 1-bit phase quantization is symmetric about the center of the aperture, and thus the superposition effect of the phase is the same at the angle symmetric about the center of the aperture, which leads to the appearance of the grating-lobe at the mirror angle of the main beam. This phenomenon is discussed in detail in [72] and [73]. When Q is greater than or equal to 4, the above-mentioned high side-lobes no longer appear and the scattered beams of different Q values basically coincide. These results show that the phase error itself has an effect on the beam and that this effect decreases as the number of phase quantization bits increases. As shown in Fig. 4.7(b), a similar pattern to the Q-bit RRA can be observed, which indicates that the difference between the achieved effect of beam assignment and the target is caused by the phase error rather than the TM. In addition, it can be found that when Q is less than or equal to 3, although the side-lobes at certain angles are effectively suppressed, the overall design goal is not achieved. When Q is greater than or equal to 4, the beam assignment objective is basically achieved. This also verifies the above conclusion that a suitable Q should be selected according to the target requirements.

The trends of the directivity and TMRA efficiency with Q are also analyzed. The calculated results of the directivities are shown in Fig. 4.7(c). Firstly, it can be found that the directivity of the proposed Q-bit TMRA is much larger than that of the 1st harmonic TMRA. Secondly, it can be found that the directivity of the proposed method increases significantly with the increase of Q when Q is less than or equal to 3. Specifically, the directivity at Q=3 is 3 dB larger than that at Q=1. However, the improvement of the directivity is very limited when increasing the Q value further. This observation suggests that the directivity does not exhibit a continuous increase with the incremental values of Q, but instead reaches an upper limit dictated by the beam-forming target. This finding further validates the previous conclusion that opting for a larger Q value does

not necessarily lead to improved performance. In this example, a maximum enhancement of 4 dB in the directivity can be achieved using the proposed method compared to the conventional method. A similar pattern appears in the variation of the TMRA efficiency, as shown in Fig. 4.7(d). The maximum TMRA efficiency can be increased from 26 % to 65 % using the proposed method compared to the conventional method. It should be noted that the above discussion shows that the proposed method can significantly improve the directivity and efficiency of beam-forming compared to the conventional method. Note that even for the least effective 1-bit TMRA, the correlation performance surpasses that of the conventional method, thus highlighting the enhanced efficiency characteristic of the proposed method.

4.4 Analysis Based on 1-bit TMRA

Based on the discussion in the preceding section, it is evident that RRAs with higher bit number ensure improved beam-forming. Nevertheless, the design and rapid switching between different phase states of multi-bit RRAs pose a notable challenge. As outlined in Chapter 1, varactor-based diodes or liquid crystal-based RRAs offer relatively easier implementation of multi-bit RRAs, but their switching speed is insufficient to meet the millisecond or even faster switching speed requirements of RIS. For PIN diode-based RRA, there are only a few reported implementations of 2-bit RRA. Presently, only 1-bit RRA-based TMRA can be employed for experimental verification of the proposed method. Consequently, it becomes imperative to undertake a theoretical analysis of the proposed method's implementation on a 1-bit RRA-based TMRA before conducting experiments. Here, three beam-forming targets are selected for theoretical calculation and analysis, denoted as Cases 1-3, respectively, with the following targets:

1. Case 1: Incidence angle equal to $(0°, 0°)$, scattered beam pointing at $(20°, 90°)$, forming a 20 dB Chebyshev pattern
2. Case 2: Incidence angle equal to $(0°, 0°)$, scattered beam pointing at $(30°, 90°)$, forming a 20 dB Chebyshev pattern
3. Case 3: Incidence angle equal to $(10°, 270°)$, scattered beam pointing at $(40°, 90)$, forming a 20 dB Chebyshev pattern

Note that in order to predict the experimental effect, the calculations are performed here using a 10×10 array with the same configuration as the 1-bit TMRA prototype. The results of the calculations are shown in Fig. 4.8.

First and foremost, it is evident that the results of each arithmetic example successfully achieve the beam-steering objective. Furthermore, the SLLs near the main beam is moderately suppressed compared to the 1-bit RRA, highlighting the effectiveness of TM. It is important to note that the grating-lobe at the mirror angle of the main beam, as well as the imperfect beam-forming results, stem from the phase error associated with 1-bit phase quantization, which has been addressed in the preceding section. These issues are not inherent problems of the proposed method. Moving on, the directivity and efficiencies of the TMRA for the three arithmetic example are also analyzed, with the results presented in Fig. 4.9. It can be observed that the proposed method surpasses the conventional 1st harmonic TMRA in terms of both directional coefficients and TMRA efficiency.

4.5 Control Mechanism and Realization

Once the decision to utilize a 1-bit TMRA for verifying the proposed method has been made, the subsequent step involves discussing the implementation of reflection coefficient amplitude and phase control. As outlined in Chapter 2, the fundamental basis for implementing the functionality of the TMRA lies in the control of its reflection coefficient. Additionally, since we design the TMRA using a PIN diode-based 1-bit RRA, the control of the reflection coefficient is effectively achieved by manipulating the bias voltage applied to the PIN diode. Therefore, without loss of generality, it is assumed that Γ^1 and Γ^2 correspond to the control voltages V^1 and V^2, respectively. First, consider applying a constant V^1 (which does not vary with time) to the mn-th element of the TMRA, as depicted in Fig. 4.10(a), which corresponds to a reflection coefficient with an amplitude Γ^1 and a phase φ^1. Next, apply a time sequence to this control voltage, switching between V^1 and V^2, as illustrated in Fig. 4.10(b). Assuming that the control voltage remains at V^1 for a normalized duration of τ^{V^1}, the TM amplitude excitation can be determined based on the theory introduced in the second section of this chapter. Importantly, this does not affect the original phase φ_1, as no TM amplitude excitation

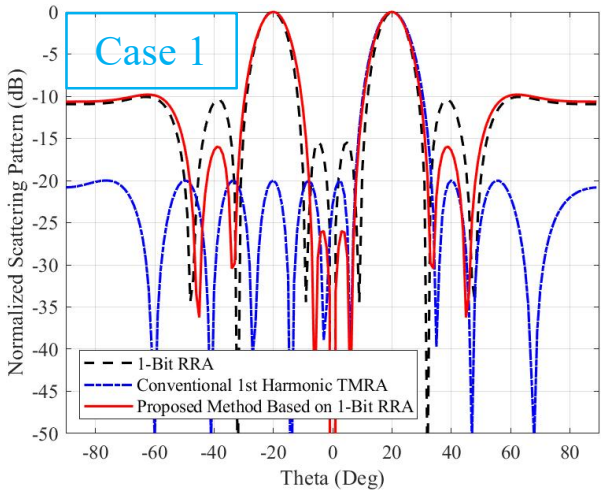

(a)

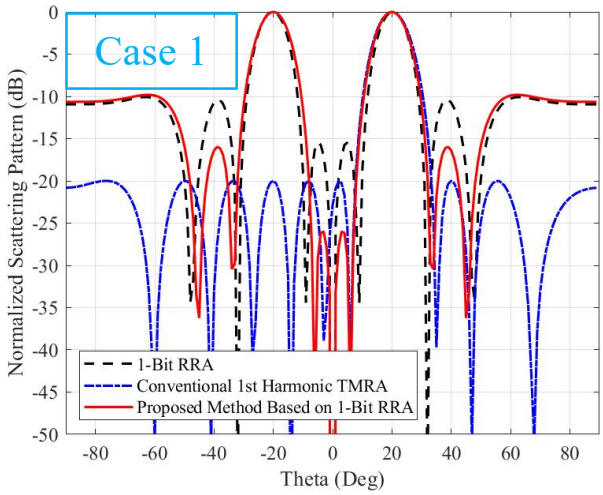

(b)

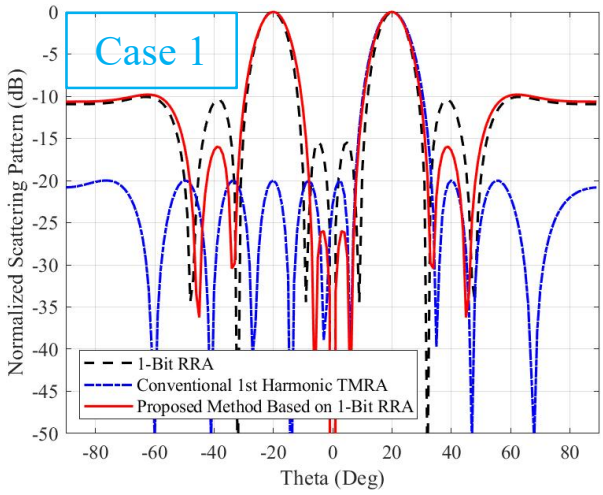

(c)

Figure 4.8: Theoretical calculation results of beam-forming based on 1-bit TMRA. (a) Case 1. (b) Case 2. (c) Case 3.

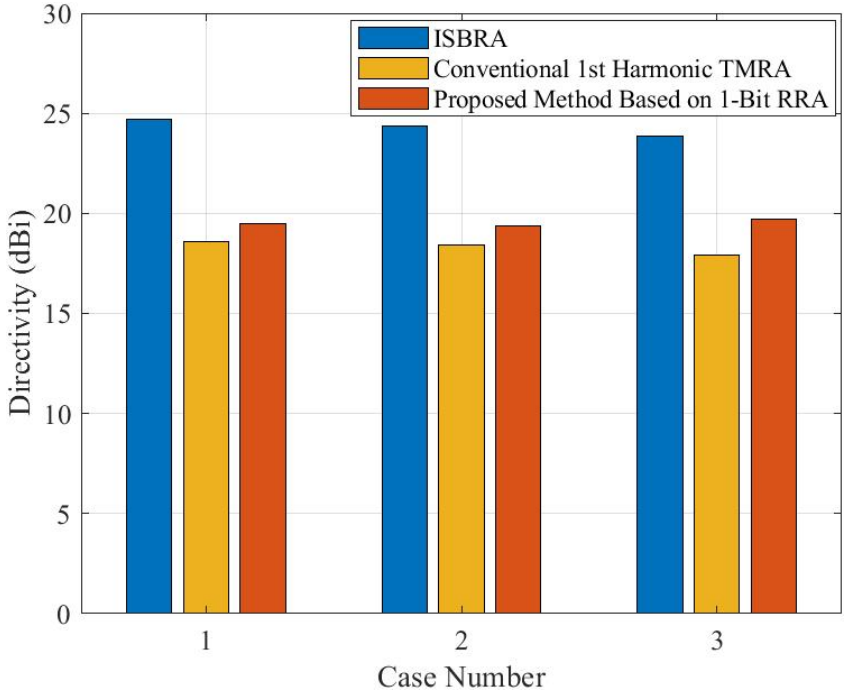

(a)

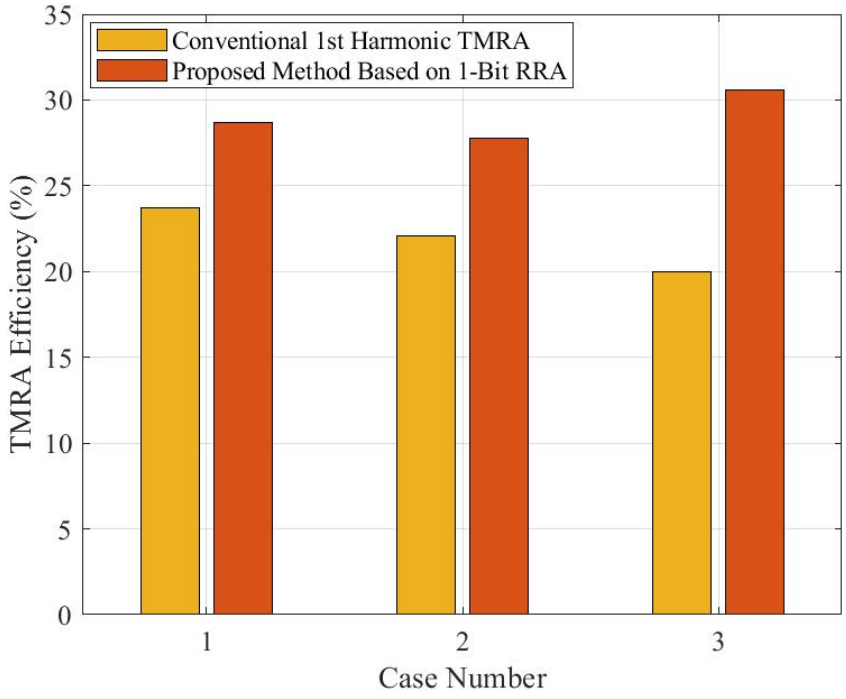

(b)

Figure 4.9: Scattering performance comparison. (a) Directivity. (b) Efficiency.

is generated. Consequently, a sequence of reflection coefficients can be achieved with a phase equal to φ^1 and arbitrary controllable amplitude. Similarly, when the start of the control voltage time sequence is positioned at V^2, a sequence of reflection coefficients with a phase equal to φ^2 and arbitrary amplitude can be realized, as indicated in Fig. 4.10(c) and (d).

It should be noted that for an ideal 1-bit RRA, the amplitude and phase adhere to the following relationships: $|\Gamma^1| = |\Gamma^2|$ and $\varphi^1 = \varphi^2 + \pi$. Consequently, the aforementioned four cases can be represented in the complex plane, as illustrated in Fig. 4.10(e). Firstly, a point is located on the circle with $|\Gamma| = 1$, corresponding to $|\Gamma^1|\varphi^1$, from which $|\Gamma^2|\varphi^2$ can be obtained. Secondly, depending on different values of τ, two sets of equivalent TM excitations with opposite phases and different amplitudes can be obtained, which are depicted in the figure. By employing this approach, the principle of simultaneous and independent control of reflection coefficient amplitude and phase, as proposed in this study, can be clearly demonstrated.

In a broader context, we introduce the concept of the basic control time sequence (BCTS), as depicted in Fig. 4.11. With these four variations of BCTS, it becomes possible to achieve two sets of reflection coefficients with arbitrary amplitudes but opposite phases. This capability enables the TMRA to achieve beam-forming at the carrier frequency.

Next, we will discuss the implementation of the aforementioned control method, specifically the design of the beam-forming control board. By observing the correlation between the states of BCTSs and the states of the actual applied voltage signals, it is observed that the control voltage signal of the 1-bit RRA (denoted as A), the TM time series control voltage signal (denoted as B), and the control voltage signal ultimately applied to the TMRA element (denoted as out) exhibit a logical relationship akin to the XNOR gate, as described in Fig. 4.12.

Based on the logical relationship described earlier, we have designed the beam-forming control board utilizing an XNOR gate chip. The schematic diagram of the board is presented in Fig. 4.13(a). The output of the XNOR gate chip is connected to the 1-bit TMRA unit, while the two inputs are the TM time series control signal (for amplitude control) and the 1-bit RRA control signal (for phase control). To achieve the two reflection states of the 1-bit RRA, the control signal of the 1-bit RRA is switched between a high level and a low level (ground) using a single-pole double-throw (SPDT) switch.

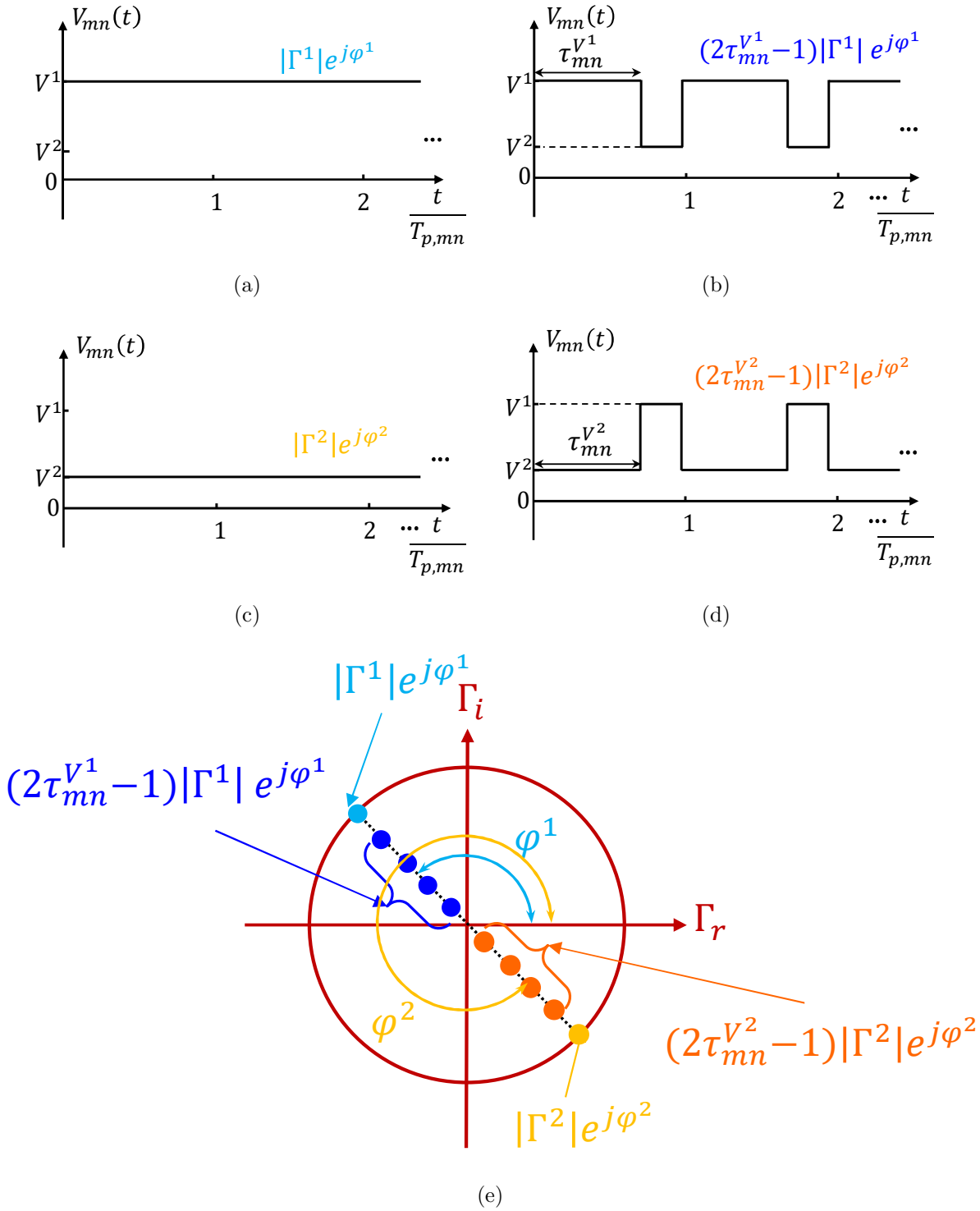

Figure 4.10: Principle of control mechanism. (a) Constant voltage start at V^1. (b) Vary voltage for TM Based on start point of V^1. (c) Constant voltage start at V^1. (d) Vary voltage for TM Based on start point of V^1. (e) Illustration of correspondence by complex plane.

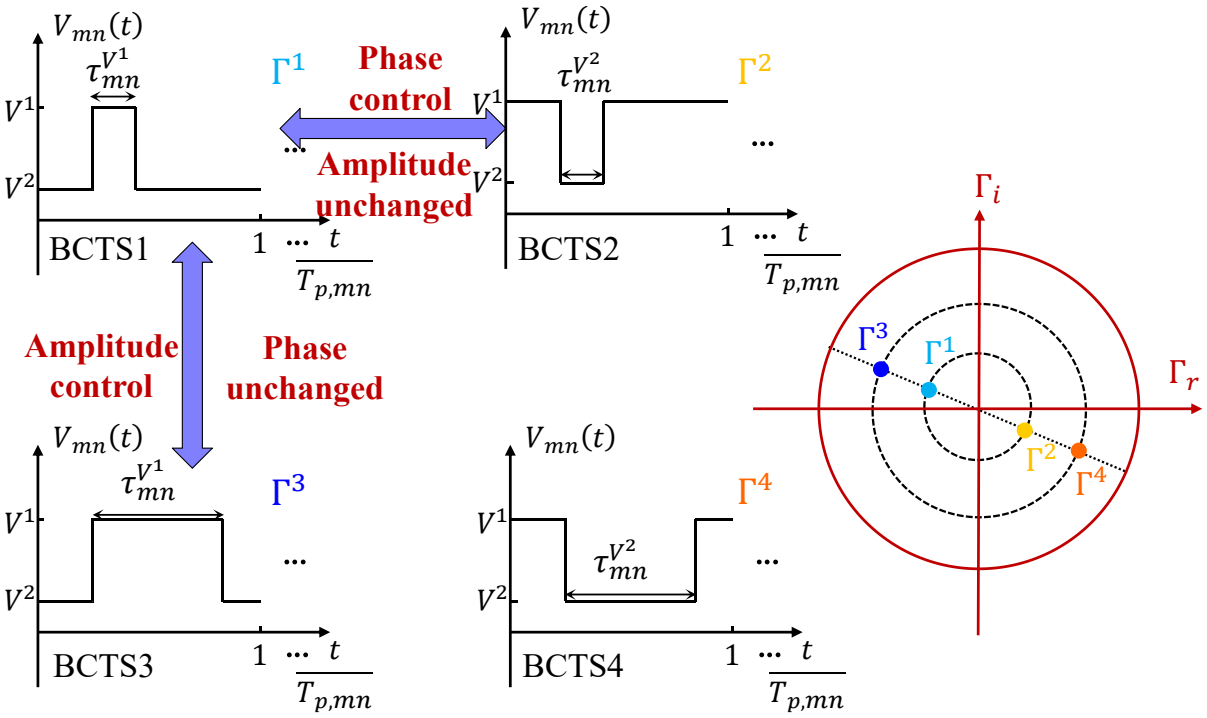

Figure 4.11: Illustration of BCTS

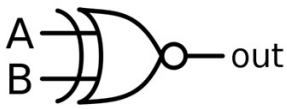

Voltage Signal of 1-bit RRA (A)	Voltage Signal of TM (B)	Voltage Signal of TMRA (out)
V^1	V^1	V^1
V^1	V^2	V^2
V^2	V^1	V^2
V^2	V^2	V^1

Figure 4.12: XNOR gate and corresponding truth table

Additionally, a LED connected to the control line of the 1-bit RRA serves as an indicator for the 1-bit status. As shown in Fig. 4.13(b), due to the complexity of the control circuit, a three-layer PCB was utilized for the design and fabrication. The final fabricated beam-forming control board is shown in Fig. 4.13(c).

4.6 Experiment Validation and Results

4.6.1 1-bit RRA Element and Prototype

Prior to conducting the experiments, it should be noted that due to the defective design of the 1-bit RRA prototype used in the previous chapter, the scattering from the floor of the socket area severely interferes with the scattering field of the TMRA aperture, leading to deviations of the test results from the theoretical design. To address this issue, a PIN diode-based 1-bit RRA with a magneto-electric dipole element structure operating at 10 GHz is used in experiment. The design of this 1-bit RRA is based on the structure reported in [74], and the element structure is depicted in Fig. 4.14, along with the fabricated 10×10 1-bit RRA prototype. The prototype design noticeably reduces the area of the sockets on both sides and eliminates the floor beneath the socket area, thus minimizing the impact on the TMRA's aperture.

4.6.2 Validation of Reflection Characteristic

The first experiment aims to verify the reflection characteristics of the 1-bit RRA prototype. The experimental setup, depicted in Fig. 4.15(a), is consistent with the environment used for measuring the reflection characteristics in the previous chapter. The distance R_{Tx} is set to 1.68 m, ensuring the far-field conditions for this prototype. During the experiment, the reflection coefficients of the 1-bit RRA were separately measured when diodes in the fully on and fully off states. The results, shown in Fig. 4.15(b), reveal several observations. Firstly, the phase difference between the two reflection states of the 1-bit RRA remains stable at approximately 180°, with the phase difference not exceeding $180° \pm 10°$ across the entire measurement frequency band. This indicates excellent 1-bit phase characteristics. Secondly, regarding the reflection amplitude, it is observed that

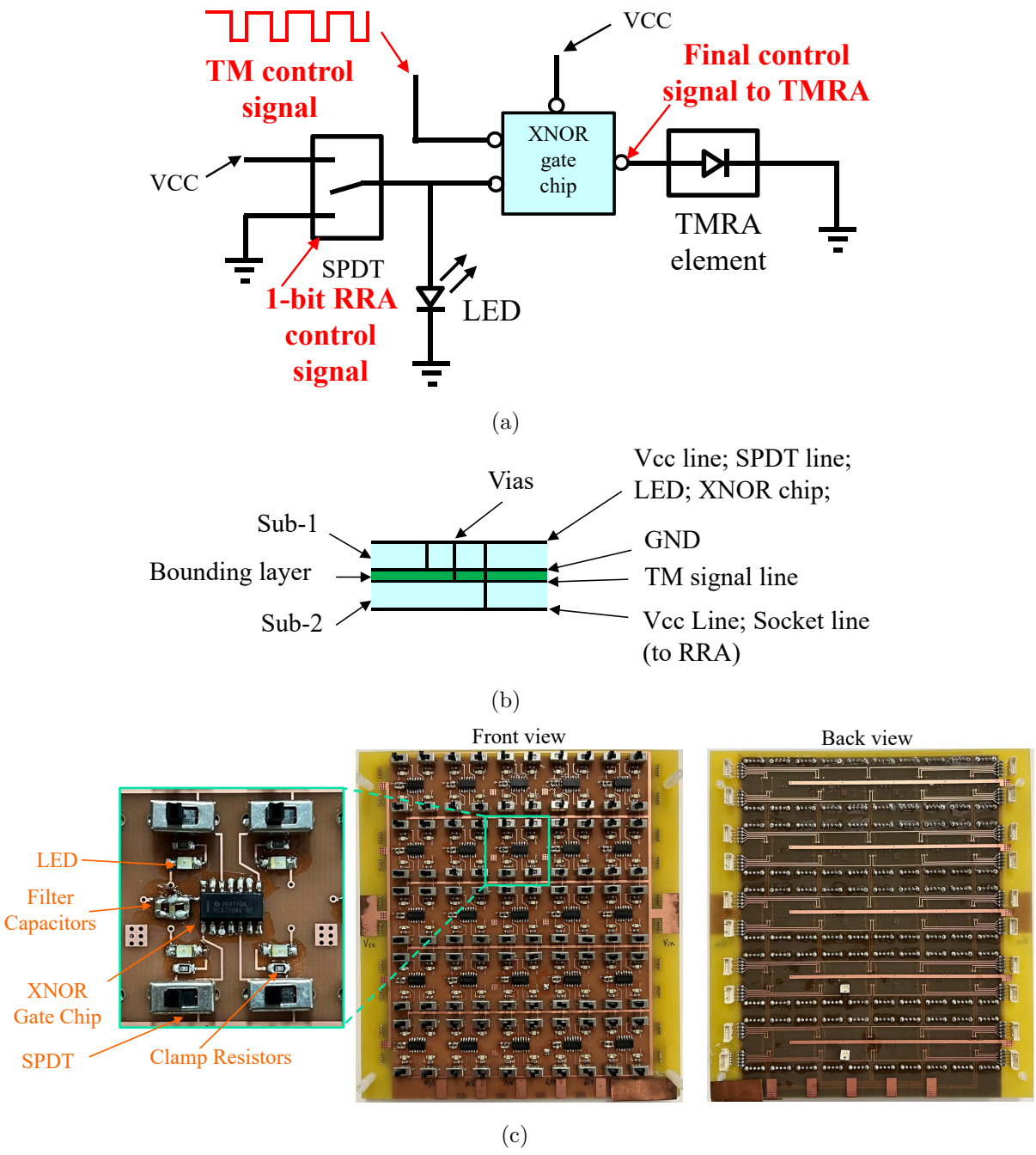

Figure 4.13: Design and fabrication of beam-forming control board. (a) Schematic of circuit. (b) Schematic of layer layout. (c) Photo of fabricated prototypre.

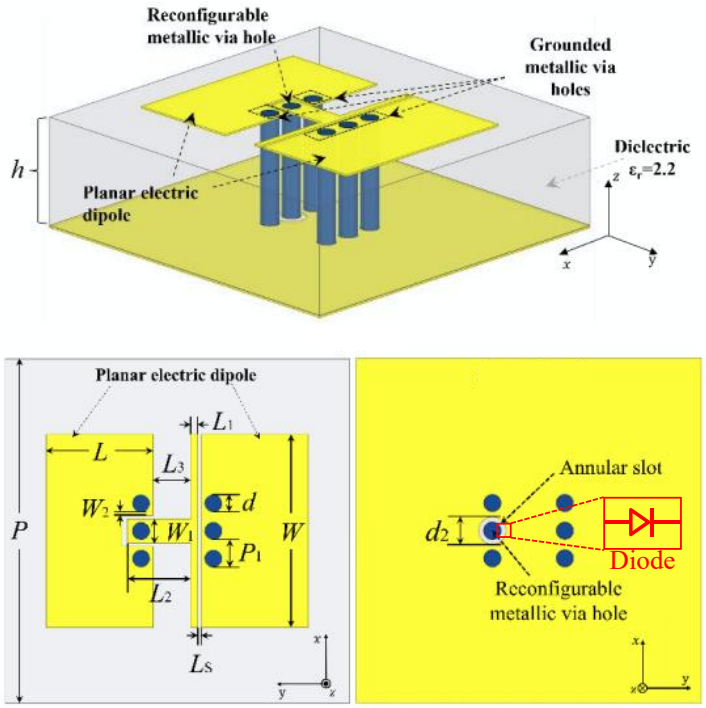

(a)

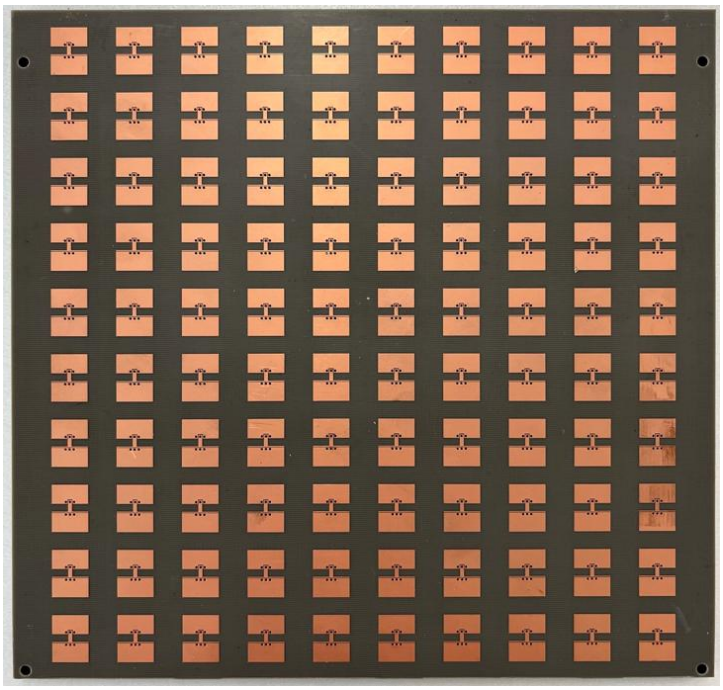

(b)

Figure 4.14: 1-bit RRA used in this work.(a) Element Structure. (b) Photo of fabricated 10×10 prototype.

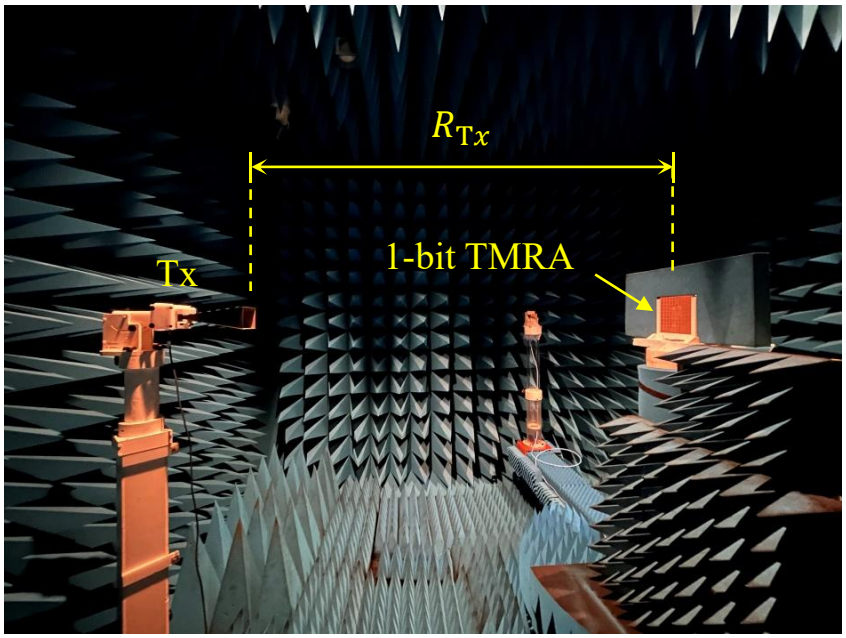

(a)

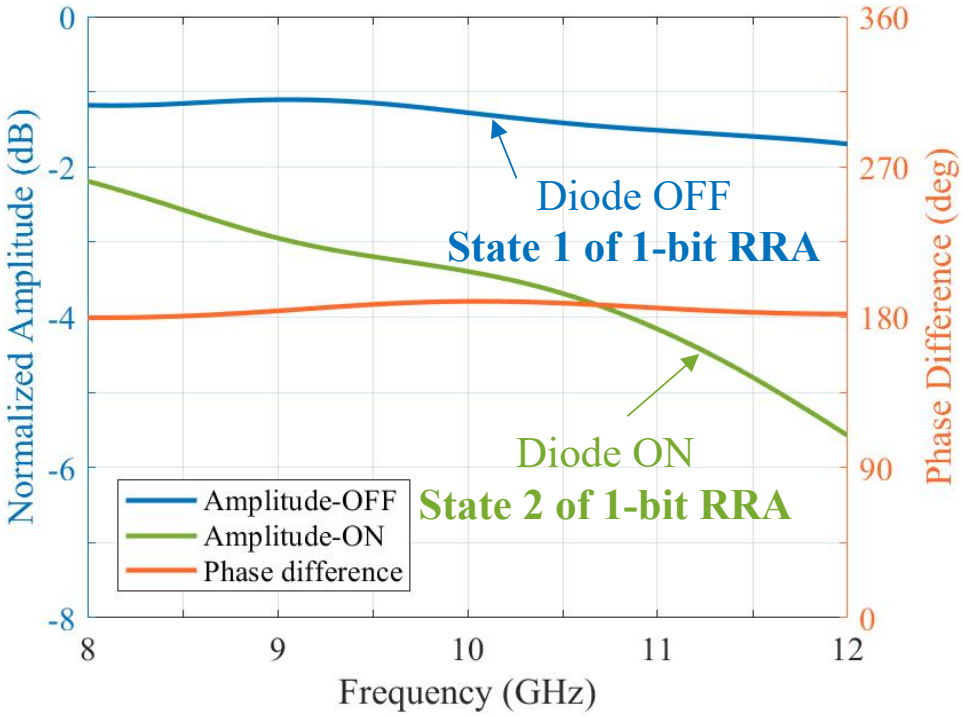

(b)

Figure 4.15: Measurement of reflection characteristic of 1-bit RRA prototype. (a) Experimental environment. (b) Experimental results of reflection coefficient.

the amplitude when the diode is fully on is smaller than when the diode is fully off, attributable to RF current losses when the diode is activated. At 10 GHz, the amplitude difference between the two reflection states is 2.1 dB, which is acceptable for a 1-bit RRA design based on PIN diodes. Based on the results obtained in this experiment, 10 GHz is selected as the operating frequency for the subsequent validation experiments.

4.6.3 Validation of Beam-Forming

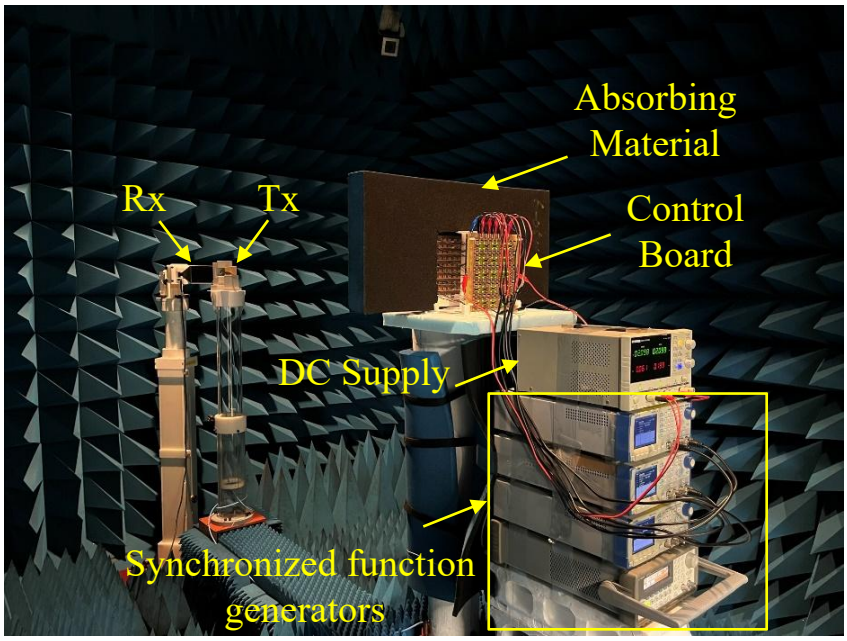

Figure 4.16: Experimental environment for validation of beam-forming

The second experiment aims to verify the effectiveness of the proposed beam-forming method using the 1-bit TMRA. The experimental setup, depicted in Fig. 4.16, is identical to the one utilized in the previous chapter to verify the TM function. The distances R_{Tx} and R_{Rx} are set to 1.3 m and 1.68 m, respectively, ensuring that both are situated in the far-field region of the TMRA aperture.

The TMRA is positioned at the center of the turntable and is supported by a 3-D printed supporter. It is shielded by specially cut absorbing material to minimize

interference from the beam-forming control board and associated wires located behind the TMRA. The voltage source and function generators are positioned on the lower rear side of the control board, and the center column of the rotary table in front of them is wrapped with absorbing material. This arrangement reduces scattering from the metal housing of these devices. The experiment is conducted at an operating frequency of 10 GHz, with a TM frequency of 100 kHz. The beam-forming objectives for this experiment are as follows:

1. Steering the direction of the scattered beam to 40 degrees.
2. Achieving a 20 dB Chebyshev pattern.
3. Achieving a 30 dB Chebyshev pattern.
3. Achieving a Binomial pattern.

Of particular significance is the presence of a considerable 1-bit phase quantization error, as revealed in the preceding theoretical analysis of 1-bit TMRA. This error imposes a hindrance to achieving the desired objective of perfect beam-forming (i.e., a scattering pattern with equal SLLs of -20 dB) when employing the proposed method with 1-bit TMRA. In light of this inherent limitation, we aim to substantiate the efficacy of our proposed method by assessing the degree of coincidence between the obtained measured results and the corresponding theoretical calculations. In essence, our verification entails aligning the experimental outcomes with the theoretical predictions of beam assignment using 1-bit TMRA. Therefore, while attaining a flawless target beam may prove unattainable, a successful demonstration of concordance between the test results and the theoretical expectations would affirm that the proposed method effectively modulates the beam as anticipated by theory.

According to the requirements of 40 ° beam-steering and 20 dB Chebyshev pattern, the corresponding phase distribution and amplitude distribution (expressed in time sequence) are calculated and set respectively, as shown in Fig 4.17(a). In the figure of phase distribution, the on (yellow zone) and off (blue zone) states of the diodes are realized by the voltages V^1 and V^2, respectively. Regarding to the figure of time sequence shown in Fig 4.17(b), the on (dark zone) and off (white zone) states of the diodes are realized by the voltages V1 and V2, respectively. The measured and theoretical calculation results of

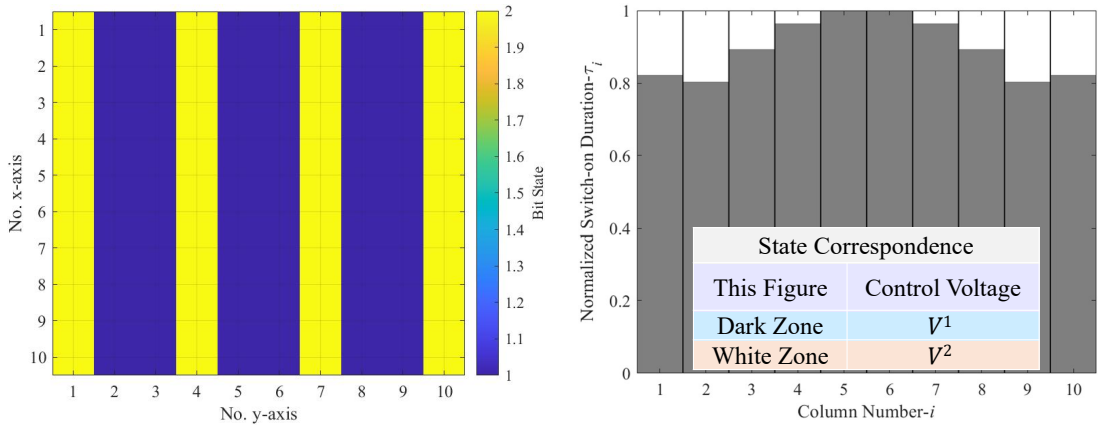

(a) (b)

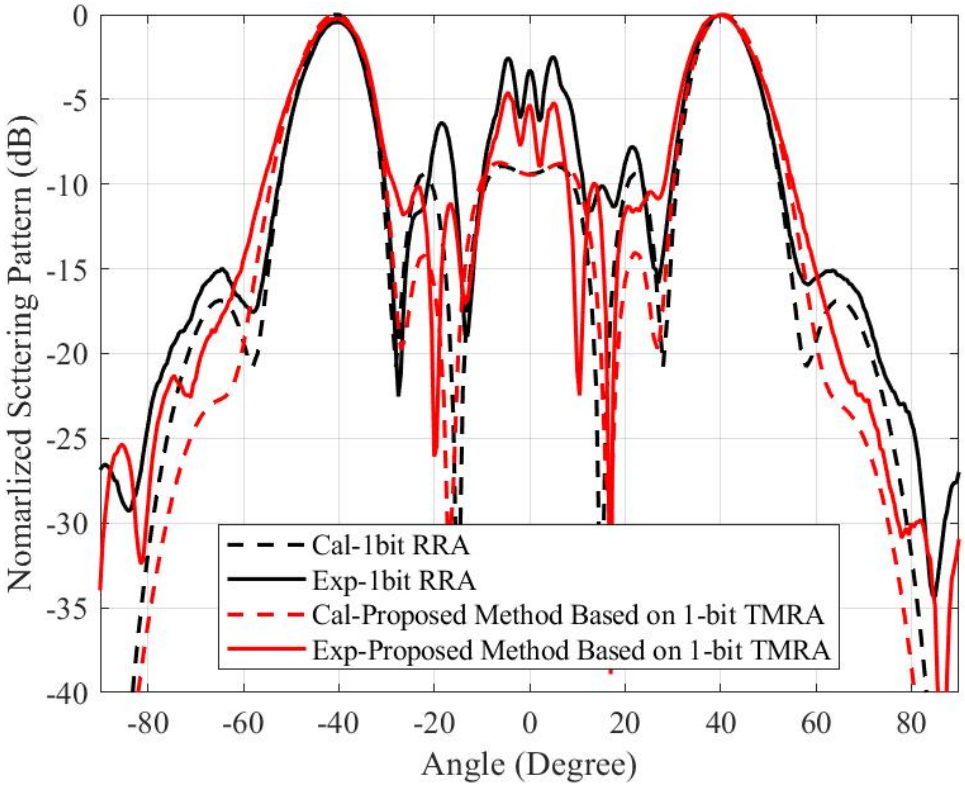

(c)

Figure 4.17: Experimental results for beam-forming of 20 dB Chebyshev pattern. (a) 1-bit distribution for beam-forming. (b) Switch-on duration (TM amplitude excitation) distribution for beam-forming. (c) Measured normalized scattering patterns

the beam-forming are shown in Fig 4.17(c). The black dashed line and the black solid line represent the theoretical and measured results of the 1-bit RRA, respectively. It should be noted that the results of the theoretical calculation are the total scattering pattern considering the element factor, and the element factor is described using the $\cos^{q_e}(\theta)$ model. q_e is calculated by fitting the results obtained from the full-wave simulation of the element structure.

As shown in Fig 4.17(c), it can be observed that the 40 ° beam steering is achieved while the grating-lobe appears at the symmetric mirror angle, which is caused by the 1-bit phase error. This is also supported by the center-symmetric 1-bit quantized phase distribution in the figure. Secondly, it can be found that the measured results agree well with the theoretical calculation, which verifies the effect of 1-bit RRA. The slightly larger SLLs observed are then due to imperfections in the experimental environment. The red dashed line and the red realization represent the theoretical calculations and the measured results of the proposed method based on 1-bit TMRA to achieve beam-forming, respectively. Firstly, it can be observed that the sub-flap level of 1-bit TMRA is suppressed to different degrees compared to 1-bit RRA, and the average measured reduction value is about 3 dB, which confirms the well performance of the proposed method in suppressing SLLs. Secondly, a comparison between the theoretical calculations and the measured results reveals a remarkable agreement, providing further evidence for the effectiveness of the proposed method. It should be noted that the large magnitude and drastic variation of the scattered field distribution observed in the range of plus and minus 10 degrees in the measured results are mainly due to the blockage of Tx. Specifically, within this range of tests, the overlapping of the Tx and Rx apertures leads to a proximity between them. As a result, the distribution of the TMRA scattered field over the Rx aperture is disrupted, and the obtained test results represent a combination of the TMRA scattered field and the Tx scattered field that are superimposed on each other. This overlapping effect introduces significant variations in the measured results and accounts for the large magnitude and drastic variation observed in the scattered field distribution within the range of plus and minus 10 degrees. Besides, the differences between the measured results and the theoretical calculation for the remaining angles mainly come from the imperfection of the measurement environment.

The time sequences required to achieve the 30 dB Chebyshev pattern and Binomial

pattern, as well as the corresponding test results, are presented in Fig. 4.18 and Fig. 4.19. It can be observed that the measured results exhibit a favorable low side-lobe characteristic, matching the theoretical calculation results. The close agreement between the measured and theoretical results confirms the effectiveness of the proposed method. It is important to note that achieving a Binomial pattern typically requires very low edge taper amplitudes, which can be challenging with conventional antennas that rely on attenuators with large dynamic range. The successful realization of the Binomial pattern in the actual measurements further demonstrates the flexible beam control capability enabled by temporal modulation techniques.

In addition, an analysis of loss (expressed in dB) and efficiency was conducted for the three experimentally validated beam-forming mentioned above. The results are presented in Table 4.1. Beam-forming loss refers to the difference between the theoretical calculated value of the directivity of the formed beam and the theoretical maximum directivity for the same aperture area. The theoretical calculated value of diode loss represents the time-averaged loss of all diodes in the array that are active during a time sequence period. The measured derived value of diode loss is obtained by subtracting the theoretical beam-forming loss from the measured total loss. It is important to note that the measured derived value is not a direct measured result on the diodes but is obtained through this calculation method using measured results, which should be clarified. Based on the results of the three experiments, the measured losses closely match the theoretical losses when considering the calculated values of diode losses, confirming the accuracy of the design. Furthermore, the measured derived values of diode losses closely match to their theoretical calculated values, validating the effectiveness of the proposed method for predicting diode losses using a theoretical approach. Additionally, the theoretical and measured values of TMRA efficiency were calculated based on the theoretical beam-forming losses and the measured total losses, respectively. It can be observed that the beam-forming losses for the 20 dB Chebyshev, 30 dB Chebyshev, and Binomial patterns increase progressively. This is due to the decreasing reflection coefficient required to form these beams, resulting in lower aperture efficiency. Since the theoretical value of TMRA efficiency is calculated without considering the diode losses, the disparity between the theoretical and measured values of TMRA efficiency can be attributed to the diode losses. It is worth emphasizing that the successful quantitative analysis of TMRA efficiency highlights the necessity and

Table 4.1: Loss Budget and Efficiency Analysis of Beam-Forming Experiments

Targets \ Loss Item		Beam-Forming	Diode	Total	$\eta_{f_0}^{TMRA}$
20 dB*	Cal.	6.24	2	8.24	23.7%
	Exp.	N/A	1.95	8.19	15.2%
30 dB*	Cal.	8.14	2.31	10.45	15.3%
	Exp.	N/A	1.56	9.70	10.7%
Bi*	Cal.	12.08	2.25	14.33	6.2%
	Exp.	N/A	1.6	13.68	4.3%

* 20 dB Chebyshev Pattern.

* 30 dB Chebyshev Pattern.

* Binomial Pattern.

value of the proposed analytical method for assessing TMRA efficiency.

To comprehensively evaluate the effectiveness of the proposed method, three additional sets of beam-forming verification experiments were conducted. In these experiments, the reflection angle of the scattered beam was adjusted to 30 degrees, while keeping the other parameters consistent with the previous three sets of experiments. The first experiment focused on evaluating the beam-steering ability using the 1-bit RRA. The corresponding 1-bit phase distribution and measured results are illustrated in Fig 4.20(a) and (b). It can be observed that the scattered beam is successfully deflected towards the 30 ° direction, and both the main beam and the surrounding region exhibit good agreement with the theoretical calculations. The higher measured SLLs at larger angular ranges, compared to the theoretical calculations, can mainly be attributed to interference factors present in the test environment. Fig 4.20(c), (d) and (e) presents the experimental results for the three different beam-formings. It can be observed that the measured scattering beams exhibit variations corresponding to the different design targets, and these results align well with the theoretical outcomes, thereby confirming the effectiveness of the proposed method. Furthermore, an analysis of loss and efficiency was performed and is presented in Table 4.2. Comparing this table with the previous one, it can be observed that the beam assignment at a 30° reflection angle achieves higher

Table 4.2: Loss Budget and Efficiency Analysis of Beam-Forming Experiments

Targets \ Loss Item		Beam-Forming	Diode	Total	$\eta_{f_0}^{TMRA}$
20 dB*	Cal.	5.44	2.23	7.67	28.6%
	Exp.	N/A	2.41	7.85	16.4%
30 dB*	Cal.	7.17	2.15	9.32	11.7%
	Exp.	N/A	2.02	9.19	12.1%
Bi*	Cal.	11.06	2.23	13.29	7.8%
	Exp.	N/A	1.67	12.73	5.3%

* 20 dB Chebyshev Pattern.

* 30 dB Chebyshev Pattern.

* Binomial Pattern.

efficiency. This can be attributed to the smaller pointing angle of the scattered beam compared to the previous three sets of experiments, as well as the larger projected area of the TMRA aperture in the direction of the scattered beam. As a result, the aperture loss is reduced, leading to improved efficiency.

4.7 Summary

In this chapter, a novel method for achieving enhanced-efficiency beam-forming with Time Modulated Reflectarray (TMRA) at the carrier frequency was proposed. By employing an anti-phase switching approach, the proposed method enables beam-forming at the carrier frequency using Q-bit Reflectarray (RRA). Theoretical analysis demonstrates that precise beam-forming can be achieved by selecting an appropriate bit number Q based on specific targets. Moreover, the TMRA efficiency of the proposed method is significantly higher than that of conventional TMRA operating at the first harmonic frequency.

To validate the effectiveness of the proposed method based on 1-bit TMRA, experiments were conducted using an available 1-bit RRA prototype. Despite the degradation caused by the large phase error resulting from 1-bit phase quantization, the proposed

method remains effective. The control mechanism for achieving beam-forming using 1-bit TMRA was detailed, with the introduction of four Binary Control Time Slot (BCTS) configurations to illustrate the control mechanism clearly. Additionally, a beam-forming control board was designed and fabricated.

A series of validation experiments were performed using 1-bit TMRA to realize beam steering at 30 and 40 degrees while shaping the beam to achieve 20 dB Chebyshev, 30 dB Chebyshev, and Binomial patterns. The experimental results demonstrate that the scattering patterns can be controlled as per the theoretical designs. TMRA efficiencies were evaluated using a proposed definition of TMRA efficiency to showcase the scattering performance of the proposed method based on 1-bit TMRA. These results validate the beam-forming capability of the proposed method, highlighting the achievement of simultaneous and independent control of reflected amplitude and phase.

The construction of BCTS and the establishment of correspondence between BCTS and their equivalent reflection coefficients enable beam-forming at the carrier frequency and make the design process more intuitive. Furthermore, by analyzing corresponding logic states and utilizing XNOR chips, the desired BCTS can be realized with a simple structure of the control board, reducing system complexity and cost.

It is important to note that the observed limitations in the actual beam-forming effect in the experimental results are primarily attributed to the phase error of 1-bit phase quantization rather than the proposed method itself. This issue can be addressed by employing TMRA with higher bit resolutions, which represents a potential direction for future research in this study.

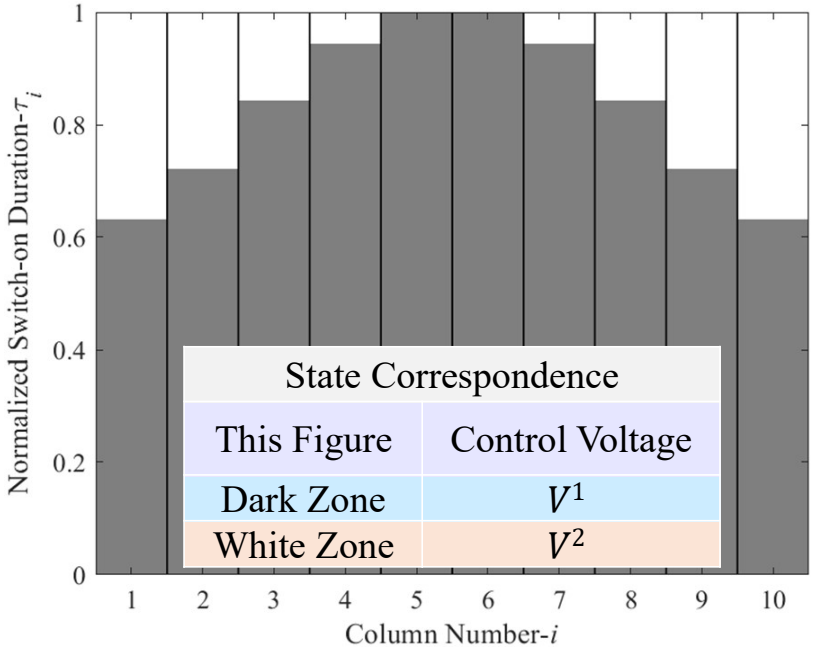

(a)

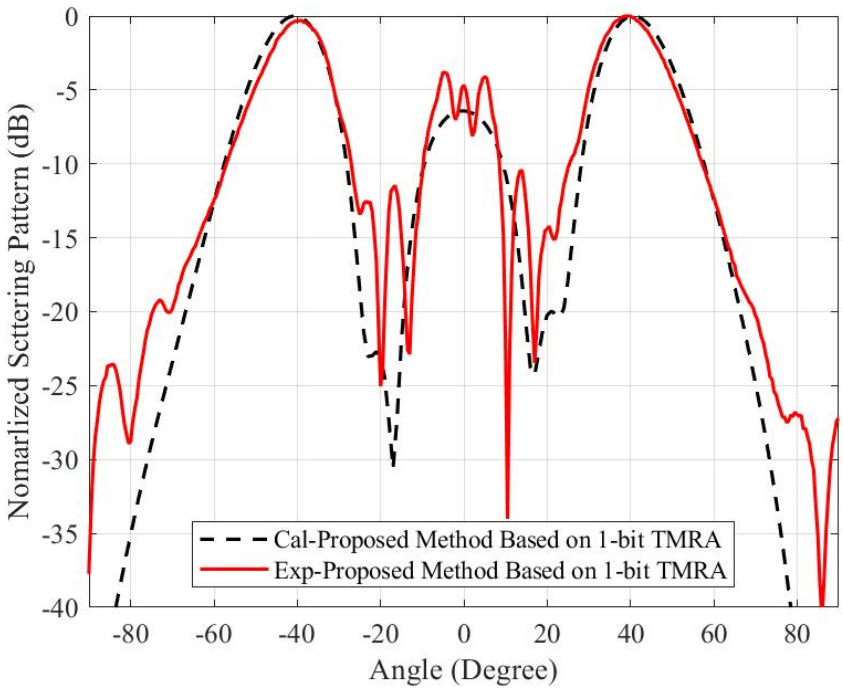

(b)

Figure 4.18: Experimental results for beam-forming of 30 dB Chebyshev pattern. (a) Switch-on duration distribution for beam-forming. (c) Measured normalized scattering patterns

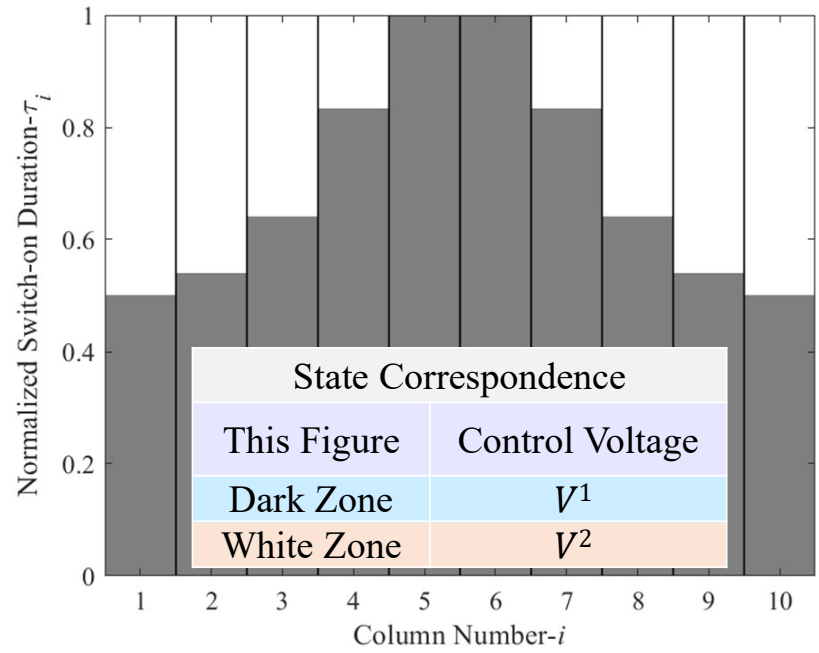

(a)

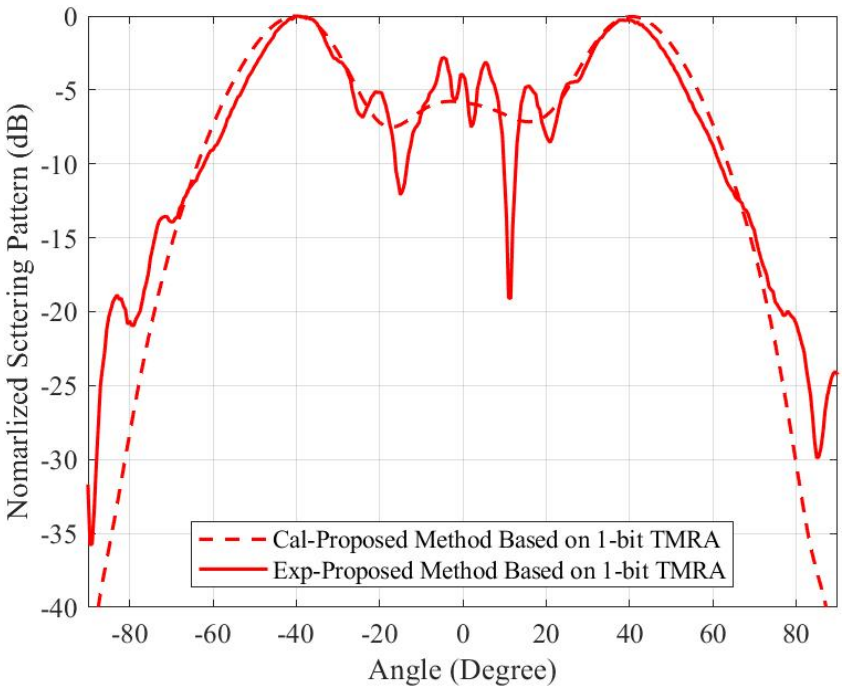

(b)

Figure 4.19: Experimental results for beam-forming of Binomial pattern. (a) Switch-on duration distribution for beam-forming. (c) Measured normalized scattering patterns

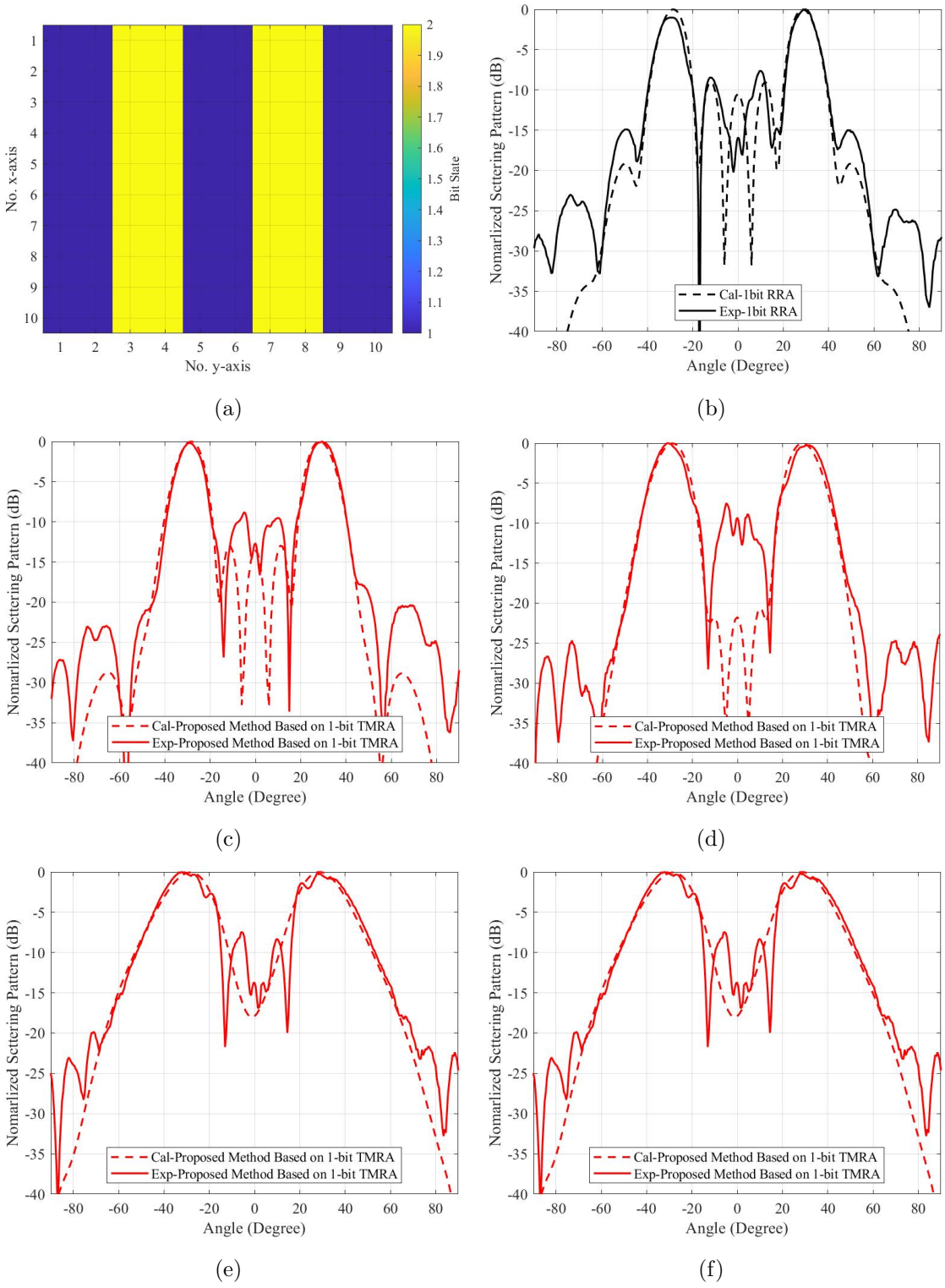

Figure 4.20: Experimental results for beam-forming at 30°. (a) 1-bit phase distribution. Measured normalized scattering patterns of (b) 1-bit RRA. (c) 20 dB Chebyshev pattern. (d) 30 dB Chebyshev pattern. (e) Binomial pattern.

Chapter 5

Summary

5.1 Conclusion

This dissertation aims to design, implement, and experimentally characterize a time-modulated reflectarray based on phase-reconfigurable reflectarray. The reflectarray possesses flexible beam control capabilities and can be applied in RIS applications. By introducing time modulation technology into the existing reflectarray structure, the reflectarray can control the reflection amplitude using different phase states, enabling flexible control of the scattered beam with low system complexity and cost-effectiveness. Furthermore, unlike traditional TMRAs, the proposed TMRA operates at the carrier frequency, making it compatible with existing communication systems and highly practical. Importantly, the flexible beam control capability of the proposed TMRA offers significant potential for assisting base stations in blind spot coverage, anti-interference communication, and intelligent sensing applications, which have been validated through simulations and measurements in this paper.

Chapter 1 provides a detailed introduction to various potential implementations of RIS at the hardware level, focusing on the perspective of physical scattering structures. It helps clarify the gap between recent research progress and the envisioned functionalities of RIS. The chapter highlights the latest advancements in RIS, such as TMRA based on reconfigurable reflectarray (RRA). It outlines the major classifications of RRAs, including phase-controllable RRAs (both electronically controlled and mechanically con-

trolled forms) and amplitude-controlled RRAs, and points out their limitations in meeting the diverse application requirements of RIS. The chapter emphasizes the principles and advantages of TMRA. Additionally, traditional TMRAs often operate at harmonic frequencies, resulting in lower scattering efficiency. Moreover, transitioning from the carrier frequency to the harmonic frequency poses a challenge for direct application in existing communication systems. The motivation for proposing a new TMRA structure operating at the carrier frequency is provided.

In Chapter 2, the working principles and design methods of TMAAs are elaborated, extending the concept of time modulation to reflectarray, referred to as TMRA. The implementation methods of TMRA are discussed, highlighting the differences between TMRA and TMAA. The analysis method and definition of TMRA efficiency are introduced for the first time, providing a useful quantitative approach for evaluating efficiency in the field of TMRA research, which is applied in the performance analysis sections of Chapter 3 and Chapter 4. Additionally, two fundamental applications of TMRA, namely beam-forming and environment sensing, are briefly introduced to emphasize its flexible beam control capability. Specifically, for the first time, a methodology for environmental sensing (e.g., DOA estimation and target localization) using the multi-harmonic properties of TMRA is discussed and its feasibility is theoretically analyzed. Furthermore, the rectangular waveguide method for measuring the reflection coefficients of individual elements is presented, offering a low-cost and rapid testing approach for designing large-scale and cost-effective RRA with active components. Additionally, a series of experiments are conducted to verify the on-off characteristics and switching speed of the diodes used, as well as the accuracy of simulation modeling, which is crucial for ensuring the consistency between the final implementation and the theoretical design of TMRA.

In Chapter 3, inspired by the concept of 1-bit RRA, a 1-bit time-modulated reflectarray (1-bit TMRA) is designed to achieve controllable reflection amplitudes using two phase-reversed reflection states. This new configuration of 1-bit TMRA offers switchable reflection phases or amplitudes control capacity, making it versatile for various communication scenarios. It also exhibits advantages such as low system complexity, ease of design, and seamless integration with existing communication systems. Compared to traditional RRAs, the proposed 1-bit TMRA has the ability to control reflection amplitudes. In contrast to conventional TMRA, the proposed 1-bit TMRA can control phase

at the carrier frequency. The design and fabrication of the 1-bit TMRA prototype, 1-bit function control board, and time modulation function control board are described. The switchable phase or amplitude control abilities are successfully verified by realizing beam-steering and beam-shaping, respectively, when 1-bit TMRA works as 1-bit state and time modulation state. In addition to measuring the scattering radiation patterns, the scattering characteristics of TMRA are discussed in detail, including gain bandwidth and SLL bandwidth, providing design guidance for TMRA applications. Furthermore, by measuring the scattering radiation patterns at different time-modulation frequencies, it is demonstrated that the scattering characteristics of TMRA remain unchanged with the variation of time-modulation frequency. These conclusions are important for a comprehensive analysis of TMRA's scattering properties and its applicable applications.

In Chapter 4, a method is proposed to enable TMRA with simultaneous independent control of both amplitude and phase, allowing for efficient beam-forming at the carrier frequency. This addresses the limitation of the previous chapter where TMRA could not control both amplitude and phase simultaneously. The scattering field equations of TMRA are reanalyzed, revealing the theoretical basis for simultaneous control of amplitude and phase, which is achieved through the independent control of RRA control signals and time modulation control signals. A phase inversion switching method is proposed to control the switching mode between different phase states of Q-bit RRA, enabling control of the reflection amplitude. The theoretical analysis of TMRA implementation using Q-bit RRA shows that selecting an appropriate number of phase quantization bits (Q) can achieve good beam-forming performance. The proposed method outperforms traditional TMRA operating at harmonic frequencies in terms of directivity and efficiency, demonstrating the enhanced efficiency characteristics. However, it is observed that using a lower number of phase quantization bits introduces larger phase errors, which degrade the beam-forming performance. It should be noted that this is due to the phase errors introduced by Q-bit phase quantization and not a limitation of the proposed method. A series of experiments is conducted using the 1-bit RRA-based TMRA. Theoretical calculations and measurement results exhibit good consistency, demonstrating the ability of the proposed method to achieve beam-forming as expected in theory and validating its simultaneous independent control of reflection amplitude and phase. Loss and efficiency analysis are also performed to objectively assess the radiation performance of

the experimentally validated 1-bit TMRA. Importantly, the realized scattering radiation patterns and efficiency can be further improved by using RRAs with more bits, providing better scattering characteristics. The proposed implementation method of TMRA can serve as a potential alternative design for developing multifunctional, low-cost, and easily manufacturable reflectarray for RIS applications.

In conclusion, this paper analyzes and addresses the challenge of designing TMRA with simultaneous independent control of reflection amplitude and phase. The proposed TMRA operates at the carrier frequency and achieves flexible control of the reflected beam with lower system complexity and cost by introducing time-modulation technology into existing RRA systems. This significantly promotes performance enhancement and functionality expansion in the field of TMRA.

5.2 Future Work

The main focus of this dissertation was on the concept and description of the design of TMRAs based on the RRA structure and operating at the carrier frequency, as well as its functionality for realizing flexible beam control (i.e., beam-forming). The outcomes and results suggest the TMRAs are in their initial stage and future investigations need to be carried out to further explore and improve their performance and functionality.

1. Complete loss analysis and harmonic suppression of TMRA. The loss of traditional RRA includes metal loss, dielectric loss, active component loss, bias circuit loss, etc. TMRA introduces time modulation on top of this, which leads to the generation of harmonic components (also called side-bands), which means that a part of the energy losses among the harmonic components. A complete analytical method should be proposed to comprehensively analyze the losses due to each factor so that the scattering performance of TMRA can be objectively evaluated. In addition, for TMRA using carrier frequency for beam-forming, the side-band level should be suppressed as much as possible so that the energy is concentrated at the carrier frequency while the interference to the adjacent frequency bands is reduced. This aspect can be achieved from optimizing the time sequence and adding filter structures in hardware, the former has been reported in TMAA-related studies, but not applied to reduce the side-band level scattering of TMRA. The latter has nor been reported yet. Research in this area is important to

broaden the application scenarios of TMRA.

2. Analyze the methodology and experimental validation of environment sensing using TMRA based on the receiver-side scattering characteristics. Although there have been some works on DOA estimation using TMRA [53,54], these works neglect the physical scattering characteristics under different time sequence, resulting in low scattering intensity at the receiver end, which affects the estimation accuracy. In the Section 2.4.2 of this dissertation, the feasibility of using the multi-harmonic properties of the scanning time sequence for environment sensing is theoretically analyzed, but more in-depth research is lacking, such as examining the variation of the scattering beam-width with the pointing angle and analyzing the theoretical resolution limit. It should be investigated in future work to derive the relationship between the signal at the receiving end and the DOA or target direction, and experimentally verified.

3. Design of TMRA with higher bit phase states. In Chapter 4, we proposed a method for beam-forming based on Q-bit TMRA, which has higher efficiency compared to the conventional TMRAs, and the performance improves with the increase of the number of quantized phase states. These features are verified in the theoretical calculations based on 4-bit TMRA. However, limited by the experimental conditions, only the 1-bit TMRA verifies that the measured and theoretically predicted results coincide with each other, and fails to realize the perfect beam-forming effect. Therefore, TMRAs with higher bit phase states should be designed in future work to achieve better beam-forming and efficiency, which is very important to promote the practicalization of TMRAs. At present, there are cases of 2-bit RRA implementation [19, 20], but how to simply and quickly control its switching in multiple phase states still poses a big challenge.

4. Conduct research on TMRA applications. The current research on TMRA mainly focuses on making it capable of flexible beam control, while less research has been done on specific applications. Attempts should be made to explore its feasibility in multi-application scenarios such as radar, communication, environment sensing, imaging, etc. In addition, it is also valuable to actually use TMRA to transmit modulated signals in communication applications, and to evaluate the performance of TMRA applied to communication systems.

5. Carry out research on time modulation devices with high switching speed, low loss, and small size. The switching speed determines the bandwidth of the TMRA transmission

signal, and the loss affects the strength of the TMRA transmission signal. At present, the mainstream PIN diode structure is simple, easy to control, but the cost is high, and will produce nonlinear harmonic components; liquid crystal through mass production has the cost advantage, and it is linear device, but the switching speed is slower and the loss is larger; MEMS has the advantage of low loss and high linearity, but its switching rate is slow and requires a higher driving voltage. Therefore, going for the exploration of new and suitable time modulation devices for TMRA applications will be a crucial step towards the solution of the practical application problems of TMRA.

Acknowledgments

As the pen reaches this point, my thesis is about to draw to a close, marking the end of my doctoral journey that has lasted for four years. I thought this moment would be filled with overwhelming excitement, but unexpectedly, it is rather calm, just like the serene summer night outside the window of Mount Yagi and the cool breeze brushing through Sakuragi Street at this moment. I turn my head to look outside, and the pitch-black sky resembles a screen, projecting every frame of the past four years and the corresponding changes in the seasons: experiments failing like a raging blizzard, research ideas blooming like all things in nature, progress advancing like scorching heat, and the acceptance of my papers bringing abundance like a harvest. Through this cycle of changing seasons, I have gradually matured and grown from stumbling to walking with steady steps. Finally, it's about to come to an end here. As I look back on this journey, I realize there have been so many people who have been continuously helping and supporting me. They have either sheltered me from the storm, guided me with their light, provided me with fuel for my fire, or cheered me on and encouraged me. They deserve my sincerest gratitude.

First and foremost, I would like to express my special gratitude to Professor Qiang Chen. Without your consent to accept me as a Ph.D. candidate, the trajectory of my life might have taken a different turn. Your solid theoretical knowledge has always benefited me greatly, your keen insight has often provided me with fresh perspectives, and your strict guidance has allowed me to grow rapidly. You not only imparting your knowledge and wisdom in studies and research, but also providing me with comprehensive care in my daily life, teaching me the principles of being meticulous in work and conscientious in character. The four years of studying under your guidance have undoubtedly been a precious treasure in my life, and they will undoubtedly influence my entire life.

I would like to thank Prof. Noriharu Suematsu, Prof. Hideo Fujikake, and associate

Prof. Keisuke Konno for their valuable feedback and comments about my dissertation.

I want to thank assistant Prof. Hiroyasu Sato and associate Prof. Keisuke Konno for their assistance with experimental equipments and sharing research experiences. Special thanks to assistant Prof. Sato for providing the APFA antenna as a feed source for my experiments. It is your generous help that has allowed my research and experiments to progress smoothly. I also want to express my gratitude to Prof. Kaida Xu. Your immense help in thesis writing and responding to reviewers' comments has been invaluable, and your encouragement has supported me to bravely face the paper rejections without giving up. Thank you, Prof. Yongliang Zhang, for treating me like a younger brother and for your care and encouragement. Thanks to Associate Prof. Daotong Li and Associate Prof. Wei Luo, I have learned knowledge far beyond the scope of research from you. In addition, I want to express my gratitude to secretary Yumiko Ito, your diligent and selfless work has helped me solve countless problems, and the conversations with you in our free time have allowed me to gain a deeper understanding of Japan.

Continuing on, I want to express my gratitude to the members of the Chen-Konno laboratory. Special thanks to Dr. Sirao Wu and Dr. Junyi Xu, your companionship in personal life has been a vital source of energy for me. May our friendship remain as eternal as the footprints we left together in various places across Japan. Thanks to Dr. Wen Wu, your rich research experience and optimistic and positive work attitude have always been beneficial to me. Thanks to Dr. Wenyi Shao, Dr. Xiaotong Li and Dr. Ao Hu, your constructive discussions have always inspired me to think more deeply. Thanks to Dr. Yue Cui and Dr. Ke Peng, our friendship continues in Sendai, bringing warmth and vitality to my life. Thanks to Dr. Kevin Mutai, for your selfless encouragement and thought-provoking discussions that have often sparked new ideas. Thanks to Dr. Chang Ge, Dr. Sijie Xia, Dr. Xiaolian Mao, Yuhao Shang, and Jialu Wang, your companionship has made life in the lab vibrant and colorful. Thanks to the rest of the members of the Chen-Konno laboratory, your help has helped me adapt better to life in Japan.

I want to extend special thanks to my bosom friend, Dr. Ziye Liu. Time and distance have not affected our friendship, instead, our similar growth stages have brought us closer together. Your support, encouragement, and care have repeatedly brought me back on track when I felt lost. May we always retain our innocent heart of a child and become the people we aspire to be. Thanks to Zhen Du, Sifan Xiao, and Dr. Xinyue Fu, your

unwavering companionship has given me courage and strength. Thanks to Dr. Jiacheng Li and Dr. Yixuan Zhang, our research discussions have always been rewarding, and I appreciate your selfless sharing. Thanks to Linhan Li, for co-founding OrientWagon with me. The satisfaction it brought was second only to publishing papers. Engaging in road trips with you and other wagon car enthusiasts has been the greatest source of joy during my journey.

I also express my deepest gratitude to my parents. It is your selfless dedication that enabled me to pursue my studies abroad. Your trust in me provided boundless strength when facing setbacks, and your unconditional love and encouragement allowed me to wholeheartedly immerse myself in my research. Yet, in front of you, I feel guilty. I have often neglected your delicate emotional needs and lacked the companionship by your side. As I approach my 30s, I find myself still seeking from you all instead of giving back. I can hardly imagine if I could ever repay even one percent of what you've given me. I promise to use every day in the future to care for and support you, fulfilling my duty as your child. You've worked so hard, I love you! I also want to thank my in-laws. Your trust, encouragement, and care have given me additional love and have provided me with more courage and strength.

I would like to express my heartfelt gratitude to my beloved wife, Dr. Ruolin Fu, for everything she has done. From our time as Master's students to pursuing our doctoral degrees together from Xi'an to Sendai, your love transcends time and space, always by my side. Your gentle nature hides immense courage; you bravely joined me in pursuing our doctoral degrees in Japan. Though you were the cherished child of your parents, you take care of me in every way, surrounding me with your love every day. Despite your petite appearance, you have the strength to embrace me entirely, helping me regroup in the warmth of our home during moments of disappointment and frustration. Your presence gives me boundless courage to face any obstacles and continue forward. In these years of pursuing our doctoral degrees together, aside from basking in your kindness and optimism, I am also delighted to witness your growing confidence, perseverance, and bravery. Growing together with you is the most romantic thing, and I eagerly look forward to every day we walk hand in hand in the future. Be it to the ends of the earth or through the mundane days, I will love you as wholeheartedly as you unhesitatingly love me.

Also, I would like to express my heartfelt gratitude to the Program on Open Innovation Platform with Enterprises, Research Institute and Academia, Japan Science and Technology Agency (JST, OPERA) under Grant JPMJOP1852. In addition, I would like to extend my appreciation to the Tohoku University's Advanced Graduate School Pioneering Research Support Project for the 1-year scholarship and proofreading fees for the two journal papers. Without their generous assistance, I may not have been able to successfully complete my doctoral program.

Finally, I want to thank myself for persisting through setbacks, growing stronger with each “battle”. And this version of myself is formed by the support and help from all of you.

Bibliography

[1] T. Nakamura, "5g evolution and 6g," in *2020 IEEE symposium on VLSI technology*, pp. 1–5, IEEE, 2020.

[2] R. T. Alliance, "Reconfigurable intelligent surface technology white paper," 2023.

[3] Y.-C. Liang, R. Long, Q. Zhang, J. Chen, H. V. Cheng, and H. Guo, "Large intelligent surface/antennas (lisa): Making reflective radios smart," *Journal of Communications and Information Networks*, vol. 4, no. 2, pp. 40–50, 2019.

[4] E. Basar, M. Di Renzo, J. De Rosny, M. Debbah, M.-S. Alouini, and R. Zhang, "Wireless communications through reconfigurable intelligent surfaces," *IEEE access*, vol. 7, pp. 116753–116773, 2019.

[5] M. Di Renzo, A. Zappone, M. Debbah, M.-S. Alouini, C. Yuen, J. De Rosny, and S. Tretyakov, "Smart radio environments empowered by reconfigurable intelligent surfaces: How it works, state of research, and the road ahead," *IEEE journal on selected areas in communications*, vol. 38, no. 11, pp. 2450–2525, 2020.

[6] L. Dai, B. Wang, M. Wang, X. Yang, J. Tan, S. Bi, S. Xu, F. Yang, Z. Chen, M. Di Renzo, *et al.*, "Reconfigurable intelligent surface-based wireless communications: Antenna design, prototyping, and experimental results," *IEEE access*, vol. 8, pp. 45913–45923, 2020.

[7] W. Tang, M. Z. Chen, X. Chen, J. Y. Dai, Y. Han, M. Di Renzo, Y. Zeng, S. Jin, Q. Cheng, and T. J. Cui, "Wireless communications with reconfigurable intelligent surface: Path loss modeling and experimental measurement," *IEEE Transactions on Wireless Communications*, vol. 20, no. 1, pp. 421–439, 2020.

[8] Y. Liu, X. Liu, X. Mu, T. Hou, J. Xu, M. Di Renzo, and N. Al-Dhahir, "Reconfigurable intelligent surfaces: Principles and opportunities," *IEEE communications surveys & tutorials*, vol. 23, no. 3, pp. 1546–1577, 2021.

[9] H. Yang, F. Yang, S. Xu, Y. Mao, M. Li, X. Cao, and J. Gao, "A 1-bit 10×10 reconfigurable reflectarray antenna: Design, optimization, and experiment," *IEEE Transactions on Antennas and Propagation*, vol. 64, no. 6, pp. 2246–2254, 2016.

[10] J. C. Liang, Q. Cheng, Y. Gao, C. Xiao, S. Gao, L. Zhang, S. Jin, and T. J. Cui, "An angle-insensitive 3-bit reconfigurable intelligent surface," *IEEE Transactions on Antennas and Propagation*, vol. 70, no. 10, pp. 8798–8808, 2021.

[11] P. Aghabeyki, Y. Cai, G. Deng, Z.-H. Tan, and S. Zhang, "A dual-polarized reconfigurable reflectarray with a thin liquid crystal layer and 2-d beam scanning," *IEEE Transactions on Antennas and Propagation*, vol. 71, no. 4, pp. 3282–3293, 2023.

[12] B. Rana, S.-S. Cho, and I.-P. Hong, "Review paper on hardware of reconfigurable intelligent surfaces," *IEEE Access*, 2023.

[13] H. Kamoda, T. Iwasaki, J. Tsumochi, T. Kuki, and O. Hashimoto, "60-ghz electronically reconfigurable large reflectarray using single-bit phase shifters," *IEEE transactions on antennas and propagation*, vol. 59, no. 7, pp. 2524–2531, 2011.

[14] E. Carrasco, M. Barba, and J. A. Encinar, "X-band reflectarray antenna with switching-beam using pin diodes and gathered elements," *IEEE Transactions on Antennas and Propagation*, vol. 60, no. 12, pp. 5700–5708, 2012.

[15] H. Yang, X. Cao, F. Yang, J. Gao, S. Xu, M. Li, X. Chen, Y. Zhao, Y. Zheng, and S. Li, "A programmable metasurface with dynamic polarization, scattering and focusing control," *Scientific reports*, vol. 6, no. 1, p. 35692, 2016.

[16] M.-T. Zhang, S. Gao, Y.-C. Jiao, J.-X. Wan, B.-N. Tian, C.-B. Wu, and A.-J. Farrall, "Design of novel reconfigurable reflectarrays with single-bit phase resolution for ku-band satellite antenna applications," *IEEE Transactions on Antennas and Propagation*, vol. 64, no. 5, pp. 1634–1641, 2016.

[17] H. Zhang, X. Chen, Z. Wang, Y. Ge, and J. Pu, "A 1-bit electronically reconfigurable reflectarray antenna in x band," *IEEE Access*, vol. 7, pp. 66567–66575, 2019.

[18] X. Pan, F. Yang, S. Xu, and M. Li, "A 10 240-element reconfigurable reflectarray with fast steerable monopulse patterns," *IEEE Transactions on Antennas and Propagation*, vol. 69, no. 1, pp. 173–181, 2020.

[19] X. Ma, J. Han, T. Wang, S. Chen, Y. Mu, H. Liu, and L. Li, "Design and rectangular waveguide validation of 2-bit wideband reconfigurable reflective metasurface element in x-band," *IEEE Antennas and Wireless Propagation Letters*, vol. 22, no. 1, pp. 4–8, 2022.

[20] L. Dai, B. Wang, M. Wang, X. Yang, J. Tan, S. Bi, S. Xu, F. Yang, Z. Chen, M. Di Renzo, *et al.*, "Reconfigurable intelligent surface-based wireless communications: Antenna design, prototyping, and experimental results," *IEEE access*, vol. 8, pp. 45913–45923, 2020.

[21] Q. Zhang, M. Zhang, X. Shi, S. Gao, Q. Luo, L. Chen, J. Wan, and X. Wang, "A low-profile beam-steering reflectarray with integrated leaky-wave feed and 2-bit phase resolution for ka-band satcom," *IEEE Transactions on Antennas and Propagation*, vol. 70, no. 3, pp. 1884–1894, 2022.

[22] J. Wang, V. Manohar, and Y. Rahmat-Samii, "Beam steerable reflectarray enabling cubesat internet of space: Conceptualization and design," in *2020 14th European Conference on Antennas and Propagation (EuCAP)*, pp. 1–4, IEEE, 2020.

[23] S. Hum, M. Okoniewski, and R. Davies, "Realizing an electronically tunable reflectarray using varactor diode-tuned elements," *IEEE Microwave and Wireless Components Letters*, vol. 15, no. 6, pp. 422–424, 2005.

[24] F. Venneri, S. Costanzo, and G. Di Massa, "Design and validation of a reconfigurable single varactor-tuned reflectarray," *IEEE Transactions on Antennas and Propagation*, vol. 61, no. 2, pp. 635–645, 2013.

[25] S. Costanzo, F. Venneri, A. Raffo, G. Di Massa, and P. Corsonello, "Radial-shaped single varactor-tuned phasing line for active reflectarrays," *IEEE Transactions on Antennas and Propagation*, vol. 64, no. 7, pp. 3254–3259, 2016.

[26] M. E. Trampler, R. E. Lovato, and X. Gong, "Dual-resonance continuously beam-scanning x-band reflectarray antenna," *IEEE Transactions on Antennas and Propagation*, vol. 68, no. 8, pp. 6080–6087, 2020.

[27] A. Sayanskiy, A. Belov, R. Yafasov, A. Lyulyakin, A. Sherstobitov, S. Glybovski, and V. Lyashev, "A 2d-programmable and scalable reconfigurable intelligent surface remotely controlled via digital infrared code," *IEEE Transactions on Antennas and Propagation*, vol. 71, no. 1, pp. 570–580, 2023.

[28] L. Cai, Z. H. Jiang, and W. Hong, "Evaluation of reconfigurable reflectarray antenna element at 19 ghz based on highly anisotropic liquid crystal material," in *2019 IEEE International Conference on Computational Electromagnetics (ICCEM)*, pp. 1–3, IEEE, 2019.

[29] X. Li, H. Sato, Y. Shibata, T. Ishinabe, H. Fujikake, and Q. Chen, "Development of beam steerable reflectarray with liquid crystal for both e-plane and h-plane," *IEEE Access*, vol. 10, pp. 26177–26185, 2022.

[30] W. Zhang, Y. Li, and Z. Zhang, "A reconfigurable reflectarray antenna with an 8 μm-thick layer of liquid crystal," *IEEE Transactions on Antennas and Propagation*, vol. 70, no. 4, pp. 2770–2778, 2022.

[31] R. Guirado, G. Perez-Palomino, M. Ferreras, E. Carrasco, and M. Caño-García, "Dynamic modeling of liquid crystal-based metasurfaces and its application to reducing reconfigurability times," *IEEE Transactions on Antennas and Propagation*, vol. 70, no. 12, pp. 11847–11857, 2022.

[32] P. Aghabeyki, Y. Cai, G. Deng, Z.-H. Tan, and S. Zhang, "A dual-polarized reconfigurable reflectarray with a thin liquid crystal layer and 2-d beam scanning," *IEEE Transactions on Antennas and Propagation*, vol. 71, no. 4, pp. 3282–3293, 2023.

[33] D. E. Serup, G. F. Pedersen, and S. Zhang, "Electromagnetically controlled beam-steerable reflectarray antenna," *IEEE Transactions on Antennas and Propagation*, vol. 71, no. 5, pp. 4570–4575, 2023.

[34] X. Yang, S. Xu, F. Yang, M. Li, Y. Hou, S. Jiang, and L. Liu, "A broadband high-efficiency reconfigurable reflectarray antenna using mechanically rotational elements," *IEEE Transactions on Antennas and Propagation*, vol. 65, no. 8, pp. 3959–3966, 2017.

[35] X. Yang, S. Xu, F. Yang, M. Li, H. Fang, Y. Hou, S. Jiang, and L. Liu, "A mechanically reconfigurable reflectarray with slotted patches of tunable height," *IEEE Antennas and Wireless Propagation Letters*, vol. 17, no. 4, pp. 555–558, 2018.

[36] Z. Cao, Y. Li, Z. Zhang, and M. F. Iskander, "Single motor-controlled mechanically reconfigurable reflectarray," *IEEE Transactions on Antennas and Propagation*, vol. 71, no. 1, pp. 190–199, 2022.

[37] P. Mei, S. Zhang, and G. F. Pedersen, "A low-cost, high-efficiency and full-metal reflectarray antenna with mechanically 2-d beam-steerable capabilities for 5g applications," *IEEE Transactions on Antennas and Propagation*, vol. 68, no. 10, pp. 6997–7006, 2020.

[38] S. Bi, L. Xu, X. Cheng, Y. Sun, Q. Zhang, and C. Yuan, "An all-metal, simple-structured reflectarray antenna with 2-d beam-steerable capability," *IEEE Antennas and Wireless Propagation Letters*, vol. 22, no. 1, pp. 129–133, 2022.

[39] G.-B. Wu, Y.-S. Zeng, K. F. Chan, B.-J. Chen, S.-W. Qu, and C. H. Chan, "High-gain filtering reflectarray antenna for millimeter-wave applications," *IEEE Transactions on Antennas and Propagation*, vol. 68, no. 2, pp. 805–812, 2019.

[40] J. Zhu, Y. Yang, D. Mcgloin, S. Liao, and Q. Xue, "3-d printed all-dielectric dual-band broadband reflectarray with a large frequency ratio," *IEEE Transactions on Antennas and Propagation*, vol. 69, no. 10, pp. 7035–7040, 2021.

[41] H. Yang, X. Chen, F. Yang, S. Xu, X. Cao, M. Li, and J. Gao, "Design of resistor-loaded reflectarray elements for both amplitude and phase control," *IEEE Antennas and Wireless Propagation Letters*, vol. 16, pp. 1159–1162, 2016.

[42] H.-P. Li, G.-M. Wang, T. Cai, J.-G. Liang, and X.-J. Gao, "Phase-and amplitude-control metasurfaces for antenna main-lobe and sidelobe manipulations," *IEEE Transactions on Antennas and Propagation*, vol. 66, no. 10, pp. 5121–5129, 2018.

[43] J. Y. Dai, J. Zhao, Q. Cheng, and T. J. Cui, "Independent control of harmonic amplitudes and phases via a time-domain digital coding metasurface," *Light: Science & Applications*, vol. 7, no. 1, p. 90, 2018.

[44] Y. Wang and A. Tennant, "Experimental time-modulated reflector array," *IEEE Transactions on Antennas and Propagation*, vol. 62, no. 12, pp. 6533–6536, 2014.

[45] L. Zhang, X. Q. Chen, S. Liu, Q. Zhang, J. Zhao, J. Y. Dai, G. D. Bai, X. Wan, Q. Cheng, G. Castaldi, *et al.*, "Space-time-coding digital metasurfaces," *Nature communications*, vol. 9, no. 1, p. 4334, 2018.

[46] J. Zhao, X. Yang, J. Y. Dai, Q. Cheng, X. Li, N. H. Qi, J. C. Ke, G. D. Bai, S. Liu, S. Jin, *et al.*, "Programmable time-domain digital-coding metasurface for non-linear harmonic manipulation and new wireless communication systems," *National science review*, vol. 6, no. 2, pp. 231–238, 2019.

[47] L. Zhang, Z. X. Wang, R. W. Shao, J. L. Shen, X. Q. Chen, X. Wan, Q. Cheng, and T. J. Cui, "Dynamically realizing arbitrary multi-bit programmable phases using a 2-bit time-domain coding metasurface," *IEEE Transactions on Antennas and Propagation*, vol. 68, no. 4, pp. 2984–2992, 2019.

[48] X. Fang, M. Li, D. Ding, F. Bilotti, and R. Chen, "Design of in-phase and quadrature two paths space-time-modulated metasurfaces," *IEEE Transactions on Antennas and Propagation*, vol. 70, no. 7, pp. 5563–5573, 2022.

[49] X. G. Zhang, Y. L. Sun, B. Zhu, W. X. Jiang, Z. Zhang, and T. J. Cui, "Light-controllable time-domain digital coding metasurfaces," *Advanced Photonics*, vol. 4, no. 2, pp. 025001–025001, 2022.

[50] C. A. Balanis, *Antenna theory: analysis and design*. John wiley & sons, 2016.

[51] P. Nayeri, F. Yang, and A. Z. Elsherbeni, "Reflectarray antennas: theory, designs, and applications," 2018.

[52] E. F. Knott, J. F. Schaeffer, and M. T. Tulley, *Radar cross section*. SciTech Publishing, 2004.

[53] X. Fang, M. Li, J. Han, D. Ramaccia, A. Toscano, F. Bilotti, and D. Ding, "Accurate direction–of–arrival estimation method based on space–time modulated metasurface," *IEEE Transactions on Antennas and Propagation*, vol. 70, no. 11, pp. 10951–10964, 2022.

[54] J. Y. Dai, W. Tang, M. Wang, M. Z. Chen, Q. Cheng, S. Jin, T. J. Cui, and C. H. Chan, "Simultaneous in situ direction finding and field manipulation based on space-time-coding digital metasurface," *IEEE Transactions on Antennas and Propagation*, vol. 70, no. 6, pp. 4774–4783, 2022.

[55] J. Zhao, X. Yang, J. Y. Dai, Q. Cheng, X. Li, N. H. Qi, J. C. Ke, G. D. Bai, S. Liu, S. Jin, *et al.*, "Programmable time-domain digital-coding metasurface for non-linear harmonic manipulation and new wireless communication systems," *National science review*, vol. 6, no. 2, pp. 231–238, 2019.

[56] J. Y. Dai, W. Tang, L. X. Yang, X. Li, M. Z. Chen, J. C. Ke, Q. Cheng, S. Jin, and T. J. Cui, "Realization of multi-modulation schemes for wireless communication by time-domain digital coding metasurface," *IEEE transactions on antennas and propagation*, vol. 68, no. 3, pp. 1618–1627, 2019.

[57] M. Gholami and M. Neshat, "A direct antenna modulator with beam steering capability based on space-time-coding arrays," *IEEE Transactions on Antennas and Propagation*, vol. 70, no. 10, pp. 9282–9291, 2022.

[58] D. Ramaccia, D. L. Sounas, A. Alu, A. Toscano, and F. Bilotti, "Phase-induced frequency conversion and doppler effect with time-modulated metasurfaces," *IEEE Transactions on Antennas and Propagation*, vol. 68, no. 3, pp. 1607–1617, 2019.

[59] M. Saikia and K. V. Srivastava, "A time-modulated polarization-rotating frequency-selective surface," *IEEE Transactions on Antennas and Propagation*, vol. 71, no. 2, pp. 1506–1515, 2022.

[60] V. Kozlov, D. Vovchuk, and P. Ginzburg, "Radar range deception with time-modulated scatterers," *IEEE Transactions on Antennas and Propagation*, 2023.

[61] X. Wang and C. Caloz, "Spread-spectrum selective camouflaging based on time-modulated metasurface," *IEEE Transactions on Antennas and Propagation*, vol. 69, no. 1, pp. 286–295, 2020.

[62] J. Wang, D. Feng, Z. Xu, Q. Wu, and W. Hu, "Time-domain digital-coding active frequency selective surface absorber/reflector and its imaging characteristics," *IEEE Transactions on Antennas and Propagation*, vol. 69, no. 6, pp. 3322–3331, 2020.

[63] J. Wang, D. Feng, Y. Kong, S. Quan, and S. Xing, "Imaging properties of nonperiodic time-varying active frequency selective surface," *IEEE Transactions on Antennas and Propagation*, vol. 70, no. 7, pp. 5884–5891, 2022.

[64] P. Hannan and M. Balfour, "Simulation of a phased-array antenna in waveguide," *IEEE transactions on Antennas and Propagation*, vol. 13, no. 3, pp. 342–353, 1965.

[65] X.-N. Wang, L.-W. Yang, T.-H. Lee, J.-K. Su, B. Zhu, and X.-F. Yao, "Rf modeling of integrated rf cmos schottky diodes for rectifier designs," in *2008 9th International Conference on Solid-State and Integrated-Circuit Technology*, pp. 305–308, IEEE, 2008.

[66] C. Xu, P. Yu, and Y. Jiang, "A macro model of rf schottky diode in 22-nm cmos and its application," *Solid-State Electronics*, vol. 154, pp. 7–11, 2019.

[67] W. Zhang, Y. Tang, D. Wang, and Y. Wang, "A novel empirical model for cmos schottky diodes up to 67 ghz," *IEEE Transactions on Electron Devices*, vol. 66, no. 11, pp. 4660–4665, 2019.

[68] S. V. Hum and J. Perruisseau-Carrier, "Reconfigurable reflectarrays and array lenses for dynamic antenna beam control: A review," *IEEE transactions on antennas and propagation*, vol. 62, no. 1, pp. 183–198, 2013.

[69] H. Sato, Y. Takagi, and K. Sawaya, "High gain antipodal fermi antenna with low cross polarization," *IEICE transactions on communications*, vol. 94, no. 8, pp. 2292–2297, 2011.

[70] J. Bregains, J. Fondevila-Gomez, G. Franceschetti, and F. Ares, "Signal radiation and power losses of time-modulated arrays," *IEEE Transactions on Antennas and Propagation*, vol. 56, no. 6, pp. 1799–1804, 2008.

[71] H. Yang, F. Yang, S. Xu, M. Li, X. Cao, and J. Gao, "A 1-bit multipolarization reflectarray element for reconfigurable large-aperture antennas," *IEEE Antennas and Wireless Propagation Letters*, vol. 16, pp. 581–584, 2016.

[72] H. Yang, F. Yang, S. Xu, M. Li, X. Cao, J. Gao, and Y. Zheng, "A study of phase quantization effects for reconfigurable reflectarray antennas," *IEEE antennas and wireless propagation letters*, vol. 16, pp. 302–305, 2016.

[73] R. J. Mailloux, *Phased array antenna handbook*. Artech house, 2017.

[74] W. Wu, K.-D. Xu, Q. Chen, T. Tanaka, M. Kozai, and H. Minami, "A wideband reflectarray based on single-layer magneto-electric dipole elements with 1-bit switching mode," *IEEE Transactions on Antennas and Propagation*, vol. 70, no. 12, pp. 12346–12351, 2022.

List of Publications

I Journal Papers

[1] **X. Cao**, Q. Chen, T. Tanaka, M. Kozai and H. Minami, "A 1-bit Time-Modulated Reflectarray for Reconfigurable-Intelligent-Surface Applications," *IEEE Trans. Antennas Propag.*, vol. 71, no. 3, pp. 2396-2408, March 2023, doi: 10.1109/TAP.2022.3233659.

[2] **X. Cao**, H. Sato, K. -D. Xu, W. Jiang, S. Gong and Q. Chen, "A Systematic Method for Efficient Wireless Powering to Implantable Biomedical Devices," *IEEE Trans. Antennas Propag.*, vol. 71, no. 3, pp. 2745-2757, March 2023, doi: 10.1109/TAP.2023.3240005.

[3] **X. Cao**, Q. Chen, T. Tanaka, M. Kozai and H. Minami, "DOA Estimation and Object Localization Based on Multi-harmonic Multi-beam Characteristic of 1-bit Time-Modulated Reflectarray," *IEICE Commun. Express.*, vol. X12-B, no. 9, pp.-, August 2023, doi: 10.1587/comex.2023TCL0008.

[4] K. -D. Xu, Y. Cai, **X. Cao**, Y. Guo, Y. Zhang, and Q. Chen, "Multiband terahertz absorbers using T-shaped slot-patterned graphene and its complementary structure," *J. Opt. Soc. Am. B: Opt. Phys.*, vol. 37, no. 10, pp. 3034-3040, October 2020, doi: 10.1364/JOSAB.404062.

[5] **X. Cao**, W. Wu, Q. Chen, T. Tanaka, M. Kozai and H. Minami, "A Method for Enhanced-Efficiency Beam-forming With Time-Modulated Reflectarray at Carrier Frequency," *IEEE Trans. Antennas Propag.*, to be submitted.

II Conference Papers with Peer Review

[1] **X. Cao**, and Q. Chen, "Design of Multifunctional Reflectarray Elements Based on the Switchable Ground Plane," *2021 International Symposium on Antennas and Propagation (ISAP)*, Taipei, Taiwan, 2021, pp. 1-2, doi: 10.23919/ISAP47258.2021.9614460.

III Conference Papers without Peer Review

[1] **X. Cao**, and Q. Chen, "Design and Experimental Study on 1-Bit Time-Modulated Reflectarray," 電子情報通信学会 アンテナ・伝播研究会 (IEICE-AP), August 2023.

[2] **X. Cao**, and Q. Chen, "A Method for High-Efficiency Beamforming With Time-Modulated Reflectarray at Carrier Frequency," *The 2nd OPERA Student Workshop 2023*, April 2023.

[3] **X. Cao**, and Q. Chen, "A 1-bit Time-Modulated Reflectarray for Reconfigurable Intelligent Surface Applications," *The 1st OPERA Student Workshop 2022*, September 2022.

[4] **X. Cao**, and Q. Chen, "A Fast and Low-cost Method for Measuring the Reflection Characteristics of electronically controlled Refletarray Antennas," 2022 年電子情報通信学会総合大会, March 2022.

[5] **X. Cao**, and Q. Chen, "A 1-bit Time-Modulated Reflectarray for Reconfigurable Intelligent Surface Applications," 第 631 回伝送工学研究会, July 2022.

[6] **X. Cao**, and Q. Chen, "Design of Multifunctional Reflectarray Elements Based on the Switchable Ground Plane," 第 621 回伝送工学研究会, June 2021.